9-12-2014

Theoretical Studies of Transition Metal Catalysis

Ryan Johnson

Ryan Johnson
Candidate

Chemistry and Chemical Biology
Department

This dissertation is approved, and it is acceptable in quality and form for publication:

Approved by the Thesis Committee:

Hua Guo, Chairperson

Abhaya Datye

John Grey

Yang Qin

Theoretical Studies of Transition Metal Catalysis

by

Ryan S. Johnson

B.A., Bennington College, 2006

DISSERTATION

Submitted in Partial Fulfillment of the
Requirements for the Degree of

Doctorate of Philosophy
Chemistry

The University of New Mexico

Albuquerque, New Mexico

July, 2014

Dedication

For Mr. Seth, Stephen and Amanda. For motivation, support, and inspiration.
And not necessarily in that order.

Theoretical Studies of Transition Metal Catalysis

by

Ryan S. Johnson

B.A., Bennington College, 2006

Ph. D., Chemistry, University of New Mexico, 2014

Abstract

Transition metal catalysis, being critical to nearly all aspects of the modern industrial world, is the focus of a series of theoretical studies which seek to elucidate the fundamental and electronic origins of enhanced chemical activity and selectivity. The application of density functional theory on extended single metal and alloyed surfaces, supported single metal atoms, and gas phase cationic species illuminate various aspects of transition metal catalysis in a wide range of enviornments. Adsorption, reactivity, and other mechanistic details developed here suggest possible mechanisms used to aid interpretation of experimental results and guide developement of future catalysts.

Contents

List of Figures

List of Tables

Chapter 1

Introduction

1.1 Introduction

One of the most critical technologies responsible for our modern industrial world is the use of catalysts to accelerate reactions. A particularly potent example is the Bosch-Haber process in which nitrogen from the atmosphere is converted to ammonia over an iron based catalyst, allowing the affordable production of fertilizer and in turn the agricultural capacity to sustain much of the world's population. Automotive exhaust is cleansed of NO_x, CO and uncombusted hydrocarbons through a three way catalyst, reducing smog and air pollution. Furthermore, it has been estimated that over 90% of industrial processes use catalysts, and the overall impact of catalysts has been estimated to $10 trillion per year [1]. Industrial catalysts are often heterogeneous and composed of transition metal particles dispersed over solid supports, however, solid metal surfaces, ligated and solvated metal atoms, enzymes and single gas phase metal containing molecules are all catalytically active systems.

However important, the catalysts that are used industrially are very complex chemical materials, often using a great number of additives (promoters) in addition to the main catalytic material, and dispersed over a porous and not always chemically inert supporting material. The morphologies of the material are often complex and difficult to characterize. A further complication is that the active catalyst as found under reaction conditions is typically not the the same as the as prepared catalyst. Once exposed to the reaction conditions (pressure, temperature and the chemical species present) a catalyst can undergo restructuring and activation, as evidenced by the short period of time before reactions begin, known as the induction period. As a result, it is often necessary to study a catalyst *in situ*.

As a result of such complex structure and function, a detailed and molecular understanding of catalytic processes is is still poor and development of catalysts continues to be done through expensive trial and error today. Important breakthroughs

in understanding catalysis have come historically, not from studying the most active, and complex materials, but from simpler systems: clean, well defined surfaces, with low concentrations of reactants for simple reactions or from studying isolated molecular reactions. For example, the careful study of CO and O_2 adsorption [2] and reaction [3, 4] on various clean surfaces earned Gerhard Ertl a Nobel prize [5] in 2007. These simple systems guide development of fundamental models, trends and "rules of thumb" which can then be used in designing new, better and more efficient catalysts. Furthermore, advancements in theoretical methods (in particular density functional theory) have made possible the modeling of relatively large catalytic systems providing the molecular and electronic view that is so desperately needed to understand more complex systems. In the following work, DFT has been used in a number of model cases, ranging from perfectly clean and infinitely extended single metal and alloy surfaces to single metal atoms embedded in a supporting material, to gas phase transition metal catalysis.

1.2 General Concepts in Catalysis

A substance that is able to accelerate the rate of a reaction without itself being consumed in the reaction is called a catalyst. This is achieved by providing some alternative pathway to the products which avoids the uncatalyzed reaction barrier.

In Figure 1.1, we can see many important features in a chemical reaction, catalyzed and not. In black we see the unperturbed pathway that represents the energetics for an uncatalyzed chemical reaction. The reactant and product wells represent the bound vibrational well of reactants A and B, and product C. Distorting the geometry along a particular mode, which can be a complicated set of internal motions (here labeled simply "Reaction Coordinate"), will take the reactant up along the black path (ie "minimum energy pathway" (MEP)) to the transition state, the high-

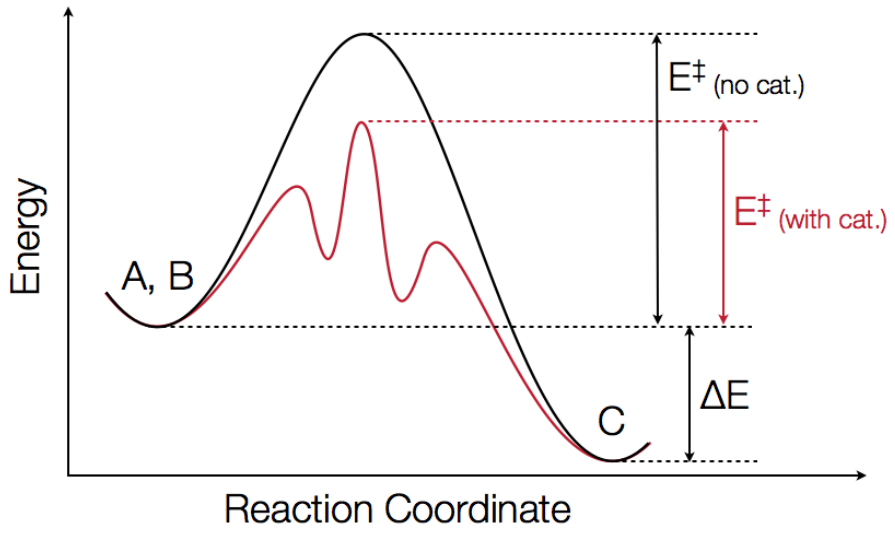

Figure 1.1: General reaction coordinate showing non-catalyzed reaction (black) and catalyzed reaction (red).

est energy point in a reaction. The transition state is of particular interest because of its intimate relationship with the rate of a reaction. According to Arrhenius, the rate of a reaction is given by:

$$k = Ae^{-E^{\ddagger}/k_B T} \tag{1.1}$$

Where A is a pre-exponential factor related how often the reactant attempts to surmount the barrier, $E^{\ddagger}$ is the activation energy of the reaction and $k_B T$ is the thermal energy available to the reactant at temperature T. Due to the exponential dependence of the rate with the transition state, a small reduction in the height of this barrier can significantly accelerate a reaction at a given temperature, or reduce the required temperature for the reaction to proceed at an appreciable rate.

This is one of the key roles of a catalyst, as is illustrated in the diagram in red. The red curve here implies that the function of a catalyst is to introduce a new pathway between the reactants an products, which circumvents the high barrier. Often, this

path will consist of new intermediate species stabilized with respect to the black curve. It is important to note that the overall Gibbs free energy of the reaction is unchanged, as this is a state function of the reaction and independent of the path taken from reactants to products. As a result, a catalyst also cannot modify the equilibrium of a reaction. It can be noted that in the framework of Transition State Theory (TST) the reactants and transition state are viewed to be in equilibrium. A reduction of the height of the barrier does in fact modify this pseudo-equilibrium in favor of the TS.

1.2.1 Functions of catalyst

Catalysts can play two roles: accelerate reactions and increase the selectivity for one possible product over other thermodynamically feasible ones. In 1948, Linus Pauling first hypothesized that an enzyme achieves catalysis by binding to, and therefore stabilizing the transition state. [6] This viewpoint has largely been supported by the subsequent 7 decades of research. However, catalysts can also achieve reduced transition states by stabilizing/destabilizing the product/reactant, as explored by Brønsted, Evans, Polanyi, Marcus and others in the context of the crossing of reactant and product potential energy surfaces. This will be discussed in further detail in section 1.3.3

The transition state is, in some sense, the worst possible energetic case a molecule will face. At this particular moment along a reaction coordinate there is a balance between breaking and forming chemical bonds. The energetic cost of dissociating the reactant molecule and forming the product meet at the same geometrical point. Often, there can be a buildup of charge in localized regions of the molecule at this point. Anything capable of stabilizing this charge buildup will reduce the activation energy of the barrier. Active sites of enzymes often have an electrostatic profile which

matches that of the transition state. Additionally, if the enzyme contains a metal center in the active site, the metal atom can act as an electron buffer for the TS; donating or accepting electron density as needed to offset the energetic penalty of charge buildup. A transition metal surface or particle can play the same role.

Selective catalysts are highly desirable in the context of increased atom economy, an important tenet of the green chemistry movement, but may also be important if side products are toxic to humans or down-stream processes. Selectivity is achieved by the modification of activation energies of the possible reactions with respect to each other. Either favorable products have lower barriers, unfavorable products have enhanced ones, or there can be a combination of both. This can either be a geometrical effect, ie. a particular isomer is blocked from forming by the geometric conformation of the catalyst-reactant complex, or an electronic one where one particular bond in the molecule is activated more than another as a result of interacting with the catalyst. The product which requires the lowest activation energy will dominate the final composition.

1.2.2 Surfaces, particles and single atoms

While not all catalysts use transition metals (examples are metal free enzymes and organocatalysis [7]), a great many do. Whether as surfaces, small particles, in metal containing enzymes, or solubilized metals, transition metals show a strong ability for catalysis. This is in part due to the fact that these atoms have a partially filled valence d shell that can both donate or accept electron density from reactants. For example, if in the transition state there is significant buildup of electron density, a transition metal could alleviate such an unfavorable situation by being reduced and accepting the excess density as needed. Alternatively, density can be donated, should a transition state be electron deficient. Transition metals are able to donate/accept

density because these primarily involve the valence d-orbitals of the metal, which are well screened from the nucleus, and as such are loosely bound to the atom. Furthermore, the near degeneracy of excited states can offer alternative reaction pathways which utilize excited spin surfaces, as will be discussed in Chapter 7.

For heterogeneous catalysts, activity is a function of surface area: the more exposed catalyst, the more places for reactions to take place. This basic principle has meant that in practice heterogenous catalysts are usually composed of small particles dispersed on some support (for example ZnO or Al_2O_3). In fact, the chemists and engineers designing catalysts were pioneers in nanoscience long before the term gained wide popularity and specific focus over the last decade. However, due to early challenges in characterizing and synthesizing uniform particles, many of the early breakthroughs in understanding these systems were done on well defined metal surfaces under ultra high vacuum conditions [2, 8]. While many of the key concepts learned from these studies are relevant for small particles, these single crystal systems cannot capture all of the unique and important features of industrially relevant small particles. For instance, a small particle can display multiple and/or high energy crystallographic surfaces, a high concentration of defects such as kinks or steps, interactions with the support, and unique electronic structure from an extended surface. All of these features have been found to impact catalysis [9] and some are visible in Figure 1.2.

For many reactions, the state-of-the-art catalyst is comprised of rare and expensive transition metals such as Pt, Pd or Ru. As such, it is desirable to use as little metal as possible. In the far most extreme case it would be advantageous to use only a single metal atom per active site. To this end a few papers [10–12] have recently been published which use single metals atoms anchored on supporting material and even find enhanced catalytic activity per atom. For example, in 2011 a Pt/FeO catalyst was found to have a turn over frequency for CO oxidation of $13.6 \times 10^2 (s^{-1})$,

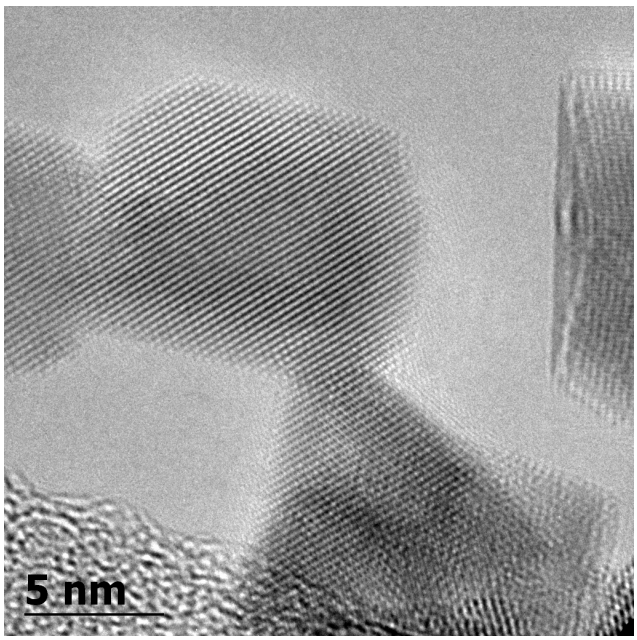

Figure 1.2: TEM image of Cerium oxide CeOx displaying (100) and (111) surfaces as well as defects and other heterogeneous morphologies. Image compliments of Andrew DeLaRiva.

2.9 times higher than that of Au/Fe_2O_3, a highly active catalyst [11]. Single atom catalysis is the focus of Chapter 6, in which single Pd atoms are incorporated into defects on a γ-Al_2O_3 surface. Developments in characterization methods such as tunnelling electron microscopy (TEM) and xray photoelectric spectroscopy (XPS) along with advancements in the controlled synthesis of nano-scaled systems have made the realization of single atom catalysts possible. These systems are also useful models for the study of fundamental processes which may be important in industrially relevant catalysts which may be difficult to isolate and examine systematically. For example, how a support modifies the electronic structure of an adsorbed metal is a key question and has been shown to be an important consideration in a number of systems [13, 14]. At the other end of large metal surfaces or nano-particles is the case of gas phase transition metal catalysis. Although not particularly relevant

for commercial processes the, small and isolated nature of such systems allow more detailed theoretical treatment. There is an important difference between atomic or molecular systems and extended systems like surfaces. The electronic states for isolated atoms/molecules are discrete, quantized states. In surfaces and bulk materials these electronic states are smeared out and described with band structures. It appears that some of the most interesting catalytic systems fall into an intermediary range between these two electronic models.

1.3 The d-band Model

A very powerful model for understanding and predicting the general reactivity of transition metals has been developed by Nørskov and Hammer [15–17] over the last decade, building on the foundational work of Newns and Andersen [18, 19]. This model identifies the d-band center as the most important descriptor for reactivity and offers insight into the mechanisms of adsorption and reactivity.

When discussing the d-band of a metal, there are a few interrelated quantities of interest: the metal-metal d orbital overlap between adjacent atoms (V_{ab}), the d-band width and the d-band center (E_d). V_{ab} largely determines the width; greater overlap and greater coupling between the atoms results in a more narrow d-band width and the center and width of the d band are interrelated via the electron occupation the bands. An increase in the overlap (eg. through compressive strain), causes the d-band width to increase. Since metals tend to conserve the number of occupied bands (those that fall below the Fermi level) the d-band center will shift down relative to the Fermi level thereby restoring the occupation of the band. As a result of the correlated behavior of these factors, only one needs to be chosen to characterize the interaction of an atomic of molecular adsorbate, and the d-band center has been found to be such a descriptor. The mechanism of adsorption is easiest to understand in terms

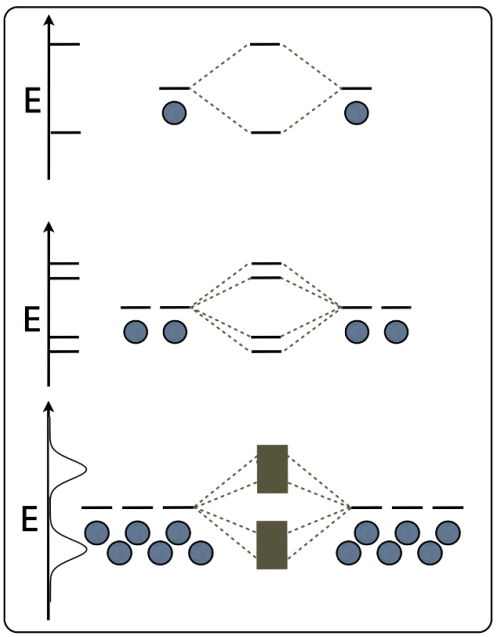

Figure 1.3: Model illustrating the transition from discrete energy levels in atoms and molecules, to broadened band structure in extended materials.

of an atomic adsorbate as discussed below, but the arguments can be extended to molecular systems and is elaborated in Chapter 5 for the adsorption of CH_2O.

1.3.1 Electronic Structure of Metals

A key qualitative difference between solid materials and molecules is the fact that the atomic orbitals which contribute to the structure are so numerous that they do not form discrete energy levels as in atoms and molecules, but rather bands, in which the eigenvalues form a continuum, or a band. This is illustrated in Figure 1.3.

For metal surfaces there are two distinct bands that form. The s-band and d-band from the overlap of s+p and d orbitals respectively. The s orbitals, largely delocalized across all atoms in the material, have a relatively large coupling element

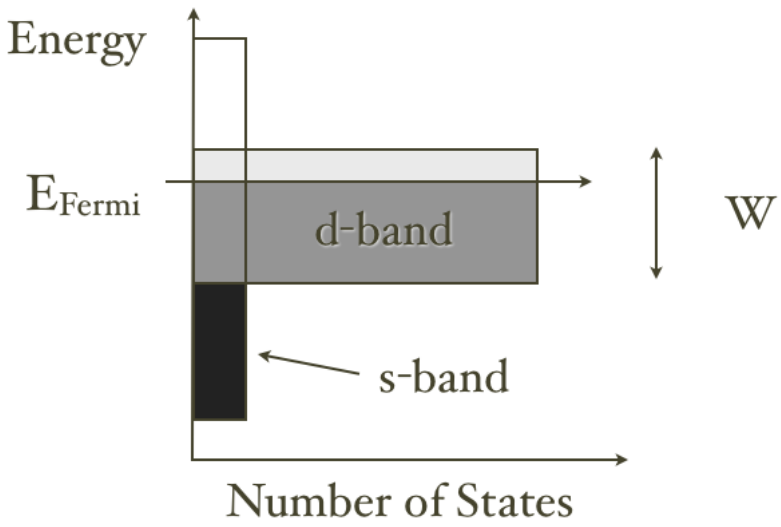

Figure 1.4: Cartoon model of the electronic structure in metals. The s-band is diffuse and half full. The d-band is more discrete and located near the Fermi level (E_{Fermi}).

between themselves, and as a result is very broad and half way filled. The d-band, conversely, is composed of the fairly localized d-orbitals which are less coupled to each other resulting a narrow band. The energy which divides the bands into occupied and unoccupied (also called the "valence" and "conduction" bands) regions is called the Fermi energy (E_{Fermi}). Electronic states that lay below the E_{Fermi} are occupied, and those above it are not. The Fermi level is analogous to the HOMO-LUMO gap in molecules.

The localization of d-orbitals and their resulting narrow d-band has profound implications in the bonding of adsorbates to the surface. The well quantized atomic and molecular eigenstates can interact with the relatively narrow d-band to form new bonding and anti-bonging orbitals between the surface and adsorbate as is seen in two-state atomic orbital model. This is opposed to interaction with the broad s-band, which does not split the orbitals but rather just smears them out. This interaction with the s-band is far weaker and does not change much from one metal

to another. The position of the d-band, on the other hand, varies from 4 eV below E_{Fermi} in Ag to 2.5 eV above in Hf. The relative position of the d-band determines the occupation of bonding/anti-bonding orbitals formed, and therefore the strength of adsorption.

1.3.2 Adsorption

The initial step for any reaction on a surface must be one or more of the reactants adsorbing on the surface. Adsorption may play a number of roles in surface catalysis, from immobilizing the species near each other, to fully modifying the electronic structure of the adsorbate upon interaction with the d-band. In some cases, this interaction is enough to break bonds in the molecule, as in the dissociative adsorption of O_2 on Pd(111) to form 2 atomic oxygen species. Alternatively, it could be a weaker interaction with the surface that simply activates a bond for later interaction with another species. This is the case for CO on Pd(111), in which the π^* MO of CO is populated from the d-orbital of the binding metal atom; elongating and weakening the C−O bond. These types of adsorption fall under the category of chemisorption, in that they result in a chemical bond to the surface. Physisorption, a weaker interaction, results from van der Walls interactions between the molecule and the surface. As this interaction is so weak and has almost no effect on the structure of the adsorbate, I will confine my discussion to the more catalytically interesting chemisorption.

Adsorption of a single atom on a surface is the simplest case and provides a clear picture of the electronic interaction, which is later applied to more complicated molecular adsorbates. When an atom comes close to a surface a number of interactions take place as the atomic orbitals mix with the valence states of the metal. It is useful to mentally break this into two separate steps, as is illustrated in Figure 1.5.

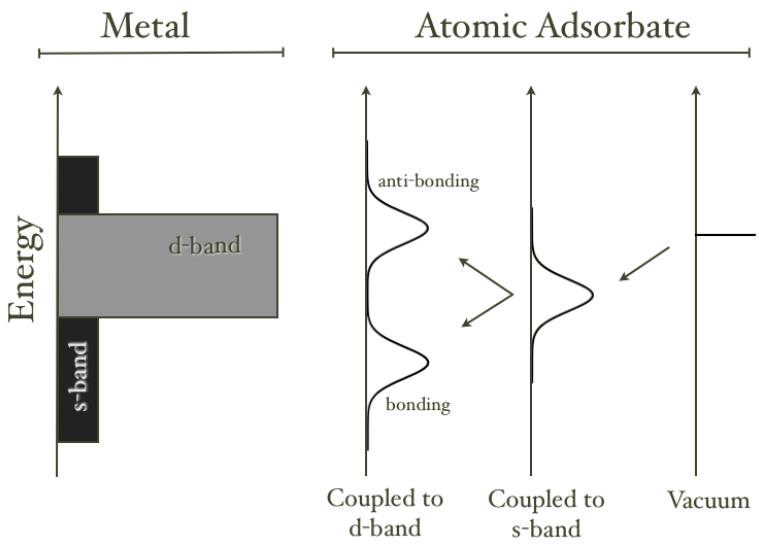

Figure 1.5: Illustration of the interaction of the atomic orbital as it couples with a metal surface. In vacuum the atomic orbital is discrete. Upon coupling with the s-band, the orbital is broadened. Coupling to the d-band slits metal-atom orbitals into bonding and anti-bonding orbitals, whose position with respect to (E_{Fermi}). depend on the position of the d-band in the metal and the atomic orbital.

First the AO's mix with the broad s-band of the surface. Since the s-band is so wide, this simply broadens the AO levels slightly, but does not cause them to shift in energy or spit into bonding and anti-bonding states. Secondly, there is coupling with the narrow d-band. Since the d-band is narrow, this interaction does result in bonding and anti-bonding orbitals formed above and below the initial AO's. The interaction of the atom with the surface is then controlled by the location of these orbitals with respect to the Fermi level. Since only the d-band forms bonding/anti-bonding orbitals, its relative position with respect to the Fermi level determines the extent to which the various atom-metal orbitals are filled, and thus it is the location of the d-band center than is the determining factor in determining the binding strength. If, for example, the d-band is very low with respect to E_{Fermi} than both bonding and anti-bonding orbitals would form below E_{Fermi}, resulting in no significant bonding

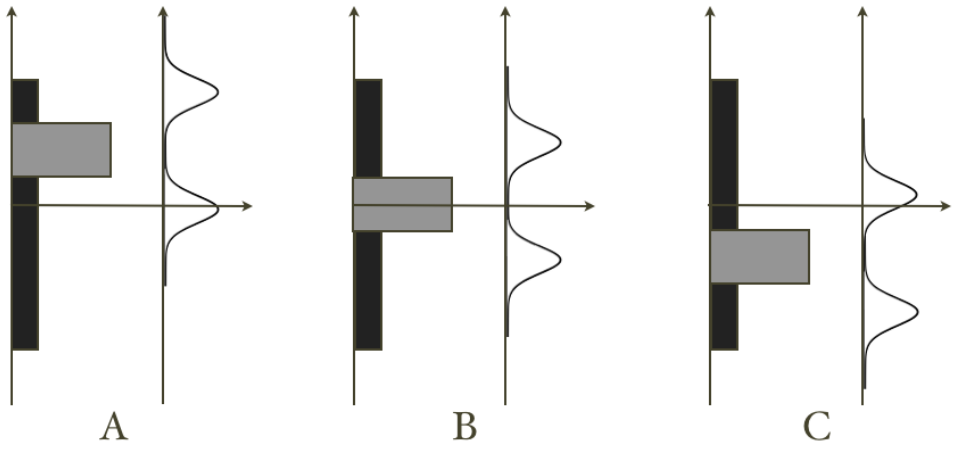

Figure 1.6: Three cases of d-band position and the resulting metal-atom orbitals upon adsorption. A) Unoccupied d-band; part of the resulting bonding orbital is populated. B) Half filled d-bad; here the strongest bond results because all bonding states are occupied and non of the anti-bonding. C) d-band totally occupied; now the anti-bonding orbitals are becoming populated weakening the adsorption.

interaction. On the other extreme, if the d-band center is very high, the resulting bonding and anti-bonding orbitals might both fall above E_{Fermi}, again forming no net bonding interaction. Three possible cases are presented in Figure 1.6

This implies that there is an ideal intermediate range of d-band position which form strong interactions with a given adsorbate, but not so strong that the adsorbed species is trapped on the surface. In fact, this variation in E_{Fermi} through the periodic table is the origin of the "volcano plot" of reactivity as shown in Fig 1.7 [20]. As the Sabatier principle identifies, the most active catalyst will be the one that does not bind too tight (poisoning) or too loose (no interaction) to the adsorbate. The most active transition metals tend to be those that fall in this intermediate range d-band center, and therefore adsorption strengths.

Molecular adsorption on surfaces follows that of atoms, but with some additional complexity. No longer is there a single adsorbate orbital interacting with the surface

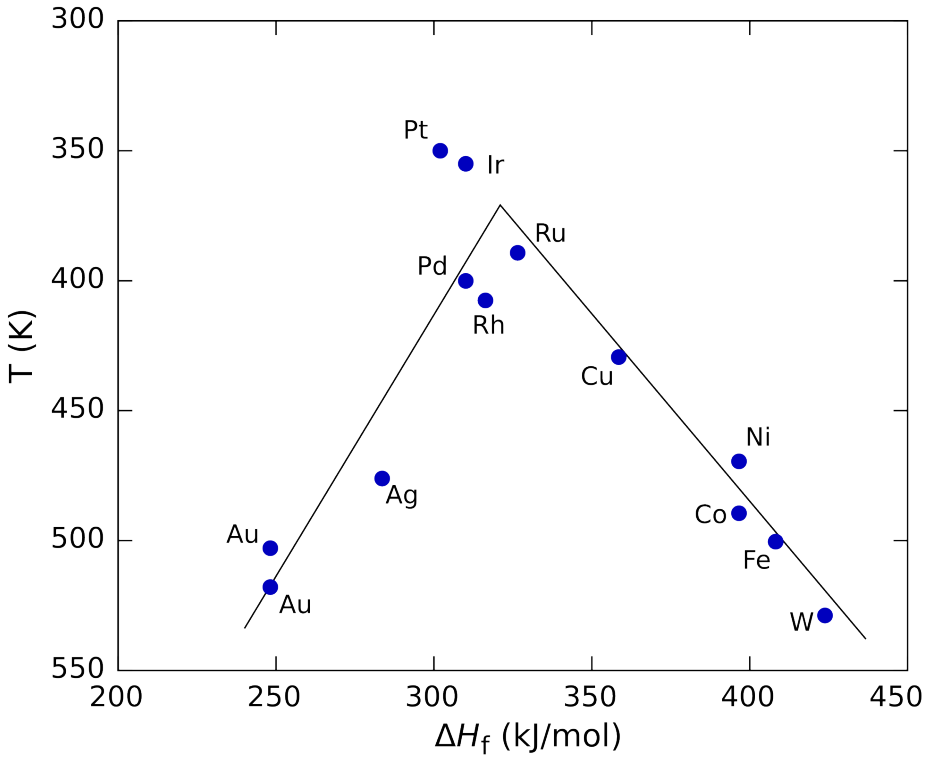

Figure 1.7: Volcano plot for the decomposition of formic acid on various transition metals. The temperature of decomposition (a measure of relative activation energy) is plotted against the enthalpy of formation. The most active metals are centered around Group 9 and 10 elements.

but many. As with atoms, there the molecular orbitals interact with the d-band to form new molecule-metal bonding and anti-bonding orbitals. The occupation of these orbitals determines the strength of the adsorption. However, the molecule also has it's own molecular bonding and anti-bonding orbitals which will change upon interaction with the surface. The change in filling of these molecular orbitals can change the bonding within the molecule itself, as in the loosening of the C−O bond upon adsorption to Pd.

1.3.3 Brønsted Evans Polanyi Relationships and Scaling Relationships

Another powerful theoretical framework on which to case catalytic reactions is the so called "BEP relationship", named after Brønsted, Evans and Polanyi, key figures in its development. [21, 22] Brønsted first articulated it in 1928 by observing that there was a linear relationship between the rate of an acid catalyzed reaction and the strength of the acid doing the catalysis. It was later generalized and extended to surface reactions. It articulates the relationship between the stability of reactants and products and the transition state between them. BEP relationships are often used to predict how the activation energy of a reaction will change on various metals. The BEP relationship can be written as,

$$\Delta E_{act} = \alpha \times \Delta E_r \tag{1.2}$$

where the change in activation energy (E_{act}) is linearly proportional to the corresponding change in reaction energy (E_r). Constant α depends on the particular reaction and can be roughly interpreted as how reactant-like (early) or product-like (late) the transition state is.

The key to understanding the BEP relationship rests on viewing the reaction as the crossing of two independent wells in the potential energy surface. One representing the reactant and the other the product. This is illustrated in Figure 1.8 where the reactant is labeled R, product P, and the transition state is represented by where the two curves cross. In this framework the transition state is the point at which the distortion of the reactant overlaps with the product well, both in geometry and in energy.

Also illustrated in Figure 1.8 is how a change in the vertical position of the reactant in this case, will shift the crossing point by roughly the same amount of energy. The depth of a well in the case of a surface reaction is simply the binding energy of

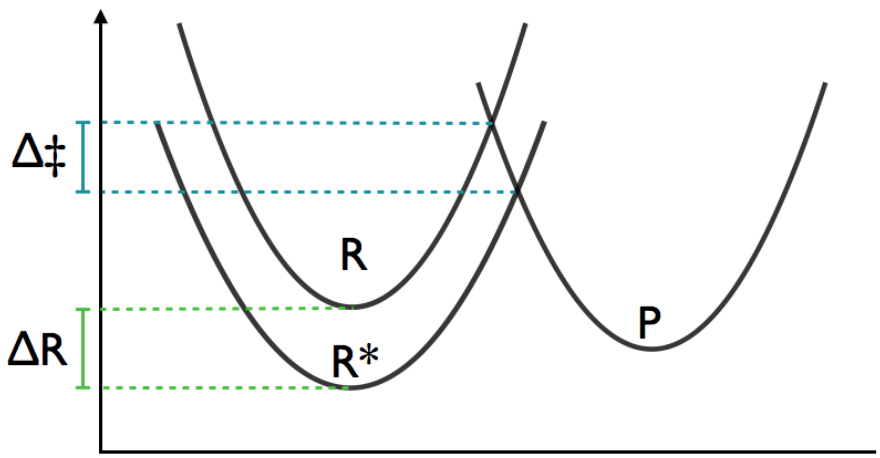

Figure 1.8: Illustration of the BEP relationship. Here the reactant has been stabilized by ΔR, resulting in a downward shift of the crossing points; the transition state by Δ‡.

a species to that surface. Assuming that the shape of the wells do not change going from metal to metal, and that the binding energy will change with the position of the d-band center of the metal as discussed above, knowledge of the activation energy and binding energies of one surface plus the change in binding energy for another metal is sufficient to predict the transition state energy on the other surface. This is useful in light of the practical challenges to calculating a transition state. Furthermore, since the d-band model allows the prediction of binding energies based on the d-band center, transition states can be estimated with only knowledge of the electronic structure of the surface.

As shown by Hammer and Nørskov [15–17], a consequence of the above d-band model of bonding to surfaces, a linear relationship is found between BE and d-center. As a result of the BEP relationships, the activation energy of a reaction can be related to the binding energy. This allows extrapolation of metal reactivity from a known

metal to one unknown one and the screening of many potential metals to a first approximation by their d-band center.

This is particularly useful in studying possible alloy combinations which have a d-band character of interest. Nørskov et al. have publish a few models recently which utilize these linear relationships to efficiently screen a great number of metals for reactivity [23–25]. The results of such screening can direct experimental studies on potentially active materials, an exciting step towards *a priori* catalyst design.

1.4 Conclusion

In the following chapters, transition metal catalysis will be explored in a number of cases, from mathematically infinite surfaces of metals, to a case of single atom catalysis, to studies of the reactivity of complexes which contain a single metal atom in the gas phase. Throughout these studies, time independent quantum mechanical methods have been used to predict the key geometries involved in reactions and their electronic structure, providing both practical and fundamental insight into these processes. Interestingly, these systems tend to be of a size scale that is difficult for our current quantum tools to treat. On one hand, our formalism of electronic structure is developed for an infinitely extended 3D periodic lattice and on the other for single isolated atoms. Both are strained when applied to these systems where the discrete quantum nature of an atom is blurred with the continuum nature of a solid.

In the next chapter I will outline the theoretical methods used throughout. Chapter 3 traces the possible reaction pathways of formaldehyde on a copper surface under methanol steam reforming conditions. In chapter 4 the effect of alloying Zn atoms into a Pd surface is studied in the context of CO oxidation. Further studies on the reactivity of formaldehyde on Pd, Cu and PdZn surfaces are investigated in chapter 5. Chapter 6 looks at the development of a model for a single Pd atom embedded

in a γ-Al_2O_3 surface, which is capable of performing CO oxidation at encouragingly low temperatures. These projects were often collaborations with experimentalists, whose data provided inspiration and key benchmarks for development of these theoretical models. The experimental methods and results are largely included to provide context and narrative, but have been edited down. Please see any publications for full details. The following chapters are associated with these publications: Chapter 3: [26], Chapter 4: [27], Chapter 7: [28].

References

[1] R. A. Santen, M. Neurock, and S. G. Shetty, "Reactivity Theory of Transition-Metal Surfaces:," *Chemical Reviews*, 2009.

[2] H. Conrad, G. Ertl, J. Koch, and E. E. Latta, "Adsorption of CO on Pd single crystal surfaces," *Surface Science*, vol. 43, no. 2, pp. 462–480, 1974.

[3] T. Engel and G. Ertl, "A molecular beam investigation of the catalytic oxidation of CO on Pd (111) — Browse - Journal of Chemical Physics," *The Journal of Chemical Physics*, 1978.

[4] T. Engel and G. Ertl, "Elementary steps in the catalytic oxidation of carbon monoxide on platinum metals," *Advances in Catalysis*, vol. 28, pp. 1–78, 1979.

[5] G. Ertl, "Reactions at Surfaces: From Atoms to Complexity (Nobel Lecture)," *Angewandte Chemie International Edition*, vol. 47, pp. 3524–3535, Apr. 2008.

[6] L. Pauling, "Nature of forces between large molecules of biological interest.," *Nature: International weekly journal of science*, vol. 161, pp. 707–709, May 1948.

[7] K. A. Ahrendt, C. J. Borths, and D. W. C. MacMillan, "New Strategies for Organic Catalysis: The First Highly Enantioselective Organocatalytic DielsAlder Reaction," *Journal of the American Chemical Society*, vol. 122, pp. 4243–4244, May 2000.

[8] G. Ertl, "Elementary Processes at Gas/Metal Interfaces," *Angewandte Chemie (International ed. in English)*, vol. 15, pp. 391–400, July 1976.

[9] G. A. Somorjai and J. Y. Park, "Molecular factors of catalytic selectivity," *Angewandte Chemie International Edition*, vol. 47, no. 48, pp. 9212–9228, 2008.

[10] S. Abbet, U. Heiz, H. Häkkinen, and U. Landman, "CO Oxidation on a Single Pd Atom Supported on Magnesia," *Physical Review Letters*, vol. 86, pp. 5950–5953, June 2001.

[11] B. Qiao, A. Wang, X. Yang, L. F. Allard, Z. Jiang, Y. Cui, J. Liu, J. Li, and T. Zhang, "Single-atom catalysis of CO oxidation using Pt1/FeOx," *Nature Chemistry*, vol. 3, pp. 634–641, July 2011.

[12] M. Yang, L. F. Allard, and M. Flytzani-Stephanopoulos, "Atomically Dispersed Au–(OH) x Species Bound on Titania Catalyze the Low-Temperature Water-Gas Shift Reaction," *Journal of the American Chemical Society*, vol. 135, no. 10, pp. 3768–3771, 2013.

[13] S. J. Tauster, "Strong metal-support interactions," *Accounts of Chemical Research*, vol. 20, no. 11, pp. 389–394, 1987.

[14] J. Y. Park, H. Lee, J. R. Renzas, Y. Zhang, and G. A. Somorjai, "Probing Hot Electron Flow Generated on Pt Nanoparticles with Au/TiO2 Schottky Diodes during Catalytic CO Oxidation - Nano Letters (ACS Publications)," *Nano Letters*, 2008.

[15] B. Hammer and J. K. Nørskov, "Electronic factors determining the reactivity of metal surfaces," *Surface Science*, vol. 343, no. 3, pp. 211–220, 1995.

[16] B. Hammer and J. K. Nørskov, "Theoretical surface science and catalysis—calculations and concepts," *Advances in Catalysis*, vol. 45, pp. 71–129, 2000.

[17] B. Hammer and J. K. Nørskov, "Why gold is the noblest of all the metals," *Nature: International weekly journal of science*, vol. 376, no. 6537, pp. 238–240, 1995.

[18] D. M. Newns, "Self-consistent model of hydrogen chemisorption," *Physical Review*, vol. 178, no. 3, p. 1123, 1969.

[19] P. W. Anderson, "Localized magnetic states in metals," *Physical Review*, vol. 124, no. 1, p. 41, 1961.

[20] "Volcano Plot." http://commons.wikimedia.org/wiki/File:Volcano_plot.png, 2008. Accessed: 2014-07-10.

[21] J. Bronsted, "Acid and Basic Catalysis.," *Chemical Reviews*, 1928.

[22] M. G. Evans and M. Polanyi, "Inertia and driving force of chemical reactions," *Transactions of the Faraday Society*, vol. 34, p. 11, 1938.

[23] P. Ferrin, D. Simonetti, S. Kandoi, E. Kunkes, J. A. Dumesic, J. K. Nørskov, and M. Mavrikakis, "Modeling Ethanol Decomposition on Transition Metals: A Combined Application of Scaling and Brønsted-Evans-Polanyi Relations," *Journal of the American Chemical Society*, vol. 131, pp. 5809–5815, Apr. 2009.

[24] L. C. Grabow, F. Studt, F. Abild-Pedersen, V. Petzold, J. Kleis, T. Bligaard, and J. K. Nørskov, "Descriptor-Based Analysis Applied to HCN Synthesis from NH3 and CH4," *Angewandte Chemie International Edition*, vol. 50, pp. 4601–4605, Apr. 2011.

[25] J. Greeley and J. K. Nørskov, "Large-scale, density functional theory-based screening of alloys for hydrogen evolution," *Surface Science*, 2007.

[26] S. Lin, R. S. Johnson, G. K. Smith, D. Xie, and H. Guo, "Pathways for methanol steam reforming involving adsorbed formaldehyde and hydroxyl intermediates on Cu(111): density functional theory studies.," *Physical Chemistry Chemical Physics*, vol. 13, pp. 9622–9631, May 2011.

[27] R. S. Johnson, A. DeLaRiva, V. Ashbacher, B. Halevi, C. J. Villanueva, G. K. Smith, S. Lin, A. K. Datye, and H. Guo, "The CO oxidation mechanism and reactivity on PdZn alloys," *Physical Chemistry Chemical Physics*, vol. 15, no. 20, pp. 7768–7776, 2013.

[28] S. G. Ard, J. J. Melko, V. G. Ushakov, R. Johnson, J. A. Fournier, N. S. Shuman, H. Guo, J. Troe, and A. A. Viggiano, "Activation of methane by FeO+: determining reaction pathways through temperature-dependent kinetics and statistical modeling.," *The Journal of Physical Chemistry A*, vol. 118, pp. 2029–2039, Mar. 2014.

[29] D. G. Truhlar and K. Morokuma, *Transition state modeling for catalysis*. American Chemical Society, 1999.

[30] B. C. Gates, *Impact of surface science on catalysis*, vol. 45. Academic Pr, 2000.

[31] G. Ertl, *Reactions at solid surfaces*, vol. 14. John Wiley and Sons, 2010.

[32] R. I. Masel, *Principles of adsorption and reaction on solid surfaces*. New York: Wiley, 1996.

Chapter 2

Methods

The study of chemical reactions on the molecular level requires that we confront the quantum nature of these systems. In principle, the Schrödinger equation offers us an complete description but full solutions to systems of interest to chemists are very difficult and thus largely unavailable. This has necessitated developement of the rich variety of approximate methods to study quantum systems. As discussed below, it is customary to first separate the treatment of the electronic part of the problem from the nuclear one. Under this so-called Born-Oppenheimer (BO) approximation, the Schrödinger equation for the electronic motion is solved at fixed nuclear configurations. In this Thesis, we will focus on the electronic problem.

The gold standard for treating electronic motion are the "first-principles" or *ab initio* methods that contain no empirical approximations; only the geometry, charge, spin state and fundamental constants are specified. They are typically very accurate, but also computational expensive. While impractical for routine use in large systems, they are powerful analysis and benchmarking tools for relatively small systems. An alternative approach to *ab initio* methods that has gained tremendous popularity is the density functional theory (DFT). In DFT, the problem is not cast in terms of wavefunctions as in the Schrödinger equation, but rather on the electron density and is efficient and qualitatively accurate. As a result, the primary methodology employed in the following work is DFT based.

There are two formalisms which I have utilized, depending on the nature of the system being studied. For large, periodic systems such as bulk crystals and surfaces, a planewave based DFT is the optimal choice. Inspired by the periodic nature of crystals, this formalism is cast in the language of planewaves, Fourier series and the notion of reciprocal space. For small gas phase systems an atomic orbital based DFT is preferred and inspired by the language of chemists. It is important to note that these two formalisms were derived to treat two different limiting cases: isolated atoms and molecules on one hand and infinitely extended crystalline structures on

the other. One is marked by quantized behavior and the other continuous. Both of these frameworks are deeply strained in some sense when applied to the intermediary systems that are of current interest in heterogeneous catalysis.

2.1 Quantum mechanics

The starting point for a quantum mechanical description of microscopic system is the time independent Schrödinger equation,

$$\hat{H}\Psi = E\Psi \tag{2.1}$$

where the wavefunction Ψ is a function of both the electronic and nuclear coordinates; $\Psi(r, R)$ for r electron coordinates and R nuclear coordinates. $\hat{H}$ is the Hamiltonian and E is its energy. Solving this partial differential equation for the individual and correlated motion of each nucleus and electron in the desired system, at least a $3N-6$ degree problem for N particles, is an immensely difficult mathematical undertaking.

Robert Oppenheimer and Max Born in 1927 [1] recognized the fact that the mass of a nucleus is more than 1800 times that of an electron and as such the nuclear motion is often so slow with respect to electron motion that the nuclear motion can be considered considered adiabatic. In other words, it is a good approximation to consider nuclei as a fixed framework upon which electrons move. The total wavefunction can thus be approximated as the product of the nuclear wavefunction (χ) and the electronic wavefunction (ψ) at a fixed position $\boldsymbol{R}$, ie

$$\Psi(r, \boldsymbol{R}) = \psi(r; \boldsymbol{R}) \times \chi(\boldsymbol{R})$$

A consequence of the Born Oppenheimer (BO) approximation is a divide-and-conquer scheme for studying molecular systems. Instead of solving electronic and nuclear problems simultaneously, the electronic energy is parameterized by the nuclear co-

ordinates and can be determined by repeating this step at different nuclear configurations. The resulting BO potential energy surface (PES) allows us to determine the forces acting on atoms as the negative derivative of PES with respect to nuclear coordinates, allowing geometry optimization. The BO PES can be used to predict behavior of the chemical system such as its reactivity and interaction with light. Our task is now to seek a solution to the electronic Schrödinger equation, the starting point is often the Hartree-Fock approximation, which is discussed below.

2.1.1 Hartree-Fock

In the Hartree approach, the true multi-electron wavefunction is approximated by the product of single electron wavefunctions:

$$\Psi(r_1, r_2, \ldots, r_n) = \phi(r_1) * \phi(r_2) * \cdots * \phi(r_n) \tag{2.2}$$

By replacing Ψ in equation 2.1 with the Hartree wavefunction, one can solve for the energies and wavefunctions for multi-electron systems. With this approximation each electron is under the averaged influence of the other electrons, and the Hamiltonian must account the Coulombic attraction to the nucleus, the electronic kinetic energy and for the average charge distribution of electrons. As the average repulsion felt by electron 1 with electron j is given by the integral of the product of the jth electrons charge density (the square of its wavefunction) and $1/r_{1j}$:

$$v_{1j} = \int |\phi_j(r)|^2 \frac{1}{r_{1j}} d\tau_j \tag{2.3}$$

the resulting single electron effective Hamiltonian for electron 1 is,

$$h_1^{eff} = \frac{-\nabla_1^2}{2} - \frac{Z}{r_1} + \sum_{j \neq 1} \int |\phi_j(r)|^2 \frac{1}{r_{1j}} d\tau_j \tag{2.4}$$

Since the solution for one electron requires the knowledge of all the other electrons, the problem must be tackled iteratively. First, a guess must be made for all

$\phi(r)$ in order to construct the electron-electron potential energy term in Eq. 2.4. Solving the resulting single electron Schrödinger equations provide improved wavefunctions over the initial guesses. The effective Hamiltonian is updated with the new $\phi(r)$, and the process is repeated until there is not significant change in energy or wavefunctions upon further iteration. This is known as the Self Consistent Field (SCF) procedure.

The above discussion does not take electron spin into account. We now must consider a spin-orbital χ, to be the product of the spatial function $\phi(r)$ and a spin function, either α or β. The Pauli exclusion principle requires that the total electronic wavefunction be antisymmetric upon exchange of any two electrons, ie: $\Psi(1,2) = -\Psi(2,1)$. As a result, only certain spin-orbit functions are valid. Vladimir Fock antisymmetrized the Hartree states by selecting only appropriate linear combinations of exchanged spin-orbit functions. The antisymmetrization was further developed by John Slater in the form of the so-called Slater determinant, shown in Eq. 2.5. For a closed shell system with two electrons, the wavefunction for two electrons sharing the same spatial orbital ϕ is written as the Slater determinant, then expanded into the resulting spin-orbit function,

$$\Psi(r_1, r_2) = \frac{1}{\sqrt{2}} \begin{vmatrix} \chi_1(1) & \chi_2(1) \\ \chi_1(2) & \chi_2(2) \end{vmatrix} \tag{2.5}$$

$$= \frac{1}{\sqrt{2}} \{\chi_1(1)\chi_2(2) - \chi_1(2)\chi_2(1)\} \tag{2.6}$$

$$= \frac{1}{\sqrt{2}} \{\phi(1)\phi(2)[\alpha(1)\beta(2) - \alpha(2)\beta(1)]\} \tag{2.7}$$

The Slater determinant ensures that if any two electrons are exchanged (ie two rows are switched) the wavefunction remains the same with a switched sign, and if any two rows are equal to each other (ie two electrons have the same spin and spatial coordinates) the determinant vanish, satisfying the Pauli principle.

Importantly, in in the Hartree-Fock (HF) method an electron does not "see"

another individual electron, but only its average charge density as given in Eq. 2.3. In truth, each electron will tend to avoid the other electrons in the system, slightly reducing Coulombic repulsion. The HF approximation fails, therefore, to account for this electron-electron correlation. The correlation function is is defined as the difference between the exact energy of the system and the HF energy,

$$E_{\text{corr}} = E_{\text{exact}} - E_{\text{HF}}$$

Relative to E_{HF}, E_{corr} is typically small and much of the total energy is reasonably well represented by the HF approach. However, the correlation energy is on the order of the strength of a bond, and therefore can become absolutely critical for accurate modeling of molecules and their processes. To address this problem a number of post-HF approaches have been developed to account for the missing electron correlation energy. These include the perturbative approaches of Møller-Plesset (MP3, MP4, etc), multi-configurational SCF, couple-cluster (CC) and configuration interaction (CI) based methods. DFT takes a distinct approach to the problem, and captures the correlation and exchange energies in an approximate. DFT takes a distinct approach to the problem, and captures the correlation and exchange energies in an approximate way through the use of an exchange-correlation functional, and is not typically considered to be an *ab inito* method because the exact form of the functional is not known.

Post Hartree-Fock *ab initio* Methods

In HF, the total wavefunction is constructed using only the Slater determinant corresponding to the ground state. However, by writing the total wavefunction as a linear combination of all possible determinants (in other words, by including those determinants that represent all possible excited configurations in which one or more unoccupied orbitals are switched with occupied ones), electron correlation is reintroduced into the calculation. It is common to label these excited determinants by

the number of electrons that are being simultaneously excited; "singles" for a wavefunction that includes all single electron excitations, "doubles" for two, etc. The HF determinant could be considered the zeroth configurations, in that it has no excitations.

$$\Psi_{CI} = \sum_k c_k D_k \tag{2.8}$$

where D_k contains the HF determinate and k possible excitations within a given basis set. The energy is minimized with respect to the coefficients c_k. For N electrons and M orbitals the number of D_k is $(2M!)/[N!(2M-N)!]$ and can quickly number in the millions or billions, thus is only possible for small systems. This is called the Configuration Interaction (CI) approach, and when used as the full CI with all possible D_k the exact energy is found for a given basis set. Since the number of D_k can be so large and because not all excited determinants will contribute equally to the correlation energy, the number of configurations is often truncated. For example CIS and CISD are methods which just include the single or single and double excitations respectively. Unfortunately, it is not possible to tell *a priori* how large such an expansion needs to be and there is not well behaved convergence with respect to increasing k.

Another popular approach to truncating the number of excitations considered is called the "Complete Active Space" SCF or CASSCF. Here, the wavefunctions are divided into three types: those that are doubly occupied in all configurations, those that are totally unoccupied, and the active space which contain the electrons and orbitals that are allowed to participate in excitations. Furthermore, unlike CI where HF wavefunctions are used unchanged and only determinant coefficients C_k are optimized, the CAS procedure optimizes both determinant and wavefunction coefficients. This can dramatically reduce the computational effort, but requires careful selection of the active space. Generally, one wants to choose one which captures all the important states (large c_k) that contribute to the Ψ and few of those

with minimal contribution.

Similar in spirit to CI but cast in terms of quantum operators is the Coupled Cluster (CC) method. Here the total wavefunction Ψ_{CC} is constructed from Ψ_0, the single HF determinant, operated on by an exponential operator which performs the excitations as in CI in the exponent.

$$\Psi_{CC} = e^T \Psi_0, \tag{2.9}$$

where

$$T = T_1 + T_2 + T_3 + \cdots \tag{2.10}$$

Here T_1 performs modifications of the HF determinant to create the ensemble of possible single excitations, T_2 the doubles, and so on. When all T operators are included, the exact wavefunction is found within the given basis set, just as in CI. However, this is only possible again for the smallest systems. Often the excitation operator is truncated with the first or second, resulting in CCS and CCSD respectively. The accuracy of these level calculations is superb for their speed, but can be further improved with addition of higher terms. The "gold standard" of computational chemistry, CCSD(T) with a large basis set, includes some triple excitation not iteratively like the singles and doubles, but rather uses a perturbative approach to make estimates of the triplet contribution. This method is still considered to be "single reference" because only the ground state HF determinant is used to generate the expansion.

2.1.2 Density Functional Theory

In the 1960's Density Functional Theory (DFT) was first established by two seminal papers by W. Kohn, P. Hohenberg, and L. Sham [2, 3]. These two papers have had a tremendous impact in molecular and atomic modeling as evidenced by the fact that

they are the two most cited papers in the publishing journal: Physical Review and by the exponential growth of those citations since 1964. Unlike the *ab initio* methods discussed above, which concern themselves with the 3N dimensional wavefunction $\Psi(r_1, r_2, \ldots, r_N)$, DFT is cast in terms of the total ground state electron density of the system $\rho(r)$, a function of only the three spatial coordinates. Although not as accurate as the post-HF *ab initio* methods, DFT scales far better with the number of electrons and thus as drastically increased the size of systems that can be brought under quantum mechanical analysis.

Kohn and Hohenberg first laid the theoretical underpinnings of DFT by showing that the total energy of a molecule is a unique functional (function of a function) of the electron density and that there exists a variation principle such that any density that other than the ground state density will have an energy greater than the ground state energy.

The basic form of the energy functional can be written as the sum of two terms;

$$E[\rho(r)] = \int V_{ext}(r)\rho(r)dr + F[\rho(r)] \tag{2.11}$$

Where $\rho(r)$ is the electron density, (V_{ext}) is the external Coulombic potential of the BO nuclear framework, and $F[\rho(r)]$ is a "catch-all" for everything else including the electronic kinetic, exchange and correlation energy contributions. Since $E[\rho(r]$ is uniquely determined by V_{ext}, the functional $F[\rho(r)]$ must be universal for any system of electrons! Unfortunately, the exact form of $F[\rho(r)]$ is not known, but Kohn and Sham proposed the following expansion:

$$F[\rho(r)] = E_{KE}[\rho(r)] + E_H[\rho(r)] + E_{XC}[\rho(r)] \tag{2.12}$$

Here $E_{KE}[\rho(r)]$ is the kinetic energy of a system of non-interacting electrons with the same density as the true system at point r. $E_H[\rho(r)]$ is the classical electrostatic (Hartree) energy of the electrons and $E_{XC}[\rho(r)]$ is the exchange-correlation energy. The first two terms are known exactly, however some error is introduced by taking

the kinetic energy of non-interacting electrons and a correction for this is included in $E_{XC}[\rho(r)]$. In practice, this last term is actually implemented as $V_{XC}[r]$, which is the functional derivative of $E_{XC}[\rho(r)]$ with respect to the density ρ;

$$V_{XC}[r] = \left(\frac{\delta E_H[\rho(r)]}{\delta\rho(r)}\right) \tag{2.13}$$

$V_{XC}[r]$ is called the exchange-correlation potential and its approximation is key to the success of DFT. Kohn and Hohenberg offered the first approximation for $V_{XC}[r]$ in their 1964 paper, called the Local Density Approximation (LDA). Here, $V_{XC}[r]$ is just the exchange-correlation potential for a homogeneous electron gas of density $\rho(r)$. This model of an even and infinitely distributed electron gas is a poor model for molecular systems, yet it proved to have better accuracy than HF for comparable computational effort. This is in part because DFT is able to account for some of the correlation energy, whereas the correlation is explicitly ignored in HF. However, LDA-DFT suffers from shortcomings such as overbinding, in which bond strengths are consistently over estimated.

Later, the Generalized Gradient Approximation (GGA) family of functionals were developed which include local gradients of electron density in deriving the exchange-correlation functional and tend to perform much better than LDA. The functional used in Chapters 3, 4, 5 and 6, Perdue-Wang 1991 (PW91) [4], is a GGA functional and is very popular for the study of surface chemistry. One of the most successful functionals developed and the one used in Chapter 7, Becky3-Lee-Yang-Parr (B3LYP) [5], is considered a "hybrid functional" because it uses a portion of the exact exchange energy as calculated from Hartree-Fock along with a GGA based functional. The amount of HF exchange to include is empirically fit to the heats of formation of a number of small molecules. Hybrid functionals are slower than non-hybrid because they perform a HF calculation as well as evaluate the DFT functional, but the accuracy is significantly improved over non-hybrid GGA functional.

There exists a variational principle for DFT that states the lowest energy possible

achieved for a given electron density corresponds to the actual ground state electron density. This allows an iterative approach to solving the problem. The density is first expanded by linear combination of basis functions in some (often random) fashion. Then these orbitals are optimized with respect to the expansion coefficients until the total energy is minimized. It should be noted that the orbitals that are calculated in DFT are actually the so-called one electron "Kohn-Sham orbitals", but are very similar to the actual molecular orbitals and can be casually interpreted as such [6].

2.1.3 Basis Sets

An important consideration in any quantum calculation is the choice of basis set. Mathematically, a basis is a complete set of linearly independent vectors which together in linear combination, can represent any possible vector in that space. Quantum mechanically, they are the set of basic (often atomically inspired) functions which are used, in linear combination, to construct the total electronic wavefunctions and/or electron density for a given nuclear framework. These are the functions that are used to construct the $\phi(n)$ in equation 2.2 by linear combination:

$$\phi(r) = \sum c_i b_i \tag{2.14}$$

Typically, the coefficients c_i of this expansion are optimized in the SCF procedure until sufficiently converged. The size of a basis set expansion is one of the primary limits of accuracy within a given model chemistry, thanks to the variational treatment. For example, if they are not sufficiently large (numerous) there is not enough flexibility in coefficient optimization to accurately model the chemical system. In principle, larger basis sets tend to be more accurate, however a practical number of basis sets that can be reasonably handled today is on the order of 1000 functions. There are two popular classes of basis functions (b_i); atomic-orbital inspired and planewave basis sets. These are typically used to model isolated and periodic

systems respectively.

Atomic orbital basis sets

A chemically intuitive approach to constructing basis sets is to use atomic based orbitals. This is in the spirit of the LCAO-MO procedure, which constructs molecular orbitals from the linear combination of atomic orbitals. For example, a carbon atom may be constructed from a 1s, 2s, and 3 separate 2p orbital functions. To ease the computational effort of dealing with the cusp at $r = 0$ for many atomic orbitals a series of Gaussian functions are used to fit, as close as possible the radial features of the true orbital. Using Gaussian functions to mimic the atomic orbitals is a far more efficient approach because mathematical operations on Gaussian functions are relatively easy. However, multiple Gaussian functions are needed to describe both the cusp behavior and exponential tail of the function. This results in a larger set of functions which comprise the basis set, but the computational efficiency is still largely improved. Basis sets are further enlarged by doubling or more the number of Gaussian constructed atomic orbitals included, adding higher angular momentum orbitals (polarized functions) and/or including deliberately diffuse functions in the basis set expansion.

Plane-wave basis sets

Another popular choice of basis functions particularly convenient for periodic systems is planewaves of various frequencies. A Fourier series can be constructed by adding enough planewaves, which vary in wavevector k to completely model the system. The expansion will require high frequency functions near the nucleus where the wavefunction is more energetic and therefor more curved. Lower frequency planewaves are needed far from the nucleus, where the energy (and curvature) of the wavefunction

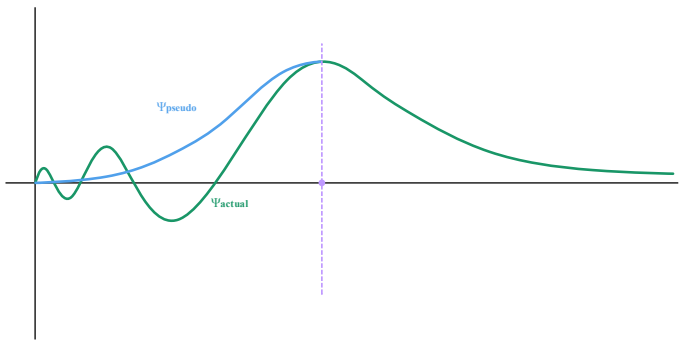

Figure 2.1: Difference between pseudopotential (blue) and actual wavefunction (green). Beyond cutoff radius (purple) they are identical.

is much less.

In principle, a planewave basis set forms a complete basis set, however approximations are often made to minimize the number of planewaves used to construct the basis. For instance, an energy cutoff is usually employed above which no planewaves are included in the Fourier series. This is reasonable because the high energy (and high frequency) functions are usually associated with the core electrons which do not play a large role in chemistry. The completeness of the planewave basis set means that results can be systematically improved by increasing the cutoff energy.

Pseudopotentials

Core electrons are qualitatively different from valence electrons in that they differ in energy by an order of magnitude or more, are spatially located in different areas of the atom and are rarely involved in chemical bonds. Additionally, the core electrons are often the most challenging computationally, because the core wavefunctions oscillates wildly near the nucleus, which require many high frequency planewaves to accurately model. Hence it seems reasonable to replace these core functions with

approximate ones, which are easy to deal with mathematically yet produce the same effective potential on valence electrons. Additionally, these approximate functions can be built to include effects not typically addressed by electronic structure calculations such as the orbital contraction that results from relativistic effects in late period transition metals. Under the atomic orbital formulization these functions are called effective core potentials (ECP) and when used with planewaves they are called pseudopotentials (PsP). This concept is illustrated in Figure 2.1. Currently the most popular pseudopotentials are of the "projector augmented wave" (PAW) type [7, 8]. Development of these PsP's is done by finding the appropriate linear transformation matrix ($\mathbf{T}$) between the true wavefunction Ψ and the pseudo one $\hat{\Psi}$ such that $\Psi = \mathbf{T}\hat{\Psi}$. Due to the high accuracy and efficiency of these PsP's they have been used throughout the periodic DFT work contained in this Thesis.

2.2 Application of quantum mechanical tools

2.2.1 Periodic Boundary Conditions

The quantum mechanics of periodically repeating systems can be elegantly cast in terms of reciprocal space and planewaves. Surfaces, being 2D periodic entities are most effectively modeled under periodic boundary conditions (PBC). This framework, which differs significantly from that of isolated systems, is addressed now.

An idealized crystal is a periodic entity with a unique "unitcell" defined by lattice constants **a, b** and **c**. The unitcell is repeated infinitely in space by a translational operation: $\mathbf{T} = n_1\mathbf{a} + n_2\mathbf{b} + n_3\mathbf{c}$, where n_1, n_2 and n_3 can be any integers. Bloch recognized that since the nuclei of a crystal are periodic arranged, the resulting electronic wavefunction will also be periodic, and so will all properties derived from that wavefunction. For example, if the electron density of copper metal is equal

to $\rho(r)$ at point r in the unitcell, than $\rho(r + \mathbf{T}) = \rho(r)$. Bloch's theorem is a condition that solutions for the Schrø"dinger equation must satisfy and it provides the connection between the original unit cell and all others extending infinitely out in space. This theorem is;

$$\Psi_E(r) = \Psi_E(r + \mathbf{T}) = e^{i\mathbf{kT}}\Psi_E(r) \tag{2.15}$$

This subtle result requires wavefunctions to obey Eq. 2.15, in that under any translation operation ($\Psi_E(r+\mathbf{T})$) only differs from $\Psi_E(r)$ by the multiplicative phase factor $e^{i\mathbf{kT}}$. This arises from the translational symmetry of a crystal but in essence maps the infinitely extended space in r to a discrete reciprocal space in $\mathbf{k}$. The wave vector $\mathbf{k}$ has units of inverse length and corresponds to points within the reciprocal space of the lattice in the same way that r is used to denote points in Cartesian space. The ground electronic state of a crystal is determined by evaluating the energy as a function of $\mathbf{k}$, touring the reciprocal unitcell (called the first or irreducible Brillouin Zone (IBZ)) and tracing out the "Band Structure" of the crystal. Since the number of $\mathbf{k}$ vectors in the IBZ is equal to the number of unitcells in the structure, any macroscopic crystal will have essentially an infinite number that must be evaluated. In practice, only a subset of possible $\mathbf{k}$ vectors in the IBZ, selected by k-points, are considered.

K-points

To evaluate properties of the wavefunction, integration must be done over all $\mathbf{k}$, which in principle could be infinite. K-points are a grid of points extended in reciprocal space which defines the $\mathbf{k}$ vectors that are sampled. The idea of a k-point grid is justified in the fact many $\mathbf{k}$ vectors are degenerate; only a representative sampling of important k-points is needed.

There is an inverse dependence on the number of kpoint required and the size

of the supercell; the smaller the unit cell, the higher the number of k-points are required for accurate calculation. However, when a very large unit cell is used, only a single kpoint, called the gamma point, is required. If a gas phase molecule is being studied the periodic nature of the model needs to be suppressed. Using a gamma point calculation can achieve this without using massive unitcells. This is key in calculating the binding energy of a molecule to a surface. For this common calculation we need to model both a periodic system, the clean surface and the molecule in the gas phase.

Throughout the following studies of surfaces, the k-point grid is generated automatically by the method of Monkhorst and Pack [9], which simply extends a homogeneous grid of k-points of user specified density throughout the IBZ. To choose the k-point grid, a number of calculations are performed for the same system but with increasing grid density. Properties of interest must be converged with respect to k-points. Fortunately, we are not typically interested in absolute energy values, but instead the difference between two or more structures. As long as these comparisons are made between identical unit cells, and with the same k-point grid, errors from slightly unconverged k-points are canceled systematically. In Figure 2.2 the binding energy of carbon monoxide on Cu(111) is plotted against the number of k-points used.

Construction of Slab and Supercell Selection

The use of PBC-DFT to study surfaces requires that the model constructed must be a unitcell that repeats infinitely in all three directions. Surfaces are built first from an optimized bulk structure which is cleaved to the desired plane, and then expanded and oriented to construct the "supercell", or the unitcell that defines the entire model. There are a number of important considerations while constructing such models and they will be discussed here.

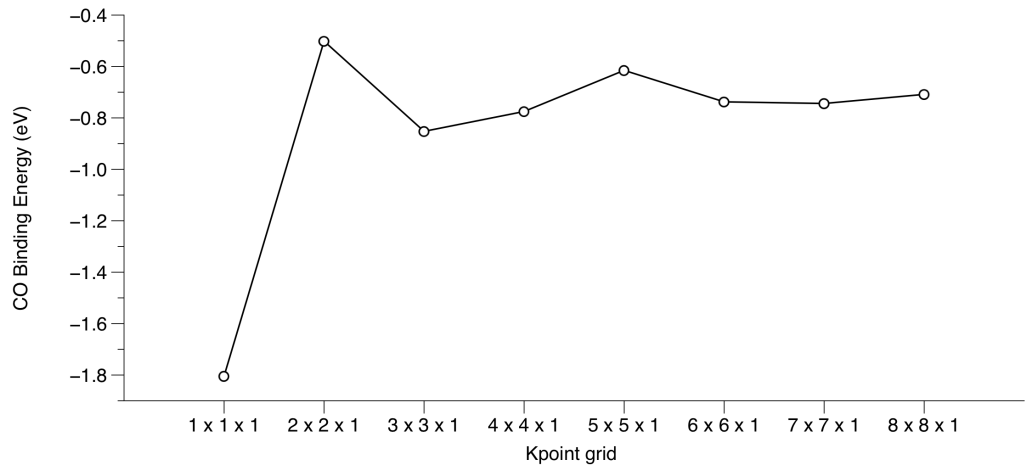

Figure 2.2: The binding energy of CO on Cu(111) is calculated for various kpoint grids. C and O atoms are allowed to relax at each kpoint. Kpoint grids are generated to insure that they are always Γ-centered and reasonable convergence is acheived at 6x6x1.

A surface is the termination of a bulk material, and so to construct one it is reasonable to begin with the bulk material itself. The bulk calculation for simple materials consists of determining the lattice constants of the primitive unitcell, and for fcc metals like Pd and Cu there is only one defining parameter a. The PW91 GGA functional used in these studies tends to over-correct the overbinding problem of the LDA functionals, and so tends to overestimate the lattice constant slightly. For Cu, for example, $a = 3.67$Å with PW91 is 0.05Å larger than the experimentally determined value. DFT optimized values are used to reduce any artificial compression, which has the effect of lowering the dband center and changing the reactivity of the surface.

The optimized bulk structure is cleaved with the Miller indices defining the surface of interest. Often, low index surfaces such as the (111) are more densely packed and more thermodynamically favored. Defects such as steps and kinks can be modeled with higher index surfaces, which expose increasingly under-coordinated surface

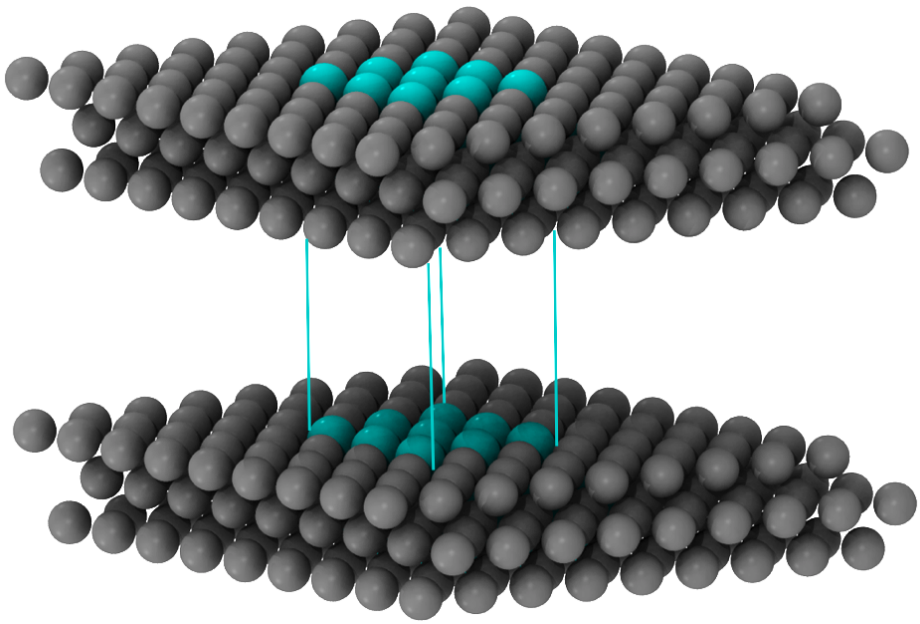

Figure 2.3: The periodic nature of these models is illustrated. The original supercell is highlighted and periodic images in all three directions shown.

atoms. The cleaved surface slab is then reoriented in the supercell as slice of the top layers of the surface. A vacuum layer is added above the surface to separate one slab from its periodic image in the z direction. A final surface supercell is displayed in Figure 2.3.

We see that this model is not really that of a surface as we usually think about it, but rather an infinitely stack of slabs of atoms separated by a finite vacuum spacing. A true surface is achieved only the limit of an infinitely thick vacuum and slab. Vacuum slabs are usually on the order of 15Å for small molecule and atomic adsorbates. The thickness of the slab and whether or not it is allowed to relax are important accuracy vs. speed considerations. For simple metals, models with 3-5 atomic layers in which the top layer is allowed to relax from it bulk-truncated position are usually sufficient. The surface area of the supercell can be adjusted

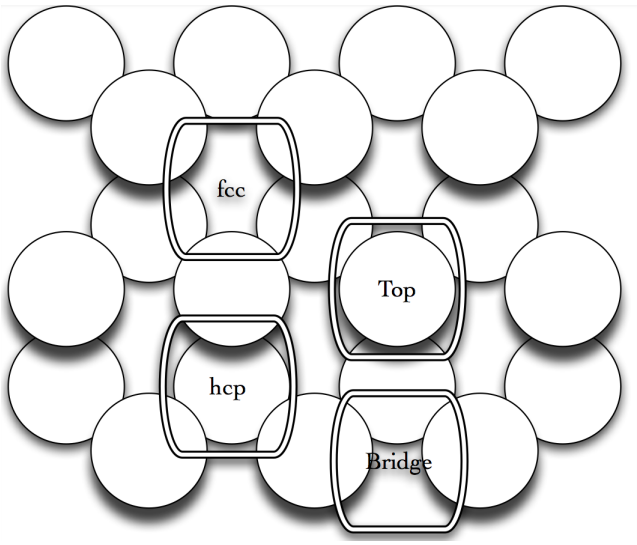

Figure 2.4: A graphic of the surface of Cu(111) surface with unique adsorption sites illustrated and labeled.

in order to mimic various surface concentrations of adsorbates. A full monolayer coverage is achieved with a small supercell containing only a single occupied binding site. Increasing the supercell size but not the number of adsorbates decreases the surface coverage accordingly.

The (111) surface of an face center cubic (fcc) metal, such as Cu an Pd has four possible high symmetry binding sites. "Top", which is on top of an atom, "bridge" which is between two atoms, and two hollow sites which are between three atoms. The hollow sites are labeled fcc and hcp depending on whether there is a atom directly below. These sites are illustrated in Figure 2.4. Adsorbates on a surface may have strong preference for particular binding sites over others and preference can change depending on the concentration of adsorbates. This can have a profound impact on the details of reactivity. Engel and Ertl [10, 11] showed that the complex interplay between adsorbed CO and dissociating O_2 at various binding sites and under various pressures resulted in kinetics not described by simple rate laws.

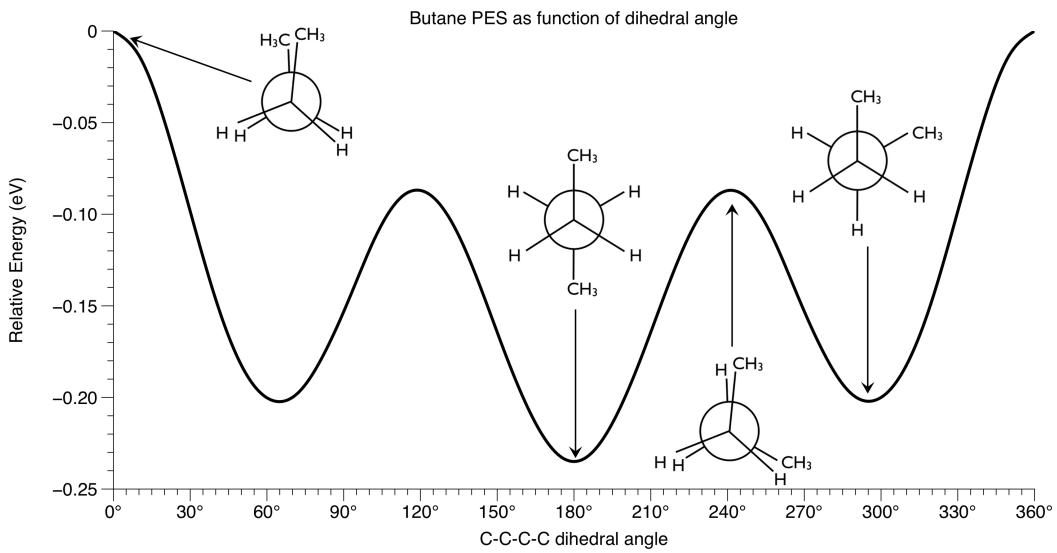

Figure 2.5: The potential energy diagram of butane as it is rotated along the center carbon-carbon axis. Many topographical features of various stationary points are illustrated.

2.2.2 Topographical definition of stationary points

Under the BO approximation, we seek to identify stationary points ($dR/dE = 0$) along the 3N dimensional PES in order to characterize a chemical reaction. Differences in the energy of minima relate to thermodynamic quantities and equilibrium constants, and the maxima, or transition state between two minima, determines the rate of a reaction. The unique topographical features of these points allow the determination and classification of stationary points, and these will be discussed here using the butane molecule as an example. Figure 2.5 shows one 2D slice of the 42D PES of butane as energy vs. the C-C-C-C dihedral angle is scanned from 0 to 360°. Eclipsed, gauche and staggered geometries are highlighted.

Minima in a potential energy surface (both local and global) correspond to bound species, or those which will have some measurable lifetime due to their stability.

Topographically, minima are molecular geometries that experience a restoring force against any small displacement of nuclear coordinates. A calculation of vibrational modes at a minima will find $3N - 6$ real vibrational frequencies for a non-linear molecule with N atoms. Minima can be further categorized as the global, the lowest possible energy configuration or local, which are less stable than the global minimum. The global minimum for butane is, as shown in Figure 2.5, the "Anti" conformation at 180°, where steric hindrance is most reduced. Two degenerate local minima exist as "Gauche" conformations at 60° and 300°.

Transition states are maxima for the minimum energy path between the two minima that define reactants and products. They are actually saddle points in the topography of the PES in that they are a point of both positive and negative curvatures. In other words, for any arbitrary perturbation of the transition state geometry the energy will rise, save for one particular mode which displacement along will result in a lower energy. This particular mode, also called the imaginary frequency mode, corresponds to the reaction coordinate through that point. As discussed in Chapter 1, the transition state can be viewed as the point at which the product and reactant minima curves cross. In Figure 2.5 a transition state exists between every pair of minima.

As a result of these unique topographical features of stationary points, vibrational mode analysis is a useful tool for characterizing structures. A method commonly employed, the finite differences method, involves displacing each atom in x, $-x$, y, $-y$, z and $-z$ by a small amount ($\sim$0.01 Å) from its equilibrium position. Usually under the harmonic oscillator approximation, the vibrational frequencies are calculated. Minima will have $3N - 6$ modes and transition states will have $(3N - 6) - 1$ real modes and one imaginary one. Harmonic vibrational frequencies are defined as $\omega = \sqrt{k_f/\mu}$, where k_f is the force constant of the vibrational mode in question and μ is the reduced mass. For minima, the force constant will always be positive, but

at a maxima k_f is negative. Hence it is proper to use the term imaginary due to the square root, but most computational codes report it as a negative frequency. Occasionally, a search for a transition state will result in more than one imaginary mode, indicating that it is not a 1st order saddle point.

Additionally, the calculation of vibrational modes allows a zero-point vibrational energy correction to be added to the energy. Approximating the vibrational wells of the molecule with harmonic oscillators leads to the following definition of the ZPE correction:

$$E_{ZPE} = \sum_i \frac{\hbar\omega_i}{2} \tag{2.16}$$

where ω_i is the harmonic vibrational frequency for the ith mode. ZPE correction for transition states includes all but the imaginary frequency in the above summation.

At a transition state, the imaginary frequency describes the curvature of the potential through the saddle along the reaction pathway. This has important consequences for another quantum effect: tunneling. A transition state can be viewed as a barrier from one state to another and quantum mechanics tells us there is a finite probability of a system to tunnel through barriers. The probability is a function of the mass of the particle, the height and width of the barrier. The magnitude of the imaginary frequency provides insight into the width of the barrier, and if the reaction involves light atoms like hydrogen, a narrow barrier (large imaginary mode) might indicate that tunneling could be playing a role in the reaction dynamics. However, to quantify this requires studying the dynamics of the reaction, which is precluded in these approaches by use of the time independent Schrödinger equation.

These discussions have all concerned themselves with the ground electronic state of a molecule or surface. In many cases this is sufficient but there are cases when excited potential surfaces must be understood in addition to the ground state. Photochemistry, in which the deliberate excitation of the system is used to make/break

bonds, is best understood in terms of a vertical transition to the excited potential energy surface. If the excited state does not share the same minimum energy geometry as the ground state the system will move along the gradient of that potential and change its geometry appropriately. In cases where there are states very close in energy to the ground state, as is often the case with transition metals, another phenomena can occur. The ground state electronic configuration may change with the geometry of the molecule. If a molecule is going from one geometry to another, ie moving along a PES, and it encounters another PES (same geometry and energy) there is a possibility that the molecule will undergo an electronic rearrangement and cross to the other surface. This has a profound impact on chemistry involving transition metals, and speaks to the reasons behind their ability to catalyze reactions. These concepts are explored in greater deal in Chapter 7.

Geometry Optimizations

Locating various stationary points on the PES, ie optimizing the molecular geometry until it is either a minimum or a transition state, often depends on derivative based methods. The direction of 1st derivative of energy with respect to nuclear coordinates ($\partial E/\partial R_i$) indicates where the minimum lies and its magnitude provides information on the steepness of the potential energy surface at that geometry. "Steepest descent" and "conjugate gradient" are two popular optimization algorithms which use the derivative to locate minima moving the atoms in the direction parallel to the net force. "Conjugate gradient" tends to converge on the minimum faster as each new step in the minimization is both orthogonal to the gradient and to the previous search vector. The Hessian, or the matrix of second partial derivatives of energy with respect to geometric coordinates, can also be utilized in optimization methods. The "Newton-Raphson" method, for instance, calculates a new geometry from the difference of the current geometry and the gradient times the inverse Hessian.

While very powerful, calculation and inversion of the Hessian can be computationally formidable. Fortunately, analytical expressions for the derivatives are available for many methods like atomic orbital based DFT, and minimization is efficient.

A particularly useful method for locating transition states and mapping minimum energy paths from reactants to products is the Nudged Elastic Band method (NEB) and in particular the Climbing-Image variant of NEB [12, 13]. In this method, the geometry of reactant is linearly extrapolated to the product in a series of images of intermediary geometries. In simple NEB, these points are then simultaneously optimized but are given an artificial force constant which connects each state to its nearest neighbors forming an elastic chain of structures from reactant to product. The "band" of geometries will minimize along the minimum energy pathway (MEP), passing through the saddle point. There is no guarantee that one of the points will fall at exactly the transition state and a large number of images must be used to accurately describe the barrier height. Climbing Image-NEB addresses this problem by performing an additional step after the NEB has converged. The image highest in energy (and therefore closest to the TS) is freed from the neighboring images and optimized uphill along the reaction coordinate until the forces acting on the atoms vanish. This final image should be located at the transition state of interest, however in practice a vibrational mode analysis is performed to check the existence of the single imaginary frequency, and verify that a saddle point has been located. CINEB has been utilized in all periodic DFT work to locate transition states and trace the minimum energy path MEP between reactants and products.

References

[1] M. Born and R. Oppenheimer, "Zur Quantentheorie der Molekeln," *Annalen der Physik*, vol. 389, no. 20, pp. 457–484, 1927.

[2] P. Hohenberg and W. Kohn, "Inhomogeneous electron gas," *Physical Review*, 1964.

[3] W. Kohn and L. Sham, "Self-consistent equations including exchange and correlation effects," *Physical Review*, 1965.

[4] J. P. Perdew and Y. Wang, "Accurate and simple analytic representation of the electron-gas correlation energy," *Physical Review B*, vol. 45, no. 23, pp. 13244–13249, 1992.

[5] P. J. Stephens, F. J. Devlin, C. F. Chabalowski, and M. J. Frisch, "Ab Initio Calculation of Vibrational Absorption and Circular Dichroism Spectra Using Density Functional Force Fields," *The Journal of Physical Chemistry*, vol. 98, pp. 11623–11627, Nov. 1994.

[6] R. Stowasser and R. Hoffmann, "What do the Kohn-Sham orbitals and eigenvalues mean?," *Inorg. Chim. Acta*, vol. 257, p. 253, 1997.

[7] P. Blöchl, "Projector augmented-wave method.," *Physical review B, Condensed matter*, vol. 50, pp. 17953–17979, Dec. 1994.

[8] G. Kresse and D. Joubert, "From ultrasoft pseudopotentials to the projector augmented-wave method," *Physical Review B*, vol. 59, no. 3, p. 1758, 1999.

[9] H. J. Monkhorst and J. D. Pack, "Special points for Brillouin-zone integrations," *Physical review B, Condensed matter*, vol. 13, no. 12, pp. 5188–5192, 1976.

[10] T. Engel and G. Ertl, "A molecular beam investigation of the catalytic oxidation of CO on Pd (111) — Browse - Journal of Chemical Physics," *The Journal of Chemical Physics*, 1978.

[11] T. Engel and G. Ertl, "Elementary steps in the catalytic oxidation of carbon monoxide on platinum metals," *Advances in Catalysis*, vol. 28, pp. 1–78, 1979.

[12] H. Jonsson, G. Mills, and K. W. Jacobsen, "Nudged elastic band method for finding minimum energy paths of transitions," in *Classical and Quantum Dynamics in Condensed Phase Simulations* (B. J. Berne, G. Ciccotti, and D. F. Coker, eds.), Singapore: World Scientific, 1998.

[13] G. Henkelman, B. P. Uberuaga, and H. Jonsson, "A climbing image nudged elastic band method for finding saddle points and minimum energy paths," *The Journal of Chemical Physics*, vol. 113, no. 22, pp. 9901–9904, 2000.

Chapter 3

Reaction of formaldehyde and hydroxyl intermediates on Cu(111)

This chapter is based on collaborative work found in the following publication:

Reproduced from S. Lin, **R. S. Johnson**, G. K. Smith, D. Xie, and H. Guo, *Pathways for methanol steam reforming involving adsorbed formaldehyde and hydroxyl intermediates on Cu(111): density functional theory studies.*, Phys. Chem. Chem. Phys., vol. 13, no. 20, pp. 9622 – 9631, May 2011, with permission from the PCCP Owner Societies.

3.1 Introduction

Methanol steam reforming (MSR);

$$CH_3OH + H_2O \longrightarrow 3\,H_2 + CO_2 \qquad \Delta H^\circ = 49.6 \text{ kJ/mol}$$

has emerged as a leading candidate for generating hydrogen fuel for on-board applications such as proton exchange membrane (PEM) fuel cells [1–4]. In this approach, methanol serves as a liquid hydrogen carrier, thus avoiding the challenging problem of hydrogen storage and transportation. Methanol has several advantages as a hydrogen carrier. First, it is commercially produced in large scale with established techniques. Second, existing infrastructure for other liquid fuels, such as gasoline, can be leveraged with some modifications in transportation, storage, and dispense. Third, methanol is a relatively clean fuel because of its high H/C ratio and low sulfur content [3, 5]. Finally, MSR generally takes place at relatively manageable temperatures ($150 - 300\circ$C) as no C−C bonds need to be cleaved, and good catalysts are known.

The traditional catalyst for MSR has been Cu supported by ZnO, which is highly selective towards CO_2 [1, 3, 4]. This selectivity is very important as the by-product CO, in addition to being a pollutant, readily poisons anode sites in PEM fuel cells [1, 3]. Unfortunately, copper catalysts suffer sintering at temperatures above 300°C,

with the associated loss in surface area and reactivity. Furthermore, copper catalysts are pyrophoric when exposed to oxidative conditions, a significant concern when used in automotive applications. More recently, a PdZn alloy formed on ZnO has shown some promise as an alternative MSR catalyst with better thermal stability [6]. It is believed that MSR proceeds on the PdZn/ZnO catalysis in a similar way to that on Cu/ZnO [7–9]. As a result, elucidation of MSR on Cu may help us to understand the process on other catalysts as well.

In order to improve existing catalysts and design new ones for MSR, it is important to understand the catalytic mechanism. Although efforts in this direction have been made through kinetic modeling [10, 11] there is much uncertainty in such endeavors because not all kinetic intermediates are experimentally identifiable. Thanks to advances in plane-wave density functional theory (DFT) [12] there is an increasing interest in addressing mechanistic questions in heterogeneous catalysis from the bottom up [13–15]. Indeed, much work has been reported on the decomposition of both methanol and water on Cu surfaces using DFT [16–24]. For example, the complete reaction path from CH_3OH to $CO + H_2$ has been mapped out in pioneering DFT studies by Greeley and Mavrikakis on Cu(111) [16], and by Mei, Xu, and Henkelman on Cu(110) [23]. Although these studies have shed much light onto MSR catalysis, none has yet provided information concerning how the various species produced by these decomposition processes interact with each other and how the $CO_2 + H_2$ products are formed.

It has been proposed that MSR on Cu based catalysts is initiated by OH bond cleavage of both CH_3OH and H_2O. The resulting methoxyl (CH_3O) and hydroxyl (OH) species adsorb strongly on the metal surface. These species may further dehydrogenate to produce formaldehyde (CH_2O) and O, respectively, but typically with high barriers. Indeed, the dehydrogenation of CH_3O is considered to be the rate-limiting step in MSR [10, 11, 25, 26]. On the other hand, formaldehyde has

been identified as a key intermediate in MSR and was detected in both MSR [27] and decomposition reactions of CH_3OH on Cu [28–30]. Indeed, when fed with H_2O under steam reforming conditions [27], it produces CO_2 and H_2 as products, further suggesting its key role in MSR. Three mechanisms have been proposed for MSR on the copper catalyst [3, 4, 26]. The first consists of methanol decomposition to CO, followed by conversion to CO_2 via the water-gas shift (WGS) reaction ($CO + H_2O \longrightarrow H_2 + CO_2$) [1]. However, the importance of this decomposition/shift pathway is now discounted by most researchers [3], as WGS was found inoperative in the presence of methanol [10, 27, 31]. The second mechanism involves reactions of CH_2O with adsorbed OH or O species to produce intermediates such as formic acid (CHOOH), formate (CHOO), and dioxomethylene (CH_2OO), which eventually convert to $CO_2 + H_2$ [32]. At high temperatures, an alternative pathway involving methyl formate ($CHOOCH_3$), formed from $CH_3O + CH_2O$, has also been proposed [10, 11, 27]. Methyl formate is also one of the main products in methanol decomposition over Cu in the absence of water [31, 32]. Unfortunately, the latest experimental studies were unable to determine definitively whether the second or the third mechanism is in operation [26]. It is possible that both mechanisms are active depending on the operating temperature [27]. In this Chapter, we will focus on the formic acid/formate/dioxomethylene pathway(s).

It is well known that formaldehyde adsorbs weakly on Cu and is nonreactive [33]. Recent DFT calculations have indicated that because of the relatively high ($\sim$0.65 eV) barrier the dehydrogenation of formaldehyde on copper surfaces cannot compete with desorption, although its dehydrogenation product, namely CHO, readily decomposes to CO + H on Cu surfaces with large exothermicity and a small barrier [16, 19, 23]. Hence, it is reasonable to assume that there has to be a pathway that diverts formaldehyde to the experimentally observed selective production of CO_2 in MSR. More importantly, the reaction must have a barrier lower than or comparable to the adsorption energy of formaldehyde. A likely mechanism involves the

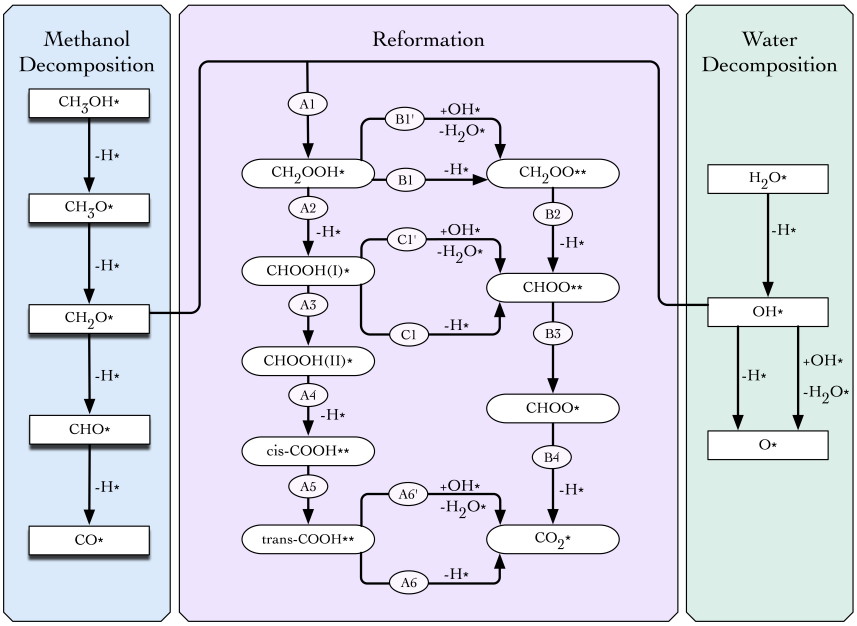

Figure 3.1: Proposed pathways for the decomposition and steam reforming of methanol on Cu(111).

reaction of CH_2O with OH or O produced by water decomposition. In Fig. 3.1, we sketched a few possible reaction pathways for such processes. In order to gain insights of the MSR mechanism, plane-wave DFT results are reported in this Chapter for these elementary steps on Cu(111). The energetics of the reaction network should help us to advance our understanding of this important process. This Chapter is organized as follows. The theory and computational protocol are outlined in Sec. 3.2 The results are presented in Sec. 3.3. The subsequent section (Sec. 3.4) discusses the implication of the calculation results in the context of MSR catalysis. Finally, a summary is given in Sec. 3.5.

3.2 Theory

All DFT calculations were carried out using the Vienna ab initio simulation package (VASP) [34–36] with the gradient-corrected PW91 exchange-correction functional [37]. The ionic cores were described with the projector augmented-wave (PAW) method [38, 39] and for valence electrons a plane-wave basis set with a cutoff of 400 eV was employed. The Brillouin zone was sampled using a $4 \times 4 \times 1$ MonkhorstPack k-point grid [40] with Methfessel-Paxton smearing of 0.1 eV [41]. The optimized bulk lattice parameter for Cu was found to be 3.67 Å, in good agreement with the experimental value (3.62 Å) [42]. Slab models for the Cu(111) surface consisted of three layers of a 3×3 unit cell, with the top layer allowed to relax in all calculations. Our unit cell is larger than previous work [14, 23, 24], and it reduces the chance of artificial interactions between co-adsorbed species in adjacent cells. A vacuum space of 14 Å was used in the z direction. The adsorption energy was calculated as follows: $E_{\text{ad}} = E_{\text{adsorbate + surface}} - E_{\text{free molecule}} - E_{\text{free surface}}$. The climbing image nudged elastic band (CI-NEB) method [43, 44] was used to determine the reaction pathways with the energy (10^{-4} eV) and force (0.05 eV/Å) convergence criteria. Stationary points were confirmed by normal mode analysis and the vibrational frequencies were used to compute zero-point energy (ZPE) corrections.

3.3 Results

3.3.1 Adsorption of pertinent species

In order to understand elementary chemical steps in MSR, it is important to first characterize the adsorption of pertinent species. In Table 3.1, we list the geometric and energetic information on various such species adsorbed on Cu(111). Many species

involved in the decomposition of CH_3OH^* and H_2O^* on Cu(111), such as CH_3O^*, have been extensively investigated before, and our results are in general agreement with the available literature values. Below, we will focus on other species identified in Fig. 3.1. The adsorption energies and geometric parameters of the energetically preferred states of all relevant species are listed in Table 3.1, where the side and top views of the adsorption geometries are also included.

CH_2OOH

This species formed by the reaction between CH_2O^* and OH^* preferentially adsorbs in a unidentate fashion at the fcc site through its carbonyl oxygen, with the methylene hydrogens pointing away from the surface. The distances between the O atom and the three surface Cu atoms are 2.04, 2.04, and 2.17 Å, respectively. The adsorption energy of -2.23 eV indicates relatively strong chemisorption. The calculated O−C−O angle was found to be 111.48. As far as we know, there has been only one DFT study on this species, where a similar adsorption energy (-2.78 eV) and configuration were reported on Cu(100) [45]. This species appears in all the reported pathways explored in this study.

CH_2OO

The dioxomethylene species adsorbs on Cu(111) with both oxygen moieties on bridge sites. The bidentate bonds are roughly equivalent. The calculated O−C−O angle is 112.7 and the two H atoms point away from the surface. A similar adsorption pattern has been reported in several earlier DFT studies in the context of methanol synthesis [15, 46], where the dioxomethylene is believed to be a key intermediate. The dioxomethylene species has been observed on Cu(110) as a product of formaldehyde oxidation, serving as a precursor to formate (CHOO) [33]. The bidentate adsorption

Species	Adsorption Configuration	D_{Cu-A} (Å)	Adsorption Energy (eV)	Bond Details	
				Bond	Length (Å)
H	Fcc/Hcp through H	1.74	-2.45 (-2.28)/ -2.44 (-2.27)	-	-
O	Fcc/Hcp through O	1.90	-4.94 (-4.86)/ -4.94 (-4.87)	-	-
OH	Fcc through O	2.03	-3.21 (-3.12)	O-H	0.97
H_2O	Top through O	2.34	-0.20 (-0.16)	O-H	0.98
CO_2	Top through O	3.58	-0.04 (-0.03)	C=O	1.18
CH_2O	Parallel to surface	3.41	-0.06 (-0.06)	C=O	1.22
				C-H	1.12
Bidentate-CHOO	Top-Top through O	2.01	-2.78 (-2.63)	C-O	1.27
		2.02		C-H	1.11
Unidentate-CHOO	Fcc through O	2.09	-2.25 (-2.14)	C=O	1.22
		2.11		C-O	1.35
		2.18		C-H	1.11
Cis-COOH	Bridge through O and C	2.11	-1.78 (-1.72)	C=O	1.25
		1.96		C-O	1.35
				O-H	0.98
Trans-COOH	Bridge through O and C	2.12	-1.67 (-1.62)	C=O	1.26
		1.96		C-O	1.35
				O-H	0.99
CHOOH(I)	Top through O	2.23	-0.24 (-0.24)	C=O	1.23
				C-O	1.32
				O-H	1.01
				C-H	1.10
CHOOH(II)	Top through O	2.41	-0.10 (-0.08)	C=O	1.22
				C-O	1.34
				O-H	0.98
				C-H	1.10
CH_2OO	Bridge-Bridge through both Os	2.04	-4.15 (-3.98)	C-O	1.42
		2.04		C-H	1.10
		1.99			
		1.98			
CH_2OOH	Fcc through O	2.04	-2.23 (-2.08)	C-O	1.42
		2.04		O-H	0.98
		2.17		C-H	1.10

Table 3.1: Adsorption energies and geometric parameters for various pertinent species on Cu(111). Entries in the parentheses are the ZPE-corrected values.

leads to a large adsorption energy of -4.15 eV, which is also in reasonable good agreement with that reported by Mei et al. [46] (-3.69 eV) on the same surface. The difference might be attributable to the smaller k grid ($2 \times 2 \times 1$) used by these authors. This species appears only in pathway B reported here.

CHOOH

Due to its closed shell nature, the formic acid adsorbs weakly on Cu(111), with an adsorption energy of -0.24 eV. There are two important adsorption configurations, as shown in Table 3.1. In the first configuration (CHOOH(I)), the carbonyl oxygen interacts with a Cu atom on the top site. The hydroxyl hydrogen points toward the surface, while another hydrogen atom on the carbon points upwards. The distance between the carbonyl oxygen and the Cu atom is 2.23 Å and the two calculated O-C bonds are 1.23 and 1.32 Å, respectively. In the second adsorption configuration (CHOOH(II)), the carbon hydrogen points toward the surface and the hydroxyl hydrogen points away from the surface. The calculated adsorption energy is smaller with the value of -0.10 eV. The weaker interaction is reflected by the fact that the distance between the carbonyl oxygen and the Cu atom is elongated to 2.41 Å. The weak adsorption of formic acid on copper is consistent with experimental observations [47]. This species appears in pathways A and C reported in this study.

CHOO

It is known that formate (CHOO) can adsorb on Cu(111) with both bidentate and unidentate modes [14, 24, 46, 48]. The bidentate adsorption features atop adsorption via the two oxygen atoms with O-Cu distances of 2.01 and 2.02 Å, respectively. These distances are very close to the reported experimental and theoretical values [14, 46, 49]. The calculated O−C−O angle of 127.8 is also consistent with the

previous theoretical values of 126.9 [46], and 127.8 [14]. The molecular plane is perpendicular to the surface and the adsorption energy was found to be -2.78 eV. The unidentate adsorption, on the other hand, features an oxygen on the hpc site with a smaller adsorption energy of -2.25 eV. While the O−C−O angle is roughly the same (124.2), the O-Cu bond lengths (2.09, 2.11 and 2.18 Å) are slightly longer than those in the bidentate configuration. The adsorption energies for the bidentate and unidentate binding modes are in good agreement with theoretical values, such as those obtained by Gokhale et al. (-2.77 and -2.32 eV, respectively) [14]. The stronger bidentate adsorption of formate is consistent with experimental observations [50, 51]. This species appears in pathways B and C reported in this study.

COOH

The carboxyl species have two possible conformations, namely the cis and trans-COOH species. Their adsorption patterns on Cu(111) are however similar, namely with C−O moiety interacting at the bridge site in a bidentate fashion with two Cu atoms. For the cis-COOH, the molecular plane is nearly perpendicular to the Cu(111) surface with an O−C−O angle of 115.4 and the C−Cu and O−Cu bond lengths are 1.96 and 2.11 Å, respectively. For the trans-COOH, as shown in Table 3.1, the configuration is close to that of cis−COOH except that its O−H bond pointing toward the surface. The cis isomer binds slightly stronger (-1.78 eV) than its trans counterpart (-1.67 eV). Our results differ somewhat from previous studies which have used a 2×2 unit cell [14, 24]. While we can reproduce the literature values with the smaller 2×2 unit cell, we believe that our 3×3 unit cell should provide a better description of the low coverage adsorption because it avoids interactions between adsorbates in adjacent unit cells. This species appears in pathway A reported in this study.

3.3.2 Reaction Pathways

As shown in Fig. 3.1, the decomposition of CH_3OH^* and H_2O^* on Cu(111) produces several species. Since the decomposition processes have been extensively investigated before, we will focus here on the reactions between the key decomposition products on the Cu(111) surface. The initial step of methanol decomposition involves the cleavage of the O−H bond, and this activated reaction has a moderate barrier, e.g., 0.68 eV on Cu(110) [20]. This is followed by the dehydrogenation of CH_3O^* leading to CH_2O^* with a high (ZPE corrected) barrier of 1.16 eV [17]. Although this step might in principle be achieved with the assistance of OH^*, which abstracts a hydrogen from CH_3O^*, the barrier for this process is unlikely to be lowered with the participation of OH^*, as discussed below. On the other hand, the decomposition of water to H^*+OH^* on Cu(111) is also activated with a (ZPE-corrected) barrier of 1.15 eV [14]. The further decomposition of OH^* to O^* + H^* is even more difficult ($E^‡$ = 1.76 eV, ΔE = 0.48 eV without ZPE corrections) [14], although O^* can be produced by the disproportionation reaction $OH^* + OH^* \longrightarrow O^* + H_2O^*$ ($E^‡$ = 0.23 eV, ΔE = -0.1 eV). While the latter reaction has a low barrier, it consumes OH^*, which itself is difficult to form due to the high barrier for water dissociation. It is thus reasonable to assume that the O^* is a minor species in MSR on Cu(111). As a result, we will only consider reaction pathways initiated by the reaction between CH_2O^* and OH^*. In addition, the recombinative desorption of H_2 and the desorption of CO_2 are not included as these two processes have been extensively studied before on copper surfaces [16, 20]. All of the thermodynamic and kinetic results in Table 3.2 are reported with and without ZPE corrections. The geometries of the initial state (IS), transition states (TS), and final states (FS) in all elementary steps are shown in Fig. 3.2.

Step	Elementary step	$E^{\ddagger}$	ΔE
A1	$CH_2O^* + OH^* \longrightarrow CH_2OOH^*$	0.11(0.11)	-0.64(-0.46)
A2	$CH_2OOH^* \longrightarrow CHOOH^* + H^*$	0.99(0.90)	-0.03(0.09)
A3	$CHOOH(I)^* \longrightarrow CHOOH(II)^*$	0.22(0.23)	0.14(0.15)
A4	$CHOOH(II)^* \longrightarrow cis{-}COOH^{**} + H^*$	1.18(0.98)	0.40(0.26)
A5	$cis{-}COOH^{**} \longrightarrow trans{-}COOH^{**}$	0.53(0.48)	0.02(0.03)
A6	$trans{-}COOH^{**} \longrightarrow CO_2^* + H^*$	1.26(1.02)	-0.46(-0.59)
A6'	$trans{-}COOH^{**} + OH^* \longrightarrow CO_2^* + H_2O^*$	0.04(0.00)	-0.14(-0.14)
B1	$CH_2OOH^* \longrightarrow CH_2OO^{**} + H^*$	1.22(1.02)	0.65(0.51)
B1'	$CH_2OOH^* + OH^* \longrightarrow CH_2OO^{**} + H_2O^*$	0.15(0.05)	0.08(0.06)
B2	$CH_2OO^{**} \longrightarrow CHOO^{**} + H^*$	0.77(0.59)	-0.69(-0.82)
B3	$CHOO^{**} \longrightarrow CHOO^*$	0.55(0.51)	0.53(0.50)
B4	$CHOO^* \longrightarrow CO_2^* + H^*$	0.60(0.45)	-0.20(-0.30)
C1	$CHOOH(I)^* \longrightarrow CHOO^{**} + H^*$	0.66(0.46)	-0.12(-0.22)
C1'	$CHOOH(I)^* + OH^* \longrightarrow CHOO^{**} + H_2O^*$	0.07(0.05)	-0.37(-0.29)

Table 3.2: Calculated activation and reaction energies (eV) for the elementary reactions on Cu(111) studied in this Chapter. Entries in parentheses are the ZPE-corrected values

Pathway A

Pathway A on Cu(111) starts with the reaction between adsorbed formaldehyde (CH_2O^*) and hydroxyl (OH^*):

$$CH_2O^* + OH^* \longrightarrow CH_2OOH^* \longrightarrow CHOOH^* \longrightarrow COOH^{**} \longrightarrow CO_2^*$$

The H^* species is not explicitly included in the reaction sequence for simplicity. The energetics of the pathway is displayed in Fig. 3.3. The first step (A1) is exothermic (ΔE = -0.64 eV) and has a low barrier of 0.11 eV, indicating this reaction will be highly favored. In this step, the OH^* species at an fcc site attacks the weakly bound CH_2O^* molecule to form CH_2OOH^* at the fcc site with oxygen binding with three copper atoms. Both the reaction barrier and exothermicity of A1 indicate that it should be able to compete effectively against the dehydrogenation of CH_2O^* ($E^{\ddagger}$ =

0.66 eV) which eventually leads to CHO^* and CO^* [19]. It should also be favored against the desorption of formaldehyde (E_{ad} = 0.06 eV). The second dehydrogenation step (A2) producing the formic acid ($CHOOH(I)^*$) has, on the other hand, a high barrier (0.99 eV), and is nearly thermoneutral. The length of the breaking C−H bond was found to be 1.60 Å at the transition state. After the C−H bond cleavage, the H^* species moves to an fcc site and $CHOOH(I)^*$ moves to a top site. This orientation of the formic acid adsorbate cannot undergo further dehydrogenation from carbon without a rearrangement (A3) in order to bring the hydrogen on the carbon atom close to the surface. As shown in Fig. 3.2, the transition state for A3 depicts a flip of the adsorbate, yielding the product $CHOOH(II)^*$ which points the carbon hydrogen towards the surface. This step has a small barrier of 0.22 eV and small endothermicity (ΔE = 0.14 eV). The further dehydrogenation of the formic acid (A4) was found to have a large barrier (1.18 eV) and moderate endothermicity (ΔE = 0.4 eV). At the transition state, the breaking C−H bond is elongated to 1.57 Å. The dehydrogenation gives a bidentate carboxyl $COOH^{**}$ and H^* coadsorbed at top and fcc sites, respectively. It should be noted that CHOOH adsorbs weakly on the surface with adsorption energies -0.24 eV for CHOOH(I) and -0.10 eV for CHOOH(II). Therefore desorption would likely be favored over further dehydrogenation without some assistance from a surface hydroxyl or oxygen species. The resulting carboxyl ($COOH^{**}$) isomerizes from cis−$COOH^{**}$ to trans−$COOH^{**}$ (A5) with a moderate barrier of 0.53 eV. This is needed because the H atom in cis−$COOH^{**}$ points away from the surface, as shown in Table 3.1. After isomerization, the hydrogen in trans−$COOH^{**}$ is pointing towards the surface, ideally positioned for the next step. Finally, CO_2^* is produced by removing the hydroxyl hydrogen of trans−$COOH^{**}$ (A6), which features a high barrier of 1.26 eV and exothermicity (ΔE = -0.46 eV). The O−H distance at the transition state is 1.416 Å, and the CO_2^* and H^* species are above the top and hcp sites, respectively. However, this step can also be accomplished by reacting trans−$COOH^{**}$ with OH^* (A6), which has essentially no barrier. As shown in

Fig. 3.2, after dissociation, the hydrogen of the product H_2O^* forms a hydrogen bond with CO_2^*.

The A6 and A6' steps have been investigated before with plane-wave DFT. The barrier heights of 1.41 eV [14] and 1.14 eV [24] for A6 are in reasonable agreement with our value of 1.26 eV. On the other hand, the barrier for A6 was found to be 0.03 eV by Gokhale et al. [14], in good agreement with our value of 0.04 eV.

Pathway B

The second pathway (B) branches off from Pathway A by removing the hydroxyl hydrogen of CH_2OOH^*:

$$CH_2OOH^* \longrightarrow CH_2OO^{**} \longrightarrow CHOO^* + CO_2^*$$

The direct O−H bond cleavage (B1) has a high barrier (1.22 eV) and large endothermicity (ΔE = 0.65 eV). The breaking O−H bond length is 1.66 Å at the transition state and after the bond scission, the bidentate CH_2OO^{**} species prefers to locate at bridge-bridge site and H^* locates on an hcp site. However, the production of CH_2OO^{**} can also be achieved by reacting CH_2OOH^* with OH^* (B1), which is almost thermoneutral (ΔE = 0.08 eV) and has a lower barrier of 0.15 eV. (We note in passing that the CH_2OO^{**} species cannot be formed directly via the reaction between CH_2O^* and OH^*, based on our calculations. It has to go through the CH_2OOH^* intermediate (A1).) In the initial state of B1, CH_2OOH^* and OH^* are coadsorbed on the surface through a hydrogen bond with the length of 1.68 Å, as shown in Fig. 3.2. At the corresponding transition state, the distance of the dissociating O−H bond was found to be 1.30 Å. The resulting dioxomethylene dehydrogenates in B2 to form the bidentate formate ($CHOO^{**}$), which has a large exothermicity (ΔE = -0.69 eV) and a moderate barrier of 0.77 eV. This O−H bond scission on Cu(111) surface proceeded from an initial bridge-bridge site to a top-top site for $CHOO^{**}$

and a fcc site for H^*, respectively. To produce CO_2^*, $CHOO^{**}$ first has to convert from the bidentate adsorption configuration to a unidentate one (B3) on an hpc site, which involves a barrier of 0.55 eV and ΔE of 0.53 eV. The final product (CO_2^*) is produced by dehydrogenation of unidentate formate (B4) with a barrier of 0.60 eV. At the transition state, the C−H distance is calculated to be 1.54 Å and after dehydrogenation, the product H^* locates at an hcp site. The energetics of this pathway is given in Fig. 3.3.

Our B2 barrier height of 0.77 eV is in reasonably good agreement with the calculated values reported in the literature. For example, Mei et al. [46] have found a barrier of 0.85 eV while Yang et al. [15] reported a value of 0.9 eV. The conversion of $CHOO^{**}$ to CO_2^* has also been studied theoretically before by several authors [14, 46]. The calculated overall barrier heights of 1.30 eV [46], and 1.29 eV [14], are in good agreement with our value of 1.13 eV (B3 + B4). These theoretical values are also consistent with experimental results in the literature (1.17 ± 0.13 eV [52] and 1.12 ±0.03 eV [53]).

Pathway C

The third pathway (C) bypasses the dioxomethylene by removing the hydroxyl hydrogen in formic acid:

$$CHOOH^* \longrightarrow CHOO^* \longrightarrow CO_2^*$$

As in Pathway B, the first step of Pathway C can be accomplished in two ways. The direct dehydrogenation (C1) has a moderate barrier (0.66 eV) and is slightly exothermic (ΔE = -0.12 eV). As shown in Fig 3.2, in the initial state, the hydroxyl hydrogen of $CHOOH^*$ points towards the surface. At the transition state, the $CHOO^{**}$ and H^* are at top and fcc sites, respectively and the distance of the dissociating O−H bond is 1.55 Å. On the other hand, the reaction of $CHOOH^*$ with OH^* is essentially

barrierless and has a larger exothermicity (ΔE = -0.37 eV). Similarly to the reaction (B1), the $CHOOH^*$ and OH^* species form an initial state with a hydrogen bond between the two. After reaction, the products $CHOO^{**}$ and H_2O^* were found to coadsorb at top-top and top sites, respectively. The B and C Pathways share the same last steps. The relevant energetics is given in Fig. 3.3.

Role of hydroxyl in dehydrogenation of CH_xO_y species.

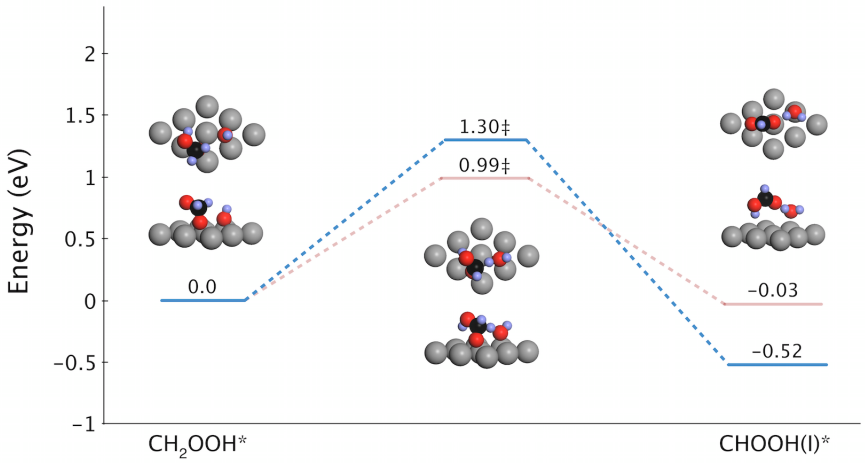

Figure 3.4: Energetics (blue) and geometries of the $CH_2OOH^* + OH^* \longrightarrow CHOOH^* + H_2O^*$ reaction. The energetic of the A2 reaction is also given (red) for comparison.

An important caveat is in order concerning the reaction network proposed in Fig. 3.1. We only consider several most probably reaction pathways in this work, and our proposal is by no means exhaustive. One such possibility not considered in our model is the OH^* assisted removal of hydrogen bonded to carbon, such as the reaction $CH_2OOH^* + OH^* \longrightarrow CHOOH^* + H_2O^*$. To test this possibility, we have computed the reaction path for this process. As shown in Fig. 3.4, the barrier is 1.38 eV (without ZPE correction), higher than the corresponding process without OH^*, namely A2 which has a barrier of 0.99 eV. Our results are consistent with the earlier work of

Gokhale et al. [14], in which it has been shown that the barrier for the $CHOO^{**}$ + $OH^{*} \longrightarrow CO_2^{*} + H_2O^{*} + {}^{*}$ reaction is higher than the direct dehydrogenation of $CHOO^{**}$ on Cu(111). Based on these observations, it is reasonably safe to conclude that the involvement of OH^{*} is unlikely to lower the barrier in such a reaction.

3.4 Discussion

Several observations are immediately in order. First, the reaction between formaldehyde (CH_2O^{*}) and hydroxyl (OH^{*}), namely A1, is strongly favored both thermodynamically and kinetically over the dehydrogenation of formaldehyde on Cu(111), which eventually leads to CO^{*}. The barrier and exothermicity of the former (0.11 and -0.46 eV obtained in this work) are much more favorable compared to latter (0.66 and 0.26 eV reported by Lim et al. [19]). Furthermore, A1 should be able to compete effectively with desorption of formaldehyde as well, given the endothermicity of 0.06 eV for the desorption process. These results are consistent with the observed small amount of formaldehyde in MSR and help to explain the high selectivity towards the CO2 product in MSR. For comparison, the dehydrogenation of CH_2O^{*} on Pd(111) has a smaller barrier (0.22 eV) and large exothermicity (-0.67) [19], which explains why Pd is not a selective MSR catalyst.

Second, the involvement of OH^{*} seems to have a dramatic effect in lowering the barriers of reactions involving the cleavage of an O−H bond. For instance, the direct removal of the hydroxyl hydrogen in $COOH^{**}$ (A6) has a high barrier of 1.26 eV, which can be reduced to 0.04 eV if the hydrogen is abstracted by OH^{*}. Similarly, the barrier for direct dehydrogenation of CH_2OOH^{*} to CH_2OO^{**} (B1) of 1.22 eV is reduced to 0.15 eV if OH^{*} is involved. Such dramatic lowering of reaction barriers have been extensively discussed in the literature for the gas-water shift reaction [14]. Recall that the barrier for the formation of OH^{*} from the decomposition of H_2O^{*}

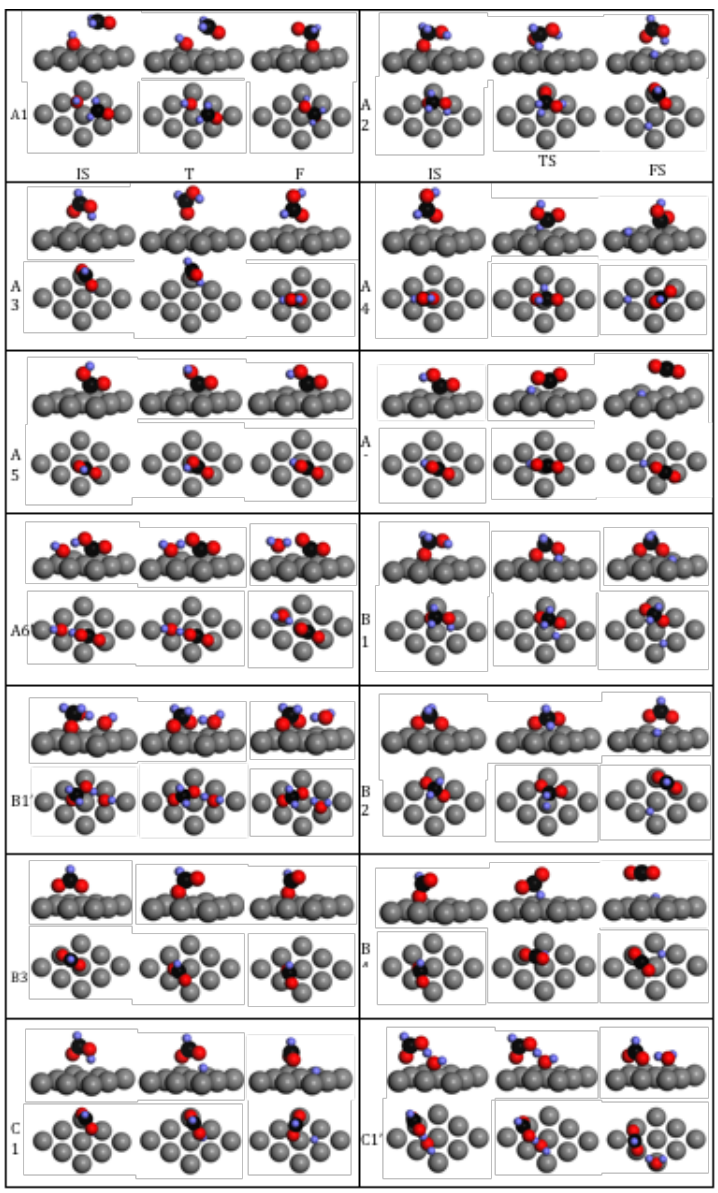

Figure 3.2: Side and top views of the initial states (IS), transition states (TS), and final states (FS) for the elementary reactions listed in Table 3.1

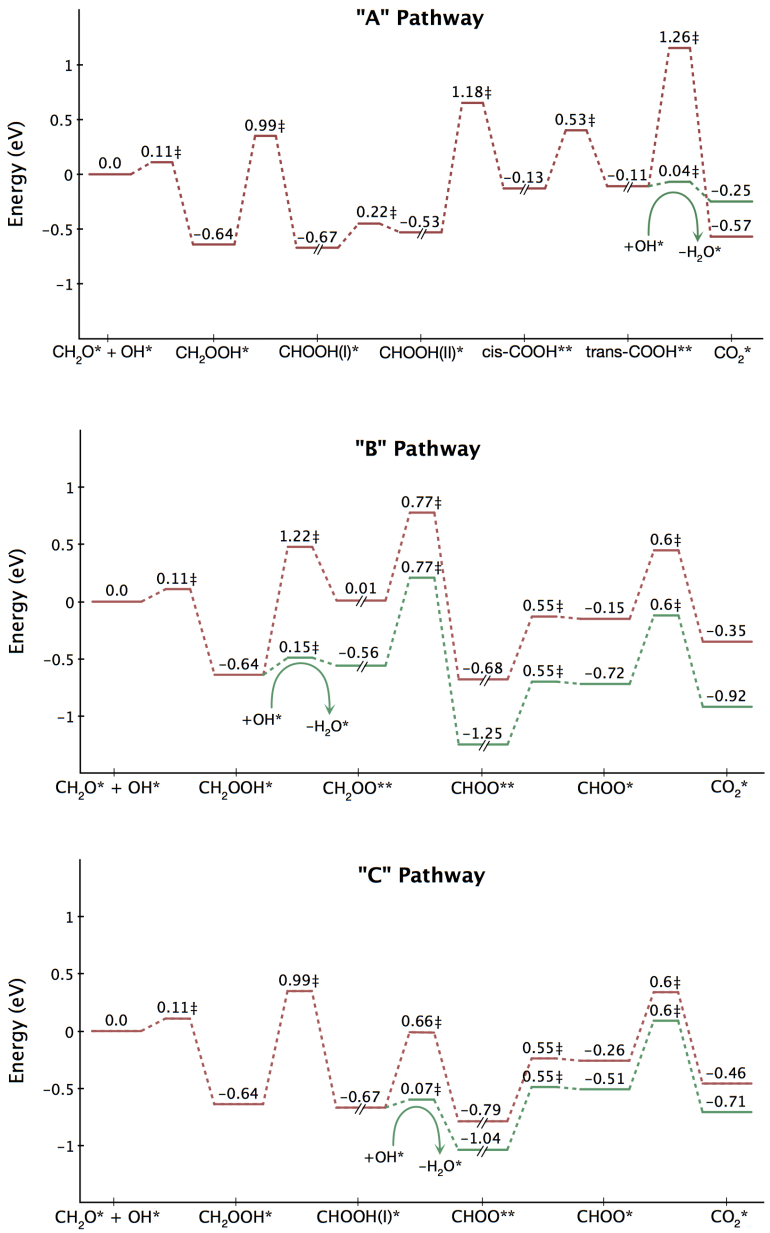

Figure 3.3: Energetics of three possible pathways initiated by the reaction between formaldehyde (CH_2O^*) and hydroxyl (OH^*). The green and red lines denote pathways with and without the involvement of the OH^* species, respectively. When a break symbol (//) is present, an H^* species is removed from the next step of the calculation.

is 1.15 eV, lower than both of those in the aforementioned direct dehydrogenation reactions. Thus, it is still advantageous to proceed with OH^* for these two elementary steps. We also note that the involvement of OH^* in cleaving a C−H bond in an adsorbate is not effective.

If the OH^* involved reactions are considered to dominate, it follows that the Pathway A is not competitive because of the high barrier (1.18 eV) involved in the conversion of formic acid ($HCOOH^*$) to carboxyl ($COOH^{**}$). On the other hand, both Pathways B and C are viable as the highest barrier is only 0.77 eV and 0.99 eV, respectively, which are lower than that for the putative rate-limiting step, namely the dehydrogenation of methoxyl (1.16 eV) [17]. Even when reactions with OH^* are excluded, Pathway A is still not viable because of the high barrier in the conversion of carboxyl to carbon dioxide (A6). Under such circumstances, the cross-over pathway (C) becomes the most favorable with the highest barrier (0.99 eV) involving the conversion of CH_2OOH^* to formic acid ($HCOOH^*$). This contrasts with a barrier of 1.22 eV in the B Pathway. Thus, Pathway C would be consistent with experimental data on the rate-limiting step of MSR [10, 11, 25, 26]. However, it might be premature to predict the dominant pathway for the MSR based on the energetics reported here alone. Detailed micro kinetic modeling is required to make definitive statements on the dominant reaction pathway.

As mentioned earlier, the newly discovered PdZn catalyst for MSR might have the same mechanism as Cu. Indeed, it is established theoretically that the dehydrogenation of methoxyl (CH_3O^*) is also the rate-limiting step on defect free PdZn alloy surfaces [17, 54], although the initial O−H bond cleavages of both H_2O and CH_3OH are highly activated [55, 56]. Furthermore, DFT studies have suggested that the dehydrogenation of formaldehyde (CH_2O^*) on PdZn surfaces has a high barrier, qualitatively similar to that on Cu(111) but different from Pd(111) [19]. The difficulties for decomposing CH_3OH to CO product on PdZn surfaces predicted by DFT

has recently been experimentally confirmed [57]. However, no theoretical studies have yet been reported on the reactions between the formaldehyde and hydroxyl intermediates.

It might also be interesting to comment on the implications of our results in the context of methanol synthesis: $CO_2 + 3\,H_2 \longrightarrow H_2O + CH_3OH$, which is the reverse of MSR and uses the same copper catalyst. A recent study [15] explored this reaction in detail and identified a path that is very similar to the Pathway B presented here. If we consider the reverse of the B2 reaction ($CHOO^{**}$ to CH_2OO^{**}), we have a barrier of 1.46 eV and ΔE of +0.69 eV. These values compare well with 1.60 eV and +0.70 eV reported by Yang et al. [15] However, the reverse of the subsequent steps (B1 and A1) is a two step scheme in our study with a CH_2OOH^* intermediate and barriers of 0.57 eV (B1 reverse) and 0.75 eV (A1 reverse), compared to their reported single step reaction with barrier 1.60 eV. Further, no report on the reverse of the Pathway C was discussed in their study, where we have obtained the reverse barriers of 0.78 eV (C1), 1.02 eV (A2), and 0.75 eV (A1). Our calculations suggest the reverse Pathway C would be favored for methanol synthesis on Cu(111).

3.5 Conclusions

Despite its importance in energy science, the methanol steam reforming (MSR) mechanism has not yet been fully elucidated. Experimental evidence has identified several key intermediates, such as methoxyl (CH_3O^*) and formaldehyde (CH_2O^*), but their involvements in the reaction network has not been firmly established. In this work, we explore several pathways leading to the $CO_2 + H_2$ products initiated by the reaction between CH_2O^* and OH^* on Cu(111), using a plane-wave DFT method. Our computational results indicate several plausible pathways, which involves species such as formic acid ($CHOOH^*$), dioxomethylene (CH_2OO^{**}), and formate ($CHOO^{**}$). Ener-

getics of these pathways suggests that the one with carboxyl ($COOH^{**}$) intermediate is not viable due to high barriers. Our pathways are not only consistent with several mechanistic proposals in the literature [26], but also provide much more microscopic details as well as energetics. These plausible pathways involve barriers that are less than the rate-limiting step of methoxyl dehydrogenation, thus are consistent with experimental observations. The energetics reported here can be combined with previous DFT results to establish a kinetic model for MSR and help to map out the complicated reaction network in this important heterogeneous catalytic process.

References

[1] D. L. Trimm and Z. I. Önsan, "Onboard fuel conversion for hydrogen-fuel-cell-driven vehicles," *Catalysis Reviews*, vol. 43, no. 1-2, pp. 31–84, 2001.

[2] L. F Brown, "A comparative study of fuels for on-board hydrogen production for fuel-cell-powered automobiles," *International Journal of Hydrogen Energy*, vol. 26, no. 4, pp. 381–397, 2001.

[3] D. R. Palo, R. A. Dagle, and J. D. Holladay, "Methanol Steam Reforming for Hydrogen Production," *Chemical Reviews*, vol. 107, pp. 3992–4021, Oct. 2007.

[4] S. Sá, H. Silva, L. Brandão, and J. Sousa, "Catalysts for methanol steam reforming-a review," *Applied Catalysis B: ...*, 2010.

[5] G. Olah, "After oil and gas: methanol economy," *Catalysis Letters*, 2004.

[6] N. Iwasa and N. Takezawa, "New supported Pd and Pt alloy catalysts for steam reforming and dehydrogenation of methanol," *Topics in Catalysis*, vol. 22, no. 3, pp. 215–224, 2003.

[7] Z.-X. Chen, K. M. Neyman, A. B. Gordienko, and N. Rösch, "Surface structure and stability of PdZn and PtZn alloys: Density-functional slab model studies," *Physical Review B*, vol. 68, no. 7, p. 075417, 2003.

[8] A. P. Tsai, S. Kameoka, and Y. Ishii, "PdZn=Cu: Can an Intermetallic Compound Replace an Element?," *Journal of the Physical Society of Japan*, vol. 73, pp. 3270–3273, Dec. 2004.

[9] P. Pfeifer, A. Kölbl, and K. Schubert, "Kinetic investigations on methanol steam reforming on PdZn catalysts in microchannel reactors and model transfer into the pressure gap region," *Catalysis today*, vol. 110, no. 1, pp. 76–85, 2005.

[10] C. J. Jiang, D. L. Trimm, M. S. Wainwright, and N. W. Cant, "Kinetic study of steam reforming of methanol over copper-based catalysts," *Applied Catalysis A: General*, vol. 93, pp. 245–255, Jan. 1993.

[11] B. Peppley, J. Amphlett, L. Kearns, and R. Mann, "Methanol-steam reforming on Cu/ZnO/Al 2 O 3. Part 1: the reaction network," *Appl. Catal. A: Gen*, vol. 179, no. 1, pp. 21–29–29, 1999.

[12] J. Greeley, J. K. Nørskov, and M. Mavrikakis, "Electronic Structure and Catalysis on Metal Surfaces," *Annual review of physical . . .*, vol. 53, no. 1, pp. 319–348, 2002.

[13] K. Honkala, A. Hellman, I. Remediakis, and A. Logadottir, "Ammonia synthesis from first-principles calculations," *Science*, 2005.

[14] A. Gokhale, J. Dumesic, and M. Mavrikakis, "On the Mechanism of Low-Temperature Water Gas Shift Reaction on Copper," *Journal of the American Chemical Society*, 2008.

[15] J. A. Rodriguez, "Fundamental studies of methanol synthesis from CO 2 hydrogenation on Cu (111), Cu clusters, and Cu/ZnO (0001)," *Physical Chemistry . . .*, 2010.

[16] J. Greeley and M. Mavrikakis, "Methanol decomposition on Cu (111): A DFT study," *Journal of Catalysis*, 2002.

[17] Z.-X. Chen, K. M. Neyman, K. H. Lim, and N. Rösch, "CH3O decomposition on PdZn(111), Pd(111), and Cu(111). A theoretical study.," *Langmuir*, vol. 20, pp. 8068–8077, Sept. 2004.

[18] S. Sakong and A. Groß, "Density functional theory study of the partial oxidation of methanol on copper surfaces," *Journal of Catalysis*, vol. 231, no. 2, pp. 420–429, 2005.

[19] K. H. Lim, Z.-X. Chen, K. M. Neyman, and N. Rösch, "Comparative Theoretical Study of Formaldehyde Decomposition on PdZn, Cu, and Pd Surfaces," *The Journal of Physical Chemistry B*, vol. 110, pp. 14890–14897, Aug. 2006.

[20] S. Sakong and A. Groß, "Total Oxidation of Methanol on Cu(110): A Density Functional Theory Study," *The Journal of Physical Chemistry A*, vol. 111, pp. 8814–8822, Sept. 2007.

[21] Q.-L. Tang and Z.-X. Chen, "Influence of aggregation, defects, and contaminant oxygen on water dissociation at Cu(110) surface: a theoretical study.," *The Journal of Chemical Physics*, vol. 127, p. 104707, Sept. 2007.

[22] Q.-L. Tang and Z.-X. Chen, "Density functional slab model studies of water adsorption on flat and stepped Cu surfaces," *Surface Science*, vol. 601, no. 4, pp. 954–964, 2007.

[23] D. Mei, L. Xu, and G. Henkelman, "Potential Energy Surface of Methanol Decomposition on Cu (110)," *The Journal of Physical Chemistry C*, vol. 113, no. 11, pp. 4522–4537, 2009.

[24] Q.-L. Tang, Z.-X. Chen, and X. He, "A theoretical study of the water gas shift reaction mechanism on Cu (1 1 1) model system," *Surface Science*, vol. 603, no. 13, pp. 2138–2144, 2009.

[25] J. K. Lee, J. B. Ko, and D. H. Kim, "Methanol steam reforming over Cu/ZnO/Al 2 O 3 catalyst: kinetics and effectiveness factor," *Applied Catalysis A: General*, vol. 278, no. 1, pp. 25–35, 2004.

[26] B. Frank, F. Jentoft, H. Soerijanto, and J. Kröhnert, "Steam reforming of methanol over copper-containing catalysts: Influence of support material on microkinetics," *Journal of Catalysis*, 2007.

[27] K. Takahashi, H. Kobayashi, and N. Takezawa, "On the difference in reaction pathways of steam reforming of methanol over copper-silica and platinum-silica catalysts," *Chemistry Letters*, no. 6, pp. 759–762, 1985.

[28] I. E. Wachs and R. J. Madix, "The selective oxidation of CH3OH to H2CO on a copper(110) catalyst," *Journal of Catalysis*, vol. 53, no. 2, pp. 208–227, 1978.

[29] M. Bowker and R. J. Madix, "XPS, UPS and thermal desorption studies of alcohol adsorption on Cu(110): I. Methanol," *Surface Science*, vol. 95, no. 1, pp. 190–206, 1980.

[30] I. A. Fisher and A. T. Bell, "A Mechanistic Study of Methanol Decomposition over Cu/SiO 2, ZrO 2/SiO 2, and Cu/ZrO 2/SiO 2," *Journal of Catalysis*, vol. 184, no. 2, pp. 357–376, 1999.

[31] K. Takahashi, N. Takezawa, and H. Kobayashi, "The mechanism of steam reforming of methanol over a copper-silica catalyst," *Applied Catalysis*, vol. 2, no. 6, pp. 363–366, 1982.

[32] N. Takezawa and N. Iwasa, "Steam reforming and dehydrogenation of methanol: Difference in the catalytic functions of copper and group VIII metals," *Catalysis today*, vol. 36, no. 1, pp. 45–56, 1997.

[33] M. Bowker and R. J. Madix, "XPS, UPS and thermal desorption studies of the reactions of formaldehyde and formic acid with the Cu(110) surface," *Surface Science*, vol. 102, no. 2â"3, pp. 542–565, 1981.

[34] G. Kresse and J. Hafner, "Abinitio Molecular-Dynamics for Liquid-Metals," *Physical Review B*, vol. 47, no. 1, pp. 558–561, 1993.

[35] G. Kresse and J. Furthmüller, "Efficient iterative schemes for ab initio total-energy calculations using a plane-wave basis set," *Physical Review B*, vol. 54, pp. 11169–11186, Oct. 1996.

[36] G. Kresse and J. Furthmüller, "Efficiency of ab-initio total energy calculations for metals and semiconductors using a plane-wave basis set," *Computational Materials Science*, vol. 6, pp. 15–50, July 1996.

[37] J. P. Perdew, K. Burke, and Y. Wang, "Generalized gradient approximation for the exchange-correlation hole of a many-electron system," *Physical review B, Condensed matter*, vol. 54, pp. 16533–16539, Dec. 1996.

[38] P. Blöchl, "Projector augmented-wave method.," *Physical review B, Condensed matter*, vol. 50, pp. 17953–17979, Dec. 1994.

[39] G. Kresse and D. Joubert, "From ultrasoft pseudopotentials to the projector augmented-wave method," *Physical Review B*, vol. 59, no. 3, p. 1758, 1999.

[40] H. J. Monkhorst and J. D. Pack, "Special points for Brillouin-zone integrations," *Physical review B, Condensed matter*, vol. 13, no. 12, pp. 5188–5192, 1976.

[41] M. Methfessel and A. Paxton, "High-precision sampling for Brillouin-zone integration in metals.," *Physical review B, Condensed matter*, vol. 40, pp. 3616–3621, Aug. 1989.

[42] *CRC Handbook of Chemistry and Physics*. New York: CRC press, 1996.

[43] H. Jonsson, G. Mills, and K. W. Jacobsen, "Nudged elastic band method for finding minimum energy paths of transitions," in *Classical and Quantum Dynamics in Condensed Phase Simulations* (B. J. Berne, G. Ciccotti, and D. F. Coker, eds.), Singapore: World Scientific, 1998.

[44] G. Henkelman, B. P. Uberuaga, and H. Jonsson, "A climbing image nudged elastic band method for finding saddle points and minimum energy paths," *The Journal of Chemical Physics*, vol. 113, no. 22, pp. 9901–9904, 2000.

[45] J.-Y. Bo, S. Zhang, and K. H. Lim, "Steam Reforming of Formaldehyde on Cu (100) Surface: A Density Functional Study," *Catalysis Letters*, vol. 129, pp. 444–448, Jan. 2009.

[46] D. Mei, L. Xu, and G. Henkelman, "Dimer saddle point searches to determine the reactivity of formate on Cu (111)," *Journal of Catalysis*, vol. 258, no. 1, pp. 44–51, 2008.

[47] D. H. S. Ying and R. J. Madix, "Thermal desorption study of formic acid decomposition on a clean Cu(110) surface," *Journal of Catalysis*, vol. 61, no. 1, pp. 48–56, 1980.

[48] G. Wang, Y. Morikawa, T. Matsumoto, and J. Nakamura, "Why is formate synthesis insensitive to copper surface structures?," *The Journal of Physical Chemistry B*, vol. 110, no. 1, pp. 9–11, 2006.

[49] A. Sotiropoulos, P. K. Milligan, B. C. C. Cowie, and M. Kadodwala, "A structural study of formate on Cu(111)," *Surface Science*, vol. 444, pp. 52–60, Jan. 2000.

[50] M. D. Crapper, C. E. Riley, D. P. Woodruff, A. Puschmann, and J. Haase, "Determination of the adsorption structure for formate on Cu(110) using SEXAFS and NEXAFS," *Surface Science*, vol. 171, no. 1, pp. 1–12, 1986.

[51] T. Fujitani, Y. Choi, M. Sano, Y. Kushida, and J. Nakamura, "Scanning tunneling microscopy study of formate species synthesized from CO2 hydrogenation and prepared by adsorption of formic acid over Cu (111)," *The Journal of Physical Chemistry B*, vol. 104, no. 6, pp. 1235–1240, 2000.

[52] H. Nishimura, T. Yatsu, T. Fujitani, T. Uchijima, and J. Nakamura, "Synthesis and decomposition of formate on a Cu (111) surface—kinetic analysis," *"Journal of Molecular Catalysis. A, Chemical"*, vol. 155, no. 1, pp. 3–11, 2000.

[53] I. Nakamura, H. Nakano, T. Fujitani, T. Uchijima, and J. Nakamura, "Synthesis and decomposition of formate on Cu(111) and Cu(110) surfaces: Structure sensitivity," *Journal of Vacuum Science & Technology A: Vacuum, Surfaces, and Films*, vol. 17, no. 4, pp. 1592–1595, 1999.

[54] Z.-X. Chen, K. H. Lim, K. M. Neyman, and N. Rösch, "Effect of steps on the decomposition of CH3O at PdZn alloy surfaces.," *The Journal of Physical Chemistry B*, vol. 109, pp. 4568–4574, Mar. 2005.

[55] Y. Huang and Z.-X. Chen, "Density Functional Investigations of Methanol Dehydrogenation on PdZn Surface Alloy," *Langmuir*, vol. 26, pp. 10796–10802, July 2010.

[56] G. K. Smith, S. Lin, W. Lai, A. Datye, D. Xie, and H. Guo, "Initial steps in methanol steam reforming on PdZn and ZnO surfaces: Density functional theory studies," *Surface Science*, vol. 605, pp. 750–759, Apr. 2011.

[57] E. Jeroro and J. M. Vohs, "Zn modification of the reactivity of Pd(111) toward methanol and formaldehyde," *Journal of the American Chemical Society*, vol. 130, no. 31, pp. 10199–10207, 2008.

Chapter 4

The CO oxidation mechanism and reactivity on PdZn alloys

This chapter is based on collaborative work found in the following publication: **R. S. Johnson**, A. DeLaRiva, V. Ashbacher, B. Halevi, C. J. Villanueva, G. K. Smith, S. Lin, A. K. Datye, and H. Guo, *The CO oxidation mechanism and reactivity on PdZn alloys*, Physical Chemistry Chemical Physics, vol. 15, no. 20, pp. 7768-7776, 2013. with permission from the PCCP Owner Societies. Please refer here for full experimental details.

4.1 Introduction

The oxidation of carbon monoxide (CO) to carbon dioxide (CO_2) is one of the most studied reactions in heterogeneous catalysis. Being toxic to life and a product of incomplete combustion of hydrocarbon fuels, CO therefore must be removed from exhaust streams. Additionally, it is one of the simplest redox reactions, converting two reactants to a single product, which quickly desorbs from the surface. In fact, this reaction has even been proposed as an ideal probe for characterizing catalysts for other heterogeneous reactions [1]. Despite its apparent simplicity, however, it has proven to hold remarkable complexity and there are still conflicting views about the nature of the catalyst in its most active working state [2–6]. The development of catalysts capable of performing this exothermic reaction at room temperature still remains a significant goal for industrial applications. These applications include supplying clean H_2 for low temperature fuel cell systems since catalysts for this process are deactivated at low temperatures by exposure to CO. Another application is the scrubbing of industrial gas streams and automotive exhaust [7].

The pioneering work by Ertl et al. [8] applied advanced surface science techniques to this reaction on well-defined single crystal surfaces such as Pd(111). Their work unambiguously identified the reaction mechanism as being Langmuir-Hinshelwood, and uncovered the source of the observed negative reaction order with respect to CO.

These authors observed, with photoemission electron microscopy (PEEM), CO and O forming discrete islands on the surface, the boundaries of which being where the reaction takes place. Interestingly, under high CO concentrations the dissociative adsorption of O_2 is blocked by CO, which has a stronger binding energy. These observations immediately suggest a possible route to enhanced reaction rate, namely by reducing the binding energy of CO, making the adsorption of O_2 more competitive.

The addition of Zn to Pd has been shown to lower the binding energy of CO [9–12]. In fact, a significant change in the CO binding energy occurs even when submonolayer quantities of Zn are deposited onto Pd, and the influence of Zn becomes more pronounced as coverage is increased [9]. However, there are no reports of steady state CO oxidation reactivity measurements on Zn modified Pd surfaces. Early studies focused on well-defined single crystals of either ZnO or Pd, which were then modified by adding Pd or Zn respectively to make thin layers of PdZn on the surface of the support [11, 13–16]. It was quickly realized that both the thickness of the PdZn layer and the support underneath might play an important role in the activity of these catalysts. Additionally, these clean, well-defined surfaces differ significantly and fundamentally from the nanoparticle catalysts used in industrial catalysis. Nanoparticles display both a high surface area and defects, and the latter can significantly affect the catalytic activity. Nanoscale particles of PdZn are usually synthesized by wet-impregnation, and the influence of both particle size and Pd loading has been characterized [17, 18]. Unfortunately, conventional supported catalysts suffer from poor homogeneity in phase, composition, and particle size. Since the activity of Pd is known to change significantly even with small concentrations of Zn, the uncertainty in the phase and composition of these particles poses serious problems for investigating the role of Zn on the catalytic activity of Pd.

The PdZn alloy has multiple phases. Apart from the 1:1 β phase, there exists an α phase with the Zn mole fraction up to about 0.18 at 300K. Control of the

homogeneity and composition in PdZn nanoparticles is quite challenging. Recently, a new synthesis method has been reported where the metals of interest (in the form of metal salts) are sent as an aerosol stream through a furnace [19, 20]. This method produces bimetallic nanoparticles that are homogeneous in both phase and composition, thus facilitating the study of PdZn reactivity and the effect of composition and phase on catalytic performance without the additional complications of a support. We have used these aerosol derived bimetallic samples to investigate whether the reduced binding energy of CO on Zn-modified Pd leads to enhanced CO oxidation reactivity, as summarized in Sec.4.3.1. We also report detailed experimental and density functional theory (DFT) studies of the CO oxidation reaction on Pd, and both the α and β phases of the PdZn alloy.

4.2 Theoretical Methods

Periodic plane wave DFT calculations were performed using the PW91 functional [21] as implemented in the Vienna Ab Initio Package (VASP [22–24]). Core electrons are approximated with the PAW pseudopotentials [25, 26] and the plane wave basis was truncated above 400 eV. In this work, we have used the (111) face to represent the catalysts surfaces. The β-PdZn(111) and Pd(111) surfaces were modeled with 2x2 unit cells, 4 and 3 layers, respectively; and constructed at the DFT optimized lattice parameters ($a = b = c = 3.97$ Å for Pd, $a = b = 4.139$ Å, $c = 3.378$ Å for β-PdZn). The α-PdZn surfaces were modeled with a 3×3 unit cell, 3 layers deep. This larger slab was chosen in order to accurately model this low zinc concentration phase. The 1-Zn slab was comprised of 27 Pd atoms and the Zn atom in the top layer, resulting in a slab with Zn mole fraction of 0.04 and was built at the DFT optimized Pd lattice parameters. The 2-Zn slab was identical to the 1-Zn slab with an additional Zn atom in the top most layer, resulting in a mole fraction of 0.07.

Partial occupancies were determined using Methfessel-Paxton smearing [27] with a width of 0.1 eV. k-point sampling was carried out using the method of Monkhorst and Pack [28] with a $4 \times 4 \times 1$ grid for Pd, β-PdZn, and α-PdZn. A vacuum space of 14 Å was used in the z direction. For all surfaces the top layer was first relaxed, and then fixed at the clean slab geometry for all further calculations. Including the top layer in the geometry optimizations resulted in a change of binding energies less than 0.1 eV.

Adsorption energies were calculated in the usual way. For adsorbed oxygen atoms, the binding energy is referenced to either O(g) or $\frac{1}{2}O_2$(g). For adsorbed CO, we have used the method developed by Abild-Pedersen and Andersson [29] to correct the well-known intrinsic overbinding (OB) error of CO on metal surfaces in DFT calculations, which stems from the underestimation of the energy of the $2\pi^*$ orbital of CO. The empirical correction (in eV) is given as follows:

$$E_{\mathrm{cor}} = 1.8 - 0.0008 \times v_{\mathrm{CO}}$$

where v_{CO} is the CO stretching frequency in wavenumbers, determined by finite difference.

Activation energies for reactions were obtained with the climbing-image nudged elastic band method (CI-NEB) [30, 31], with energy (10^{-4} eV) and force (0.05 eV/Å) convergence criteria. All stationary points were confirmed by normal mode analysis.

4.3 Results

4.3.1 Experimental

The key experimental results are summarized in Table 4.1. Samples of phase pure Pd metal, α-PdZn and β-PdZn were synthesised and test for CO oxidation activity.

Sample	Reaction Order		CO desorption		TOF (185°C)
	Order in CO	Order in O_2	T_{desorp} (K)	E_{desorp} (kJ mol^{-1}/eV)	s^{-1}
Pd Metal	-1	1	530	150/1.55	0.055
α-PdZn	-0.6	0.6	450	125/1.30	0.11
β-PdZn	-0.4	0.6	420	120/1.24	0.075

Table 4.1: Summary of various experimental results, namely the reaction orders for CO oxidation at 185°C , desorption temperature and desorption energy of CO, and steady-state turnover frequencies for CO oxidation on Pd metal powders and PdZn alloys.

It was found that the initial CO oxidation reactivity (per Pd surface atom) could be 10 times higher on the α-PdZn surface and about 5 times higher on the β-PdZn surface, compared to metallic Pd. However, the high initial activity is lost during CO oxidation presumably due to the fact that the Zn becomes oxidized and is no longer available. Fig. 4.1 shows how the specific activity for the PdZn α and β samples decays within the first hour, and approaches the value for Pd metal (which is shown as a horizontal dotted line). The α-PdZn surface remains slightly more active than Pd metal, even at steady state.

4.3.2 Theoretical

Adsorption

We first screened all surfaces for binding energies of O and CO at all unique binding sites. The results are given in Tables 2 and 3, along with comparison with previous theoretical and experimental results. These calculated adsorption energies are in good agreement with values found by previous researchers [9, 12, 29, 33–35].

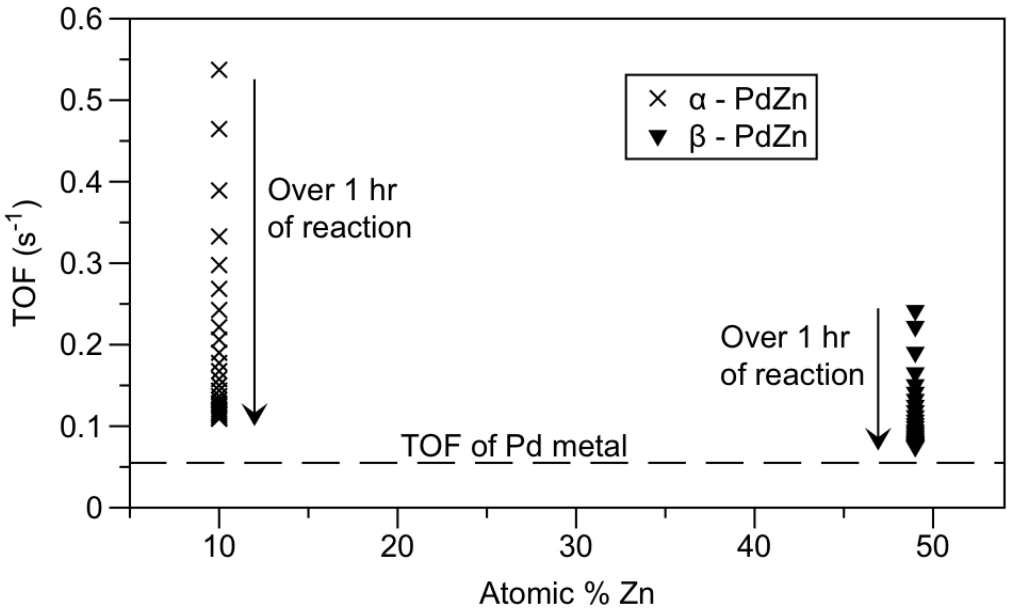

Figure 4.1: TOF as a function of time. This plot clearly demonstrates the deactivation of PdZn catalysts. Over time both drop towards the TOF of Pd metal (here shown as black dotted line)

Pd(111)

On Pd(111), several binding sites were found for CO. The most stable one is the hcp hollow site, which is closely followed by the fcc hollow site. At low coverages, CO is found experimentally to adsorb at hollow sites [36], with perhaps a slight preference to fcc [37, 38]. The adsorption energies of these two sites after the OB correction are in good agreement with experimental value of -1.47 eV [33]. The top site adsorption was the least stable and the bridge site is in between. Our calculated adsorption energies shown in Table 4.2 are similar to those found in other studies [29, 32, 34, 39]. The relatively small differences between our values and other reported values can presumably be attributed to the different functional and pseudopotentials used. The adsorption energy is also in good agreement with the

Surface	Site	E_{ads} (OB) Theo. (This work)	E_{ads} (OB) Theo.	E_{ads} Expt.
β-PdZn	T-Pd	-1.00 (-0.78)	-0.9938	
	B-Pd_2	-0.95 (-0.63)		
α-PdZn	T_1	-1.42 (-1.25)		-1.3
(1-Zn)	T_2	-1.47 (-1.31)		(this work)
	H_1	-1.99 (-1.62)		
	F_1	-1.94 (-1.58)		
	B_2	-1.83 (-1.51)		
	B_3	-1.75 (-1.44)		
α-PdZn	$T_{1,1}$	-1.33 (-1.17)		
(2-Zn)	$T_{2,1}$	-1.34 (-1.17)		
	$T_{2,2}$	-1.43 (-1.26)		
	$H_{1,1}$	-1.88 (-1.51)		
	$F_{1,1}$	-1.90 (-1.53)		
	$B_{1,1}$	-1.55 (-1.25)		
	$B_{2,2}$	-1.74 (-1.42)		
Pd	H-hcp	-1.97 (-1.55)	-1.83 [32], (-1.37) [29]	-1.47 [33], -1.55 (this work)
	H-fcc	-1.92 (-1.51)	-2.07 [34], -1.85 [32], (-1.36) [29]	
	T-Pd	-1.41 (-1.20)	-1.27 [32], (-0.98) [29]	
	B-Pd_2	-1.79 (-1.44)	(-1.26) [29]	

Table 4.2: Calculated CO adsorption energies (eV) on three surfaces and comparison with experimental and previous theoretical values (overbinding corrected values are given in parentheses). The most favorable sites are underlined.

value of 150 kJ/mol (1.55 eV) estimated from the desorption temperature of 530K for CO on Pd metal powder [20, 40] (see Table 4.1).

Our DFT calculations indicated that oxygen also prefers hollow sites, either fcc or hcp. The adsorption energies are similar for these two sites, and much larger than that for the top site. As shown in Table 4.2, our results are similar to previous theoretical values [32, 34]. It should be pointed out that the values listed in the table are referenced to the gas phase oxygen atom. If molecular oxygen is used as the reference, adsorption energies are generally reduced by 2.5eV.

β-PdZn On the (111) face of β-PdZn, CO is found to adsorb preferentially on the Pd top site. The overbinding corrected adsorption energy of -0.78 eV is consistent with both experimental TPD data [9, 12] and an earlier DFT value [32] reported in the literature, as shown in Table 4.2. Overall, the binding energy is significantly smaller than that on Pd(111), due apparently to the abundant Zn atoms nearby. Interestingly, the recent experimental work on PdZn powders seems to suggest a much larger binding energy for CO (-1.24 eV) [19], which is likely due to multiple re-adsorption events in the experiment and therefore an increase in binding energy when compared to the ideal desorption energy measured in a single turnover experiment [41].

Oxygen, on the other hand, prefers to adsorb at hollow sites. Most stable is the $PdZn_2$ site, followed by the Pd_2Zn site. The adsorption energies are consistent with the previous theoretical values [32], as shown in Table 4.3.

α-PdZn The α-PdZn surfaces (Zn in substitutional sites in fcc Pd) have not been previously studied via DFT methods, and as a result a thorough investigation has been carried out. In our 1-Zn model, the sole Zn atom replaces a Pd atom on the (111) surface. To label the binding sites on the alpha slab we use the symbol S_d, where S is a letter denoting the site (T for top, B for bridge, H and F for hcp and fcc

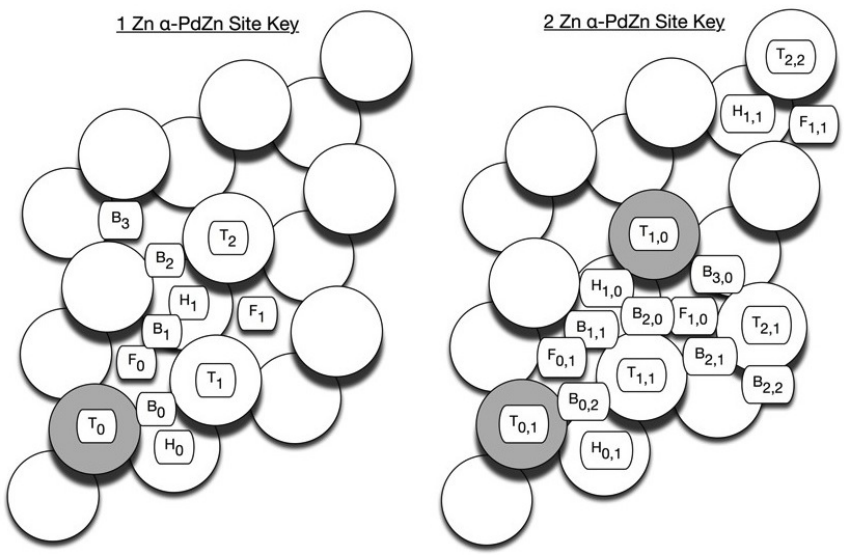

Figure 4.2: Adsorption sites studied on the α-PdZn model surfaces.

hollows sites, respectively) and d indicates the relative distance from the zinc atom. For example, T_0 refers to the atop zinc site and H_1 is the hcp hollow one hcp site away from the zinc, as is shown in Fig. 4.2. The adsorption energies for several sites are listed in Table 4.2. It was found that CO avoids the immediate vicinity of the Zn atom in the surface. Not surprisingly, the adsorption energies are significantly larger Based on the experimental CO desorption temperature of 450K (Table 4.1), we estimated the desorption energy of 125 kJ/mol (1.30 eV).

Oxygen binding weakens as the sites approach the Zn atom. Comparing top sites T_0, T_1 and T_2; the binding energy is -2.52 eV, -3.09 eV, and -3.16 eV. A similar trend is noted for hollow sites as well. We can also clearly see that the hcp sites are more stable than the fcc sites. This trend is the opposite on Pd(111), where fcc sites are more stable.

On the 2-Zn atom slab, where a slightly higher Zn concentration is modelled, there are 17 unique binding sites, which have been investigated. The labelling scheme we

have adopted for this slab is similar to that of the 1-Zn α-PdZn except with two subscripts denoting the relative distance from each Zn atom. For example, $T_{0,1}$ is equivalent to T_0 in the 1-Zn system and $B_{1,1}$ is the bridge site equidistant between the two Zn atoms and is shown in Fig. 4.2. We find that the general trend established by the other three slabs is retained; the binding energy of CO is reduced with more Zn, CO binds less favorably near Zn atoms and CO prefers three fold hollow sites followed by bridge and then top sites. Oxygen binding energies are similar to the 1-Zn slab and it prefers binding to threefold hollow sites in the vicinity of the Zn atoms. All binding energies are summarized in Table 4.2.

Reaction Barriers

The calculated reaction barriers are summarized in Table 4.4. The reaction of adsorbed CO with O proceeds on all surfaces in very similar fashion. The initial state has the oxygen in a hollow site and the CO bound to an adjacent hollow (Pd) or the top site of Pd (α and β-PdZn). The initial states were chosen based on the most favorable adsorption energies for the two species. While only one single initial state was considered for the Pd and β-PdZn surfaces, three unique coadsorbed states were considered for α-PdZn. These configurations, labeled A, B, and C, have coadsorbed adsorption energies of -5.83, -5.70 and -6.01 eV, respectively.

The CO oxidation on the Pd(111) surface has a barrier of 0.88 eV and an exothermicity of -0.70 eV. These values are consistent with the recent theoretical work of Zhang and Hu [42]. The same reaction on β-PdZn(111) has a much lower barrier (0.59 eV) and larger exothermicity (-0.90 eV). To our best knowledge, there has not been any theoretical study of this reaction on any PdZn surfaces.

On the 1-Zn α-PdZn surface, the CO oxidation in the A configuration, in which the oxygen is at the H_0 site and the carbon monoxide is on T_2 site, has a barrier of

Surface	Site	Eads Theo. (This work) ref. to O/ ref to $\frac{1}{2}O_2$	Eads Theo.
β-PdZn	H-$PdZn_2$	-4.85 / -2.35	-4.6538 [32]
	H-Pd_2Zn	-4.34 / -1.84	-4.1038 [32]
α-PdZn (1-Zn)	T_0	-2.52 / -0.02	
(1-Zn)	T_1	-3.09 / -0.59	
	T_2	-3.16 / -0.66	
	H_0	-4.19 / -1.69	
	F_0	-4.35 / -1.85	
	H_1	-4.29 / -1.79	
	F_1	-4.57 / -2.07	
α-PdZn	$T_{0,1}$	-2.62 / -0.12	
(2-Zn)	$T_{1,0}$	-2.62 / -0.12	
	$T_{1,1}$	-3.05 / -0.55	
	$T_{2,2}$	-3.17 / -0.67	
	$H_{0,1}$	-4.20 / -1.70	
	$F_{0,1}$	-4.35 / -1.85	
	$H_{1,0}$	-4.15 / -1.65	
	$F_{1,0}$	-3.35 / -0.85	
	$H_{1,1}$	-4.24 / -1.74	
	$F_{1,1}$	-4.51 / -2.01	
	$B_{2,2}$	-4.05 / -1.55	
Pd	H-hcp	-4.41 / -1.91	-4.1338 [32]
	H-fcc	-4.60 / -2.10	-4.3538 [32], -4.0837 [34]
	T-Pd	-3.11 / -0.61	-2.6438 [32]

Table 4.3: Calculated O adsorption energies (eV, reference to O(g)) on three surfaces and comparison with previous theoretical values. The most favorable sites are underlined.

Surface	Ea (Theo.) This work	ΔE (Theo.) This work	Ea (Expt.)	Ea (Theo.) [34]
Pd	0.88	-0.7	0.90	0.93
α-PdZn (1-Zn)			0.73	
A	0.75 (0.93)	-0.85 (-0.67)		
B	0.50 (0.81)	-1.05 (-0.74)		
C	0.83 (0.83)	-0.67 (-0.67)		
α-PdZn (2-Zn)				
A	0.34 (1.59)	-2.05 (-0.67)		
B	0.51 (0.78)	-1.06 (-0.79)		
C	0.74 (0.74)	-0.82 (-0.82)		
-PdZn	0.59	-0.9	0.78	

Table 4.4: Calculated activation energies (Ea) and reaction energies (ΔE) (eV) on three surfaces and comparison with experimental and previous theoretical values. Values in parentheses are normalized to most stable initial state.

β-PdZn.

The addition of another Zn atom in the alpha system causes further reduction in the barrier for the most stable of the three states studied. The C coadsorbed configuration, in which the CO is on the $T_{1,1}$ and O on $F_{1,0}$ sites, has a barrier of 0.74 and exothermicity of -0.82. The other two configurations (A with CO on $T_{1,0}$, O on $F_{0,2}$ and B with CO on $T_{2,1}$ and O on $H_{1,0}$) display low apparent barriers of 0.34 (A) and 0.51 (B) but large exothermicities of -2.05 and -1.06 respectively as a result of the very low binding energies of their coadsorbed initial states. As a result, the very small barrier of state A is misleading, and should be compared to the most stable state C. When all are normalized to C, the barriers are 1.59 (A), 0.78 (B) and 0.74 (C), respectively.

4.4 Discussion

Our calculations show that the addition of a single Zn atom on the Pd(111) surface reduces the reaction barrier for CO oxidation by almost 10%. This is consistent with the experimentally observed reduction of the activation energy from 86 kJ/mol (0.89 eV) on the Pd catalyst to 73 kJ/mol (0.77 eV) on α-PdZn. We emphasize here that our calculated α-PdZn model is an approximation of the catalyst because the precise surface composition is not known. Rodriguez [12], on the basis of the rate which Pd bound CO decreases with increasing Zn concentration, deduced that Zn tends to segregate to the surface. Our calculated results are indeed consistent with the enhanced reactivity we observe on the α samples.

However, this initial high activity state is not stable and the α-PdZn samples showed a significant drop in activity once exposed to CO oxidation conditions. To explain both the high initial activity and the subsequent deactivation we envision the following two-site kinetic picture. On the α samples we can expect that a large portion of the surface behaves similarly to the Pd metal but with islands of Zn-modified Pd sites as has been predicted theoretically [43]. These Zn-modified Pd sites, with destabilized CO binding but essentially unchanged O binding, remain available for O_2 dissociative adsorption, preventing CO poisoning and providing a continuous source of O. The surrounding Pd does strongly binds CO, providing a ready source of bound CO reactants. The reduced activation energy at these sites, together with this favorable kinetic situation, result in the initial enhanced activity. On β-PdZn, the activation energy is even lower than on α, but now Zn modifies all Pd. As a result, all sites are equal.

Unfortunately, this enhanced state is short lived, and quickly deactivates as can be seen in Fig. 4.1. We believe that this deactivation is a result of the oxidation of Zn to ZnO. Previous work [19, 40] has indicated that the PdZn surface is readily

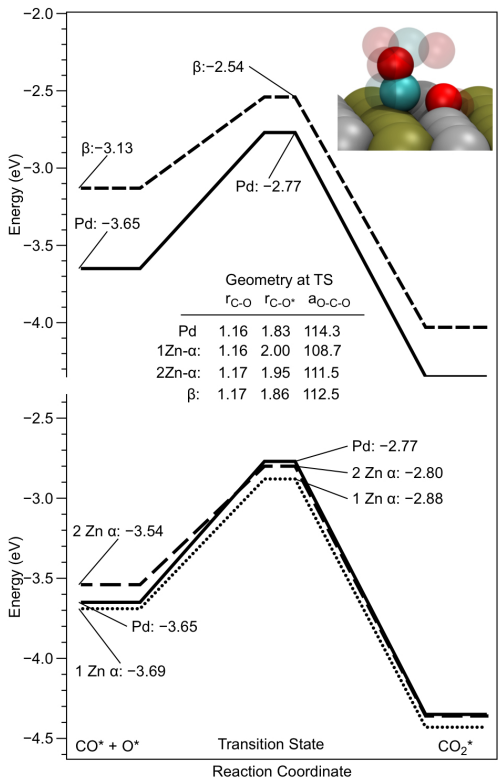

Figure 4.3: Reaction profile for all surfaces. Pd and β are compared in the top and Pd and α-PdZn in the bottom trace. Gas phase CO + O + clean surface is used as reference state. These plots highlight the competing effects of Zn; destabilization of the coadsorbed state and a reduction in the activation energy.

oxidized under CO oxidation reaction conditions, but this oxidation can be reversed during the reductive methanol steam reforming process, which produces hydrogen. The oxidation of Zn modifies the interaction with Pd, and the beneficial effects of Zn are likely lost. Nonetheless, even at steady state the α-PdZn is about two times more reactive than Pd metal, which suggests that some of the beneficial effects of Zn are retained. Indeed, the activation energy of α-PdZn in the steady state is slightly different from that of Pd, as shown in Fig. 4.1.

Given the much lower theoretical barrier for CO oxidation on the β-PdZn(111)

intermetallic surface, one would expect that this catalyst would show the highest reactivity. However, even in the initial transient stage, this catalyst is less active than α-PdZn. The CO oxidation reactivity is determined by the coverage of CO and the barrier for CO oxidation. We found that the coverage of CO on the β-PdZn surface is very low, as also seen in previous work [9, 12, 40]. Rodriguez analyzed this phenomenon [12] and reasoned that the presence of Zn, which binds CO poorly, effectively reduces the number of available Pd sites to bind CO, thereby reducing to total amount of CO these particles are able to adsorb. This would then explain the lower overall reactivity of the β-PdZn catalyst. Like the α-PdZn samples, however, we also see a decline in activity of this catalyst during the initial 60 minutes of CO oxidation. We believe that the same mechanism discussed above on the α phase catalysis is in operation here as well, namely, the surface Zn is oxidized during the catalysis, which diminishes the promotional effects of Zn. It is interesting to note that the CO binding energy on PdZn (-0.78 eV) is significantly smaller than that on Pd (-1.55 eV). Hence, as the Zn is oxidized and Pd sites are liberated, CO would clearly prefer to adsorb on Pd if both surfaces are available, due to the higher binding energy on Pd. Thus, the effective barrier for CO oxidation would closely resemble that on Pd, which was indeed what was observed. This is illustrated in Fig. 4.3, which summarized the reaction profiles for all surfaces. Indeed, the experimentally measured steady state activation energy on the β-PdZn catalyst is slightly lower than that on metallic Pd, suggesting coexistence of Pd and PdZn sites.

4.5 Conclusions

In this Chapter, we examined the effects of Zn in PdZn alloys on CO binding and reactivity for its oxidation. On the experimental side, phase pure samples of Pd metal, α-PdZn and β-PdZn have been synthesized. Specific reactivities for CO oxidation

were measured both in the initial state (after exposure to CO oxidation reaction conditions) and at steady state. It was found that the initial CO oxidation reactivity (per Pd surface atom) could be 10 times higher on the α-PdZn surface and about 5 times higher on the β-PdZn surface, compared to metallic Pd. This was attributed to higher reactivity to a weakening of the CO bond and easier binding of oxygen to Pd sites modified by Zn. However, the high initial activity is lost during CO oxidation presumably due to the fact that the Zn becomes oxidized and is no longer available. At steady state, the reactivity of the β-PdZn surfaces approaches that of Pd metal. The α-PdZn surface remains slightly more active than Pd metal, even at steady state.

To understand these experimental findings, we have calculated the most stable adsorption sites for CO and O as well as the barriers for CO oxidation on Pd(111), α-PdZn where Zn is present a low concentrations on the Pd(111) surface, and β-PdZn which is an ordered intermetallic compound. The calculated binding energies suggest that Zn weakens the binding of CO to Pd and also lowers the barrier for reaction on the Zn modified surfaces. The energetics of all reactions on coexisting Pd and Zn sites under experimental conditions allows us to identify the preferred reaction site and mechanism, which are consistent with experimental observations.

The work reported here suggests that modification of the reactivity of Pd by added oxophilic metals such as Zn is consistent with the predictions of theory, but in order to achieve stable high steady state activities it is important to prevent the oxidation of the oxophilic component.

References

[1] H.-J. Freund, G. Meijer, M. Scheffler, R. Schlögl, and M. Wolf, "CO Oxidation as a Prototypical Reaction for Heterogeneous Processes," *Angewandte Chemie*

International Edition, vol. 50, pp. 10064–10094, Sept. 2011.

[2] O. Balmes, A. Resta, D. Wermeille, R. Felici, M. E. Messing, K. Deppert, Z. Liu, M. E. Grass, H. Bluhm, R. v. Rijn, J. W. M. Frenken, R. Westerström, S. Blomberg, J. Gustafson, J. N. Andersen, and E. Lundgren, "Reversible formation of a PdCx phase in Pd nanoparticles upon CO and O2 exposure," *Physical Chemistry Chemical Physics*, vol. 14, no. 14, p. 4796, 2012.

[3] M. S. Chen, Y. Cai, Z. Yan, K. K. Gath, S. Axnanda, and D. W. Goodman, "Highly active surfaces for CO oxidation on Rh, Pd, and Pt," *Surface Science*, vol. 601, pp. 5326–5331, Dec. 2007.

[4] F. Gao, Y. Wang, Y. Cai, and D. W. Goodman, "CO oxidation on Pt-group metals from ultrahigh vacuum to near atmospheric pressures. 2. Palladium and platinum," *The Journal of Physical Chemistry C*, vol. 113, no. 1, pp. 174–181, 2008.

[5] J. Gustafson, R. Westerström, O. Balmes, A. Resta, R. van Rijn, X. Torrelles, C. T. Herbschleb, J. W. M. Frenken, and E. Lundgren, "Catalytic Activity of the Rh Surface Oxide: CO Oxidation over Rh(111) under Realistic Conditions," *The Journal of Physical Chemistry C*, vol. 114, pp. 4580–4583, Mar. 2010.

[6] B. L. M. Hendriksen, M. D. Ackermann, R. van Rijn, D. Stoltz, I. Popa, O. Balmes, A. Resta, D. Wermeille, R. Felici, S. Ferrer, and J. W. M. Frenken, "The role of steps in surface catalysis and reaction oscillations," *Nature Chemistry*, vol. 2, pp. 730–734, July 2010.

[7] L. Carrette, K. A. Friedrich, and U. Stimming, "Fuel cells–fundamentals and applications," *Fuel cells*, vol. 1, no. 1, pp. 5–39, 2001.

[8] T. Engel and G. Ertl, "Elementary steps in the catalytic oxidation of carbon monoxide on platinum metals," *Advances in Catalysis*, vol. 28, pp. 1–78, 1979.

[9] E. Jeroro, V. Lebarbier, A. Datye, Y. Wang, and J. M. Vohs, "Interaction of CO with surface PdZn alloys," *Surface Science*, vol. 601, no. 23, pp. 5546–5554, 2007.

[10] E. Jeroro and J. M. Vohs, "Zn modification of the reactivity of Pd(111) toward methanol and formaldehyde," *Journal of the American Chemical Society*, vol. 130, no. 31, pp. 10199–10207, 2008.

[11] E. Jeroro and J. M. Vohs, "Exploring the Role of Zn in PdZn Reforming Catalysts: Adsorption and Reaction of Ethanol and Acetaldehyde on Two-dimensional PdZn Alloys," *The Journal of Physical Chemistry C*, vol. 113, pp. 1486–1494, Jan. 2009.

[12] J. A. Rodriguez, "Interactions in bimetallic bonding: electronic and chemical properties of PdZn surfaces," *J. Phys. Chem*, vol. 98, no. 22, pp. 5758–5764, 1994.

[13] H. Gabasch, A. Knop-Gericke, R. Schlögl, S. Penner, B. Jenewein, K. Hayek, and B. Klötzer, "Zn Adsorption on Pd(111): ZnO and PdZn Alloy Formation," *The Journal of Physical Chemistry B*, vol. 110, pp. 11391–11398, June 2006.

[14] C. Rameshan, W. Stadlmayr, C. Weilach, S. Penner, H. Lorenz, M. Hävecker, R. Blume, T. Rocha, D. Teschner, A. Knop-Gericke, R. Schlögl, N. Memmel, D. Zemlyanov, G. Rupprechter, and B. Klötzer, "Subsurface-Controlled CO_2 Selectivity of PdZn Near-Surface Alloys in H_2Generation by Methanol Steam Reforming," *Angewandte Chemie International Edition*, vol. 49, pp. 3224–3227, Apr. 2010.

[15] W. Stadlmayr, C. Rameshan, C. Weilach, H. Lorenz, M. Havecker, R. Blume, T. Rocha, D. Teschner, A. Knop-Gericke, D. Zemlyanov, S. Penner, R. Schlögl, G. Rupprechter, B. Klötzer, and N. Memmel, "Temperature-Induced Modifications of PdZn Layers on Pd(111)," *The Journal of Physical Chemistry C*, vol. 114, pp. 10850–10856, June 2010.

[16] K. M. Neyman, K. H. Lim, Z.-X. Chen, L. V. Moskaleva, A. Bayer, R. Denecke, and N. R Sch, "Microscopic models of PdZn alloy catalysts: structure and reactivity in methanol decomposition," *Physical Chemistry Chemical Physics*, vol. 9, no. 27, p. 3470, 2007.

[17] R. A. Dagle, Y.-H. Chin, and Y. Wang, "The Effects of PdZn Crystallite Size on Methanol Steam Reforming," *Topics in Catalysis*, vol. 46, pp. 358–362, Nov. 2007.

[18] V. Lebarbier, R. Dagle, A. Datye, and Y. Wang, "The effect of PdZn particle size on reverse-water-gas-shift reaction," *Applied Catalysis A: General*, vol. 379, pp. 3–6, May 2010.

[19] B. Halevi, E. J. Peterson, A. DeLaRiva, E. Jeroro, V. M. Lebarbier, Y. Wang, J. M. Vohs, B. Kiefer, E. Kunkes, M. Hävecker, M. Behrens, R. Sehloegl, and A. K. Datye, "Aerosol-Derived Bimetallic Alloy Powders: Bridging the Gap," *The Journal of Physical Chemistry C*, vol. 114, no. 40, pp. 17181–17190, 2010.

[20] E. J. Peterson, B. Halevi, B. Kiefer, M. N. Spilde, A. K. Datye, J. Peterson, L. Daemen, A. Llobet, and H. Nakotte, "Aerosol synthesis and Rietveld analysis of tetragonal (β 1) PdZn," *Journal of Alloys and Compounds*, vol. 509, no. 5, pp. 1463–1470, 2011.

[21] J. P. Perdew, J. A. Chevary, S. H. Vosko, K. A. Jackson, M. R. Pederson, D. J. Singh, and C. Fiolhais, "Atoms, molecules, solids, and surfaces: Applications of the generalized gradient approximation for exchange and correlation.," *Physical review B, Condensed matter*, vol. 46, pp. 6671–6687, Sept. 1992.

[22] G. Kresse and J. Hafner, "Abinitio Molecular-Dynamics for Liquid-Metals," *Physical Review B*, vol. 47, no. 1, pp. 558–561, 1993.

[23] G. Kresse and J. Furthmüller, "Efficient iterative schemes for ab initio total-energy calculations using a plane-wave basis set," *Physical Review B*, vol. 54, pp. 11169–11186, Oct. 1996.

[24] G. Kresse and J. Furthmüller, "Efficiency of ab-initio total energy calculations for metals and semiconductors using a plane-wave basis set," *Computational Materials Science*, vol. 6, pp. 15–50, July 1996.

[25] P. Blöchl, "Projector augmented-wave method.," *Physical review B, Condensed matter*, vol. 50, pp. 17953–17979, Dec. 1994.

[26] G. Kresse and D. Joubert, "From ultrasoft pseudopotentials to the projector augmented-wave method," *Physical Review B*, vol. 59, no. 3, p. 1758, 1999.

[27] M. Methfessel and A. Paxton, "High-precision sampling for Brillouin-zone integration in metals.," *Physical review B, Condensed matter*, vol. 40, pp. 3616–3621, Aug. 1989.

[28] H. J. Monkhorst and J. D. Pack, "Special points for Brillouin-zone integrations," *Physical review B, Condensed matter*, vol. 13, no. 12, pp. 5188–5192, 1976.

[29] F. Abild-Pedersen and M. P. Andersson, "CO adsorption energies on metals with correction for high coordination adsorption sites–A density functional study," *Surface Science*, vol. 601, no. 7, pp. 1747–1753, 2007.

[30] H. Jonsson, G. Mills, and K. W. Jacobsen, "Nudged elastic band method for finding minimum energy paths of transitions," in *Classical and Quantum Dynamics in Condensed Phase Simulations* (B. J. Berne, G. Ciccotti, and D. F. Coker, eds.), Singapore: World Scientific, 1998.

[31] G. Henkelman, B. P. Uberuaga, and H. Jonsson, "A climbing image nudged elastic band method for finding saddle points and minimum energy paths," *The Journal of Chemical Physics*, vol. 113, no. 22, pp. 9901–9904, 2000.

[32] Z.-X. Chen, K. M. Neyman, K. H. Lim, and N. Rösch, "CH3O decomposition on PdZn(111), Pd(111), and Cu(111). A theoretical study.," *Langmuir*, vol. 20, pp. 8068–8077, Sept. 2004.

[33] H. Conrad, G. Ertl, J. Koch, and E. E. Latta, "Adsorption of CO on Pd single crystal surfaces," *Surface Science*, vol. 43, no. 2, pp. 462–480, 1974.

[34] B. Hammer, L. B. Hansen, and J. K. Nørskov, "Improved adsorption energetics within density-functional theory using revised Perdew-Burke-Ernzerhof functionals," *Physical Review B*, vol. 59, no. 11, p. 7413, 1999.

[35] Z.-X. Chen, K. H. Lim, K. M. Neyman, and N. Rösch, "Density functional study of methoxide decomposition on PdZn (100)," *Physical Chemistry Chemical Physics*, vol. 6, no. 18, pp. 4499–4504, 2004.

[36] P. Sautet, M. K. Rose, J. C. Dunphy, S. Behler, and M. Salmeron, "Adsorption and energetics of isolated CO molecules on Pd (111)," *Surface Science*, vol. 453, no. 1, pp. 25–31, 2000.

[37] T. Mitsui, M. Rose, E. Fomin, D. Ogletree, and M. Salmeron, "Diffusion and Pair Interactions of CO Molecules on Pd(111)," *Physical Review Letters*, vol. 94, p. 036101, Jan. 2005.

[38] S. Surnev, M. Sock, M. G. Ramsey, F. P. Netzer, M. Wiklund, M. Borg, and J. N. Andersen, "CO adsorption on Pd (111): a high-resolution core level photoemission and electron energy loss spectroscopy study," *Surface Science*, vol. 470, no. 1, pp. 171–185, 2000.

[39] J. A. Herron, S. Tonelli, and M. Mavrikakis, "Atomic and molecular adsorption on Pd(111)," *Surface Science*, vol. 606, pp. 1670–1679, Nov. 2012.

[40] B. Halevi, E. J. Peterson, A. Roy, A. DeLaRiva, E. Jeroro, F. Gao, Y. Wang, J. M. Vohs, B. Kiefer, and E. Kunkes, "Catalytic reactivity of face centered cubic PdZn α for the steam reforming of methanol," *Journal of Catalysis*, vol. 291, pp. 44–54, 2012.

[41] J. L. Falconer and J. A. Schwarz, "Temperature-Programmed Desorption and Reaction: Applications to Supported Catalysts," *Catalysis Reviews*, vol. 25, pp. 141–227, June 1983.

[42] C. J. Zhang and P. Hu, "CO oxidation on Pd(100) and Pd(111): a comparative study of reaction pathways and reactivity at low and medium coverages.," *Journal of the American Chemical Society*, vol. 123, pp. 1166–1172, Feb. 2001.

[43] X. He, Y. Huang, and Z.-X. Chen, "Zinc coverage dependent structure of PdZn surface alloy.," *Physical Chemistry Chemical Physics*, vol. 13, pp. 107–109, Jan. 2011.

Chapter 5

CH_2O Selectivity in Methanol Steam Reforming

5.1 Introduction

Using methanol as a hydrogen carrier to be reformed upstream from fuel-cells is an exciting prospect for a next generation transportation strategy [1]. It takes advantage of the high efficiency of polymer-electrolyte hydrogen fuel cells and the fact that their only exhaust is H_2O. It also circumvents the inherent difficulties in dispensing, storing and transporting hydrogen. However, using an methanol reformer upstream of a fuel cell places strong demands on the selectivity of the catalyst; fuel cells are rapidly poisoned by CO, a possible side product in reforming. It is thus critical that the catalyst is optimized to produce exclusively CO_2 to avoid the added complexity of scrubbing the hydrogen stream of CO.

Methanol steam reforming,

$$CH_3OH + H_2O \longrightarrow CO_2 + 3\,H_2 \tag{5.1}$$

and methanol decomposition,

$$CH_3OH \longrightarrow CO + 2\,H_2 \tag{5.2}$$

are closely related reactions, and both can be catalyzed by transition metal surfaces. However, even under reforming conditions, Pd will exclusively decompose methanol to CO and hydrogen gas.

As was illuminated by the study of MSR on copper in Chapter 3, and as noted by previous theoretical studies [2, 3], the selectivity of MSR catalysts is governed by the fate of the adsorbed formaldehyde (CH_2O^*) intermediate. It can either decompose to form formyl (CHO) and adsorbed hydrogen (H^*), which then will quickly and irreversibly dehydrogenate further to produce $CO^* + H_2^*$. Or, it can condense with an adsorbed hydroxyl (OH^*) or oxygen (O^*) species to form hydroxymethoxy/dioxymethalene (OCH_2OH/OCH_2O) respectively. These, via a series of low barrier dehydroxylation steps, eventually produce CO_2 and hydrogen gas, the

required products of MSR. On a Pd surface, the decomposition reaction is favored over MSR, resulting in the evolution of $CO + H_2$ exclusively. Yet, on Cu and PdZn surfaces, MSR is the favored reaction, with little or no CO production. Understanding the electronic and molecular factors that influence the fate of formaldehyde on these three surfaces provide powerful tools for future development of MSR catalysts. Dehydrogenation of formaldehyde has been previously modeled on Cu, Pd and PdZn surfaces [3] showing a low reaction barrier on Pd surfaces but Cu and PdZn showed activation energies greater than the binding energy of CH_2O. Later it was calculated [2] that not only is the decomposition pathway blocked on copper but additionally the condensation reaction is activated with respect to Pd. There are no studies which address both reaction on these three import surfaces.

In this Chapter a detailed analysis of the adsorption of CH_2O on the (111) surfaces on Pd, Cu, and the 50:50 β-PdZn alloy are presented, as well as the stationary points for the decomposition ($CH_2O^* \longrightarrow CHO^* + H^*$) and condensation ($CH_2O^* + OH^* \longrightarrow OCH_2OH^{**}$) reactions of formaldehyde are presented. Density of states (DOS) are calculated for adsorbed formaldehyde and are consistent in explaining trends in binding energies within the framework of the d-band model [4, 5]. Only the reaction with CH_2O^* and OH^* are considered as concentrations of O^* are expected to be low under reforming conditions and reactions with O^* tend to be similar to OH^* but with lower barriers [6]. It is found that on both Cu and PdZn the condensation reaction is quite exothermic with low reaction barriers. Additionally, the decomposition pathway is disfavored, both thermodynamically and kinetically. This behavior is reversed for Pd, as might be expected give the various selectivities of these three metals.

5.2 Methods

Planewave density functional calculations were performed with the VASP code under the PW91 functional. Planewave expansion was truncated at 400 eV and the core electrons are treated with PAW type pseudopotentials. Integrations over the Brillouin zone where performed using a 5x5x1 kpoint grid constructed by the method of Monkhorst-Pack. The three surfaces studied (Cu(111), Pd(111) and PdZn(111)) where each was constructed from bulk structures with DFT minimized lattice parameters. Our calculated lattice parameters are reported previously [6, 7], and agree well with other calculations.

Cu(111) and Pd(111) were modeled with 2x2x3 super cells, and PdZn(111) was modeled with a slightly larger 4x4x3 slab because the equivalent sized slab could not be constructed with the desired 1:1 stoichiometry and a 2x2x1 slab was found to be too small due to interactions with adjacent images. The top most layer of each clean slab was allowed to relax fully before being fixed for all subsequent calculations. This common approximation has been found to have only a minor (< 0.1 eV) effect on binding energies. The ionic positions in minimizations and reaction path calculations are all optimized until forces are less that 0.05 eV/Å. Binding energies are calculated by $E_{complex} - E_{slab} + E_{gas}$, where subscripts indicate the adsorbed system, the clean slab, and the gas phase adsorbate respectively. As such, a negative value indicates favorable binding. Reaction pathways were followed with the climbing image nudged elastic band method [8]. Density of states (DOS) are calculated and projected upon atomically centered spherical harmonics, allowing the resolution of d, s and p orbitals. Since DOS calculations are more sensitive to the size of kpoint grid than are geometry optimizations, the 7x7x1 Monkhorst-Pack grid was used for single point electronic calculations on the various structures determined at 5x5x1.

5.3 Results

5.3.1 Adsorption of CH_2O

Formaldehyde exhibits both a weakly bound physisorbed and more tightly bound chemisorbed state. The binding energies and geometries are presented in Table 5.1. The geometry of CH_2O remains similar to its gas phase counterpart in the physisorbed state, which is characterized by binding energies on the order of 0.1 eV and shows no site preference on the surface. Physisorption is very weak interaction; there is very little coupling between the molecular orbitals and the surface d-band. This can be observed in the sp-band DOS of physisorbed CH_2O in Figure 5.1, where the molecular orbitals have only been broadened and shifted down in energy, consistent with interaction only with the delocalized s-band of the surface. The molecular geometry of CH_2O is only slightly perturbed from that in gas phase.

The chemisorbed state, however, is bent towards a trigonal-pyramidal geometry with the hydrogen atoms projecting up from the surface and O atom down on all surfaces, but most so on Pd. The oxygen atom prefers binding at a bridge site and carbon on an adjacent top site such that the CH_2O straddles a hollow site. This top-bridge configuration is unique on Pd and Cu, but on PdZn the carbon atom prefers the top site on a Pd atom and oxygen at a two zinc atom bridge site. This is typical of the PdZn surface, where it is observed that carbon and hydrogen atoms tend to favor coordination with Pd oxygen prefers to maximize its interactions with Zn. It should be noted that both top-top [3, 9] and top-bridge [2, 6] configurations have been reported as the most stable configuration on all three these surfaces. All reported binding energies are consistent with each other within experimental error, and this reflects the fact that the shallow binding potential of CH_2O to the surface does not show a strong binding site preference.

Surface	BE (eV)	O-Surf (Å)	C-Surf (Å)	C−O (Å)	C−H (Å)
Pd(111)	-0.10, (-0.66)	1.75, (3.04)	1.97, (3.03)	1.33, (1.22)	1.10, (1.12)
Cu(111)	-0.06, (-0.06)	1.68, (3.35)	2.04, (3.22)	1.33, (1.22)	1.10, (1.12)
PdZn(111)	-0.06, (-0.15)	1.81, (2.80)	1.97, (3.12)	1.32, (1.22)	1.10, (1.11)
CH_2O(g)				1.21	1.12

Table 5.1: Binding energy and geometric parameters of chem- and physisorbed CH_2O on Cu, Pd and PdZn surfaces. Chemisorbed values are in parenthesis. Also included are gas phase CH_2O bond lengths for comparison

CH_2O Adsorption DOS

According to the d-band model, molecular adsorption is a result of coupling between molecular orbitals and the metal's d and s-bands. Coupling with the broad s-band results in a down shift and broadening of the molecular orbitals and this interaction does not change from metal to metal. The d-band however, is discrete enough that interaction with molecular orbitals results in a splitting into broadened bands or bonding and anti-bonding molecule-surface orbitals. The degree of the splitting will depend on the energy difference between the d-band center and the s-band down-shifted MO energy, and the degree of coupling between the d-band and MO.

Upon weak physisorption, both the HOMO and LUMO of CH_2O shifted down in energy by about 1.5 eV. The HOMO, which is anti-bonding in the C=O and bonding in C−H is not significantly modified in shape from the gas phase, indicating a weak coupling with the surface states. The LUMO is modified more: it is broadened but there is not significant splitting into distinct bonding/anti-bonding states. Between the different surfaces, we again see a manifestation of the similarity of Cu with PdZn and in contrast to Pd. Neither HOMO or LUMO are shifted as far down in Pd as Cu and PdZn, consistent with the higher d-band center in Pd.

Chemisorption causes a significant distortion in the molecular orbitals, which

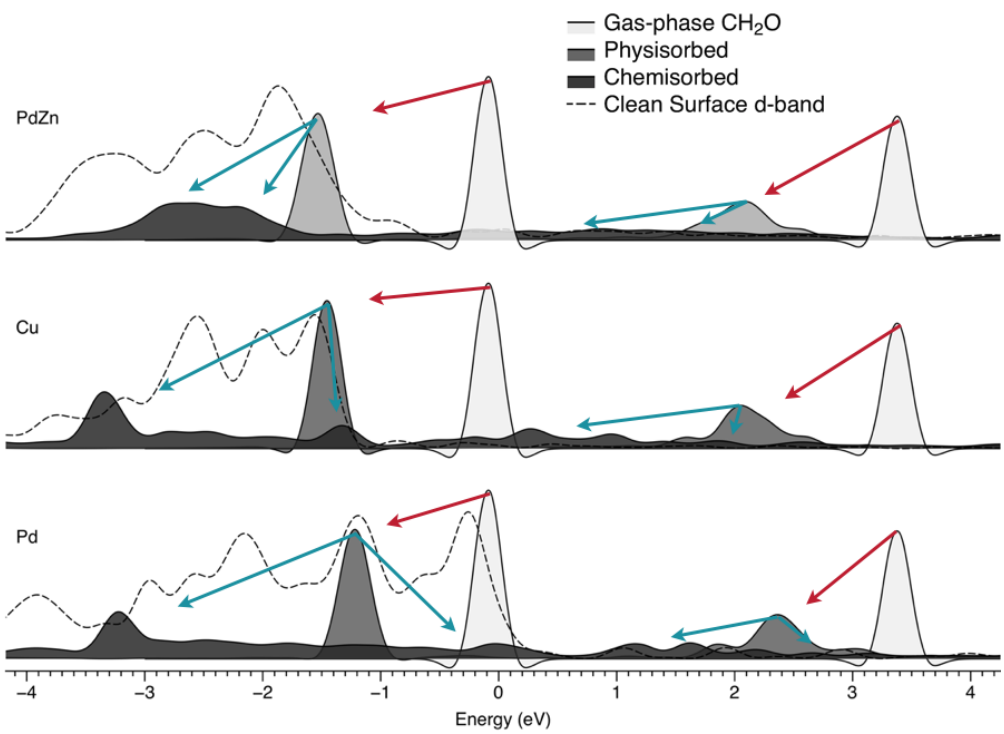

Figure 5.1: Total s+p projected DOS of CH_2O in gas phase, at its physisorbed geometry and upon full chemisorption on the (111) surfaces of PdZn, Cu and Pd. The clean surface d-band is also plotted as unshaded dashed line. Differences in adsorption energies can be interpreted as the different occupation of anti-bonding orbitals produced first upon weak coupling (red line) and then upon full coupling with the d-band (blue lines).

might be surprising given the relatively small binding energy of formaldehyde to these surfaces. The small binding energy might be incorrectly interpreted as indication of a weak interaction with the surface, but as evidenced from the DOS, adsorbed formaldehyde is very different (electronically) from gas phase formaldehyde. Low binding energies, particularly on Cu and PdZn, arise because both bonding and anti-bonding adsorbate-surface orbitals fall below the Fermi level, and thus contribute no net bonding. The higher d-band center of Pd, however, pushes some small population of anti-bonding orbitals above the Fermi level, depopulating these most energetically

unfavorable and therefore most anti-bonding states. The result is slightly more occupied bonding orbitals than anti-bonding on Pd surface, and stronger binding.

5.3.2 Reactions

5.3.3 $CH_2O^* \longrightarrow CHO^* + H^*$

The dehydrogenation reaction is similar on all three metals. Starting from the chemisorbed geometry as the IS, the plane of CH_2O tilts to position the dissociating hydrogen towards the nearest adjacent 3-fold hollow site in the transition state. The C-H bond breaks, and the CHO moiety moves to its preferred off-hollow binding site in the final state, in which carbon points down and the O and H atoms up, and the H^* atom is fully in its hollow site. On PdZn, the most stable FS corresponds to that where both CHO^* and H^* are in the preferred Pd_2Zn hollow site. These reactions are illustrated in Figure 5.2. On Cu and PdZn, CHO prefers a more a-top interaction with Cu and Pd respectively, and is pulled slightly out of the hollow site. On Pd, the C atom is bridging two Pd atoms, and its O is a-top another. The binding energy of this Pd FS is also the strongest of the three metals [3].

The reaction is favored on the Pd surface both with the lowest relative transition state (0.5 eV) and because it is significantly exothermic (-0.6 eV). PdZn and Cu both have barriers 0.3 eV greater and are endothermic by 0.5 and 0.4 eV respectively. These barriers are far larger than the binding energy of CH_2O and as such would be expected to desorb or defuse away rather than decompose. The barrier on Pd(111) is also high, however it is compensated by the strong binging energy to this surface. As a result, once CH_2O is formed, decomposition is a competitive pathway to desorption. These results for the decomposition of CH_2O are consistent with previously published results within the variation of functionals and surface models used.

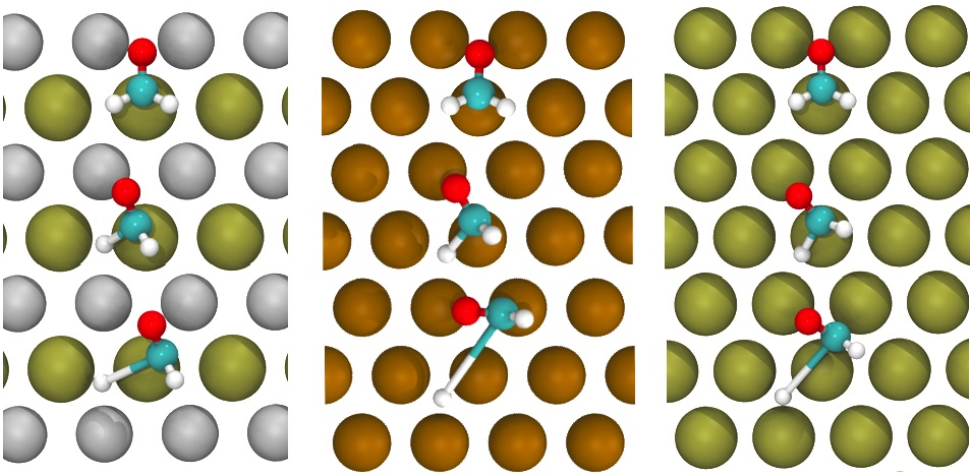

Figure 5.2: Initial, transition and final states (top, middle and bottom respectively) for $CH_2O^* \longrightarrow CHO^* + H^*$ on PdZn (left) , Cu (center) and Pd (right) slabs.

5.3.4 $CH_2O^* + OH^* \longrightarrow OCH_2OH^{**}$

The condensation reaction is also similar on the three surfaces studied, however slight variation in the initial coadsorbed state and transition state geometries are

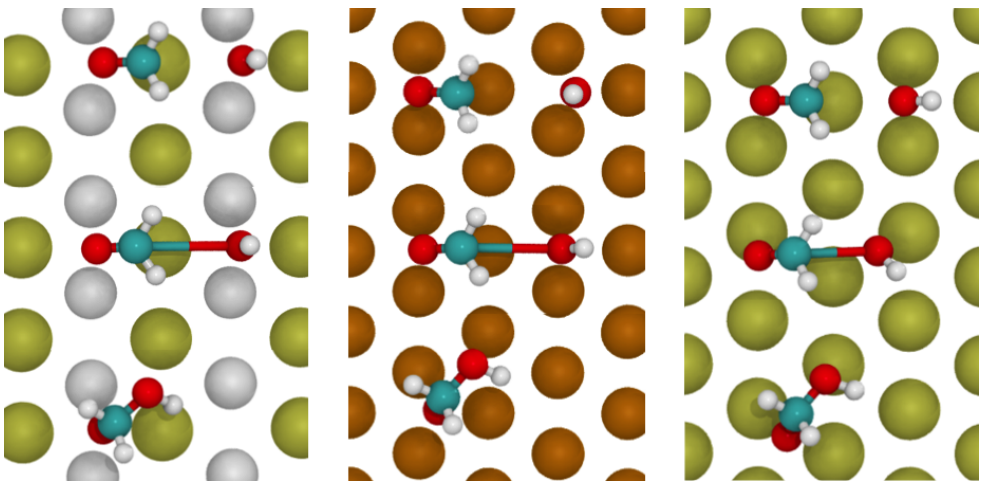

Figure 5.3: Geometry of Initial, transition and final states (top, middle and bottom respectively) for $CH_2O^* + OH^* \longrightarrow OCH_2OH^{**}$ on PdZn (left) , Cu (center) and Pd (right) slabs.

	CH_2O				OH		
Surface	O−M	C−M	C−O	C−H	O-M	O−H	$C_{CH2O}-O_{OH}$
Pd(111)	2.26, 2.29	2.12	1.33	1.10, 1.10	2.16, 2.16	0.98	3.14
Cu(111)	2.15, 2.15	2.13	1.33	1.10, 1.10	2.06, 2.06, 2.03	0.97	3.78
PdZn(111)	2.39 (Zn), 2.39 (Zn)	2.31 (Pd)	1.29	1.10, 1.10	2.10 (Zn), 2.10 (Zn)	0.98	3.22

Table 5.2: Geometric parameters of coadsorbed $CH_2O^* + OH^*$ on (111) surfaces of Pd, Cu and PdZn in Å.

Reaction	Surface	$E^‡$ (Lit. Refs)	ΔE
$CH_2O^* \longrightarrow CHO^* + H^*$	Pd(111)	0.53 (0.36 [2], 0.39 [3], 0.53 [10])	-0.58 (-0.84 [2], -0.58 [3], 0.75 [10])
	Cu(111)	0.80 (0.76 [2], 0.66 [6], 0.83 [3])	0.37 (0.24 [2], 0.56 [11], 0.37 [3])
	PdZn(111)	0.76 (0.83 [12], 0.81 [3])	0.49 (-0.19 [12], -0.04 [3])
$CH_2O^* + OH^* \longrightarrow OCH_2OH^{**}$	Pd(111)	0.45 (0.58 [2])	-0.32 (-0.18 [2])
	Cu(111)	0.11(0.18 [2], 0.11 [6])	-0.73 (-0.42 [2], -0.46 [6])
	PdZn(111)	0.02 (0.16 [13])	-0.65 (-0.34 [13])

Table 5.3: Transition state and reaction energies of $CH_2O^* \longrightarrow CHO^* + H^*$ and $CH_2O^* + OH^* \longrightarrow OCH_2OH^{**}$ on Cu(111), Pd(111) and PdZn(111) in eV

collected in Tables **??** and 5.2. All initial states where constructed to be the most stable configurations in which OH^* is positioned to attack the C atom from the nearest stable 3-fold hollow site. The final states where constructed such that the OCH_2OH^{**} is bound to the hollow site that CH_2O initially straddled in it's top-bridge configuration. The IS and FS structures as well as TS structures are illustrated in Figure 5.3. Again, efforts were made to locate the binding configurations which maximize Pd interaction with C and H atoms, and Zn with O, which maximize the binding energies of adsorbates to the surface.

On copper, the reaction passes through an early transition state in which carbon atom lifts slightly as it moves to atop position, and the O of CH_2O remains in the hollow. OH moves into the bridge site, changing the C−OH bond from 3.78Å in the IS to 3.30 at the TS. The reaction continues as carbon further rises, OH reorients to lay parallel to the surface and the C−OH distance shortens to 1.42Å in the FS. On PdZn, the TS is also very early, and marked by a lifting of formaldehyde from the

	CH_2O				OH		
Surface	O−M	C−M	C−O	C−H	O−M	O−H	$C_{CH2O}-O_{OH}$
Pd(111)	2.23, 3.05	2.92, 2.91	1.25	1.11, 1.10	2.38, 2.07	0.98	2.85
Cu(111)	2.40, 2.40	2.43	1.27	1.11, 1.10	2.02, 2.02	0.98	3.30
PdZn(111)	3.28, 3.57	3.75	1.22	1.12, 1.12	2.05 (Zn), 2.06(Zn), 2.5 (Pd)	0.98	3.73

Table 5.4: Geometries of $CH_2O^* + OH^* \longrightarrow OCH_2OH^{**}$ transition state on Pd(111), Cu(111), and PdZn(111) in Å

surface as in Cu. On Pd, however, the TS is later ($C_{CH2O}-O_{OH}$ bond length $= 2.85$Å), and formaldehyde remains more tightly bound to the surface than Cu or PdZn. In fact, rather than move on top of the Pd atom, CH_2O shifts to a bridge site, tilting slightly as the O of CH_2O moves to bridge also, allowing a more side-on attach than on Cu and PdZn. The non ZPE-corrected barriers reaction energies are summarized in Table 5.3 and Figure 5.4. These results overestimate the exothermicity compared to previous results but are consistent with their trends. These differences are likely due to the lack of ZPE corrections in this work.

The reaction energies and barriers for condensation follow the opposite trend as those for the dehydrogenation reaction. The reactions are exothermic for all three surfaces, but more so for Cu and PdZn by ~ 0.4eV. The transition state energy is significantly higher for Pd however. The non-ZPE corrected values presented here are consistently lower than the ZPE corrected values in previous work. However, the trend is; depending on the surface in question, which differ primarily in their d-band electronic structure, both the point at which decomposition becomes unfavorable and when condensation becomes favorable happens in between that of palladium and copper and their isoelectric analogs.

5.4 Discussion

The various reactions studied here are summarized in Figure 5.4. We can see the similarity between Cu and PdZn, and the source of the favored product on all three surfaces. The similar reactivity between the copper and PdZn surfaces s. The 50:50 alloy between Pd and Zn is isoelectric with Copper (Zn carries one more electron than Cu and Pd one electron less), and further the band structures are very similar as can be see in the d-band plots of the clean surfaces found in Figure 5.1. Pd's d-band ends just at the Fermi level, with a small amount tailing above, in contrast to PdZn and Cu, which both terminate about 1 eV below the Fermi level. The high d-band center on Pd is responsible for the tighter binding energy, as the surface-CH_2O anti-bonding orbitals are less occupied than those for Cu/PdZn.

The tight binding of formaldehyde to the the Pd(111) surface is responsible for the exclusive selectivity of this surface towards CO; the reaction barrier to decomposition is lower that for desorption. This situation is not true on the Cu and PdZn surfaces, where very weak binding energies far outcompete the barrier to decomposition. This relative barrier heights for decomposition on the three surfaces can be rationalized with the BEP relationship. Stabilization of the IS on Pd will shift the CH_2O vibrational well down in energy, and in turn the crossing point between the IS well and the FS well is reduced as well.

In the condensation reaction, the reactivity trends are reversed. Here the barrier on Pd becomes competitive with the adsorption energy, and desorption becomes more likely. Likewise, barriers on Cu/PdZn surfaces are low enough that they become as likely as desorption. The fact that CH_2O does have such a low binding energy on these surfaces, even compared to the very low barriers to react with adsorbed OH, is consistent with the observation of small traces of CH_2O in MSR products on these two catalysts. Again, these reactions follow the BEP relationship but it is not due to

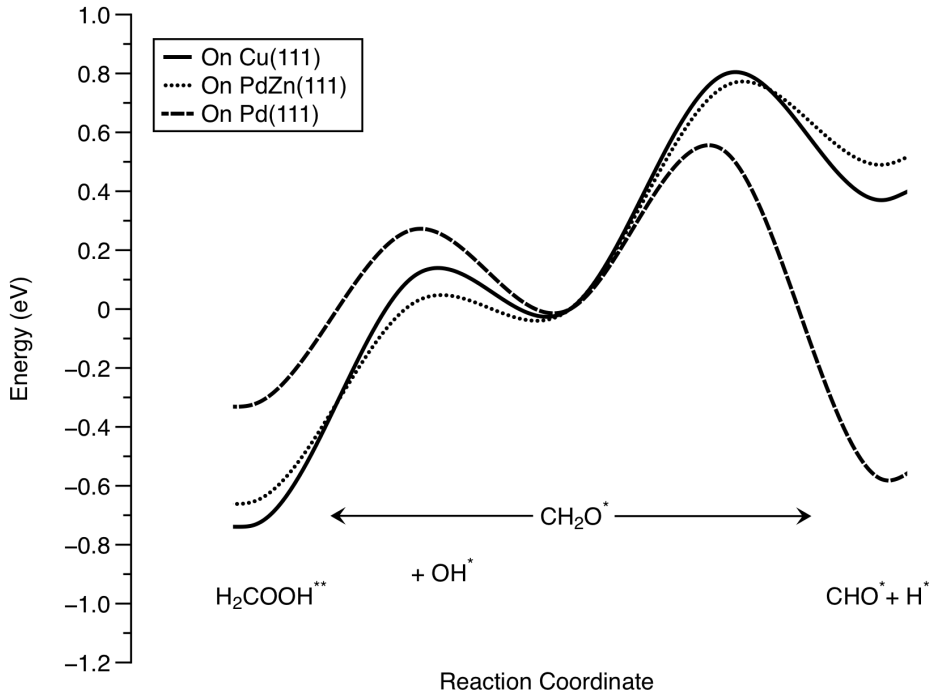

Figure 5.4: Summary of the reaction energies for condensation and dehydrogenation of formaldehyde on the three surfaces studied here.

the stabilization of the reactants as it is in decomposition, as this would lead to the expectation that the barrier on Pd would be the lowest. Rather, it is stabilization of the product on Cu and PdZn over that on Pd, a result of the difference in OCH_2OH^{**} adsorption energies [2, 6, 13].

Two possible reactions of formaldehyde have been investigated on three important catalytic surfaces; dehydrogenation and condensation with OH. There is evidence that the overall selectivity of an MSR catalyst is dependent upon the relative rates of these two reactions. It is found that on the low d-band center surfaces Cu and PdZn, condensation is favored and on the high d-band Pd surface, dehydrogenation is preferred. This suggests a region of d-band energies which can influence the selectivity of this key methanol reforming intermediate. Furthermore, it appears

that PdZn is an intermediary between these two surfaces, as evidenced by the trends in reactivity. There may be other elementary reaction steps along the MSR pathway which take advantage the Pd-like qualities of PdZn, and other, such as the fate of CH_2O^*, which are favored by the Cu-like electronic structure.

References

[1] G. Olah, "After oil and gas: methanol economy," *Catalysis Letters*, 2004.

[2] X.-K. Gu and W.-X. Li, "First-Principles Study on the Origin of the Different Selectivities for Methanol Steam Reforming on Cu (111) and Pd (111)," *The Journal of Physical Chemistry C*, vol. 114, pp. 21539–21547, Dec. 2010.

[3] K. H. Lim, Z.-X. Chen, K. M. Neyman, and N. Rösch, "Comparative Theoretical Study of Formaldehyde Decomposition on PdZn, Cu, and Pd Surfaces," *The Journal of Physical Chemistry B*, vol. 110, pp. 14890–14897, Aug. 2006.

[4] B. Hammer and J. K. Nørskov, "Electronic factors determining the reactivity of metal surfaces," *Surface Science*, vol. 343, no. 3, pp. 211–220, 1995.

[5] A. Nilsson, L. G. M. Pettersson, B. Hammer, T. Bligaard, C. H. Christensen, and J. K. N rskov, "The electronic structure effect in heterogeneous catalysis," *Catalysis Letters*, vol. 100, pp. 111–114, Apr. 2005.

[6] S. Lin, R. S. Johnson, G. K. Smith, D. Xie, and H. Guo, "Pathways for methanol steam reforming involving adsorbed formaldehyde and hydroxyl intermediates on Cu(111): density functional theory studies.," *Physical Chemistry Chemical Physics*, vol. 13, pp. 9622–9631, May 2011.

[7] R. S. Johnson, A. DeLaRiva, V. Ashbacher, B. Halevi, C. J. Villanueva, G. K. Smith, S. Lin, A. K. Datye, and H. Guo, "The CO oxidation mechanism and reactivity on PdZn alloys," *Physical Chemistry Chemical Physics*, vol. 15, no. 20, pp. 7768–7776, 2013.

[8] G. Henkelman, B. P. Uberuaga, and H. Jonsson, "A climbing image nudged elastic band method for finding saddle points and minimum energy paths," *The Journal of Chemical Physics*, vol. 113, no. 22, pp. 9901–9904, 2000.

[9] K. M. Neyman, K. H. Lim, Z.-X. Chen, L. V. Moskaleva, A. Bayer, R. Denecke, and N. R Sch, "Microscopic models of PdZn alloy catalysts: structure and reactivity in methanol decomposition," *Physical Chemistry Chemical Physics*, vol. 9, no. 27, p. 3470, 2007.

[10] Y. Huang and Z.-X. Chen, "Density Functional Investigations of Methanol Dehydrogenation on PdZn Surface Alloy," *Langmuir*, vol. 26, pp. 10796–10802, July 2010.

[11] J. Greeley and M. Mavrikakis, "Methanol decomposition on Cu (111): A DFT study," *Journal of Catalysis*, 2002.

[12] Z.-X. Chen, K. M. Neyman, K. H. Lim, and N. Rösch, "CH3O decomposition on PdZn(111), Pd(111), and Cu(111). A theoretical study.," *Langmuir*, vol. 20, pp. 8068–8077, Sept. 2004.

[13] S. Lin, D. Xie, and H. Guo, "Pathways of Methanol Steam Reforming on PdZn and Comparison with Cu - The Journal of Physical Chemistry C (ACS Publications)," *The Journal of Physical Chemistry C*, 2011.

Chapter 6

Atomically dispersed Pd on Al_2O_3

This chapter is based in part on the following collaborative work currently under review under the title: *Low Temperature CO Oxidation Catalyzed by Regenerable Atomically Dispersed Palladium on Alumina*, Eric Peterson, Andrew DeLaRiva, Sen Lin, Ryan Johnson, Hua Guo, Jeffrey Miller, Ja Hun Kwak, Charles Peden, Boris Kiefer, Lawrence Allard, Fabio Ribeiro, Abhaya Datye. Please refer to this reference for full experimental details.

6.1 Introduction

In heterogeneous catalysis, only the surface of the material is catalytically active, so increasing the surface area by decreasing the particle size will correspondingly increase the activity of that material. As a result, chemists working in this field have been working with nano particles long before development of the spectroscopic and synthetic tools used today to create and characterize nanostructures. The catalysts used currently to scrub pollutants from combustion engines are composed of small ($\sim 10 - 100$ nm) metallic particles deposited on inert but high surface area oxides such as zeolites, alumina (Al_2O_3) or cerium oxide (CeO_2). Despite the small size of these clusters, there still remain metal atoms inside the particle which are unable to do catalysis, and in this sense wasted. It is reasonable to try to develop catalysts which make use of every metal atom. Towards this end, a number of catalysts have been developed recently that consist of single isolated metal atoms deposited on a supporting material [1–5]. There are, however, no reports of the stabilization of atomically dispersed Pd at elevated temperatures, such as those encountered in automotive catalysts. Increasing the atomic efficiency of catalysts is particularly important for automobile catalytic converters which use expensive Pd, Pt and Rh.

These systems are of interest beyond simply reducing material cost. The geometric and electronic features of supported but isolated metal atoms are quite different

from the surfaces of clean metals slabs or small particles, and can give rise to unique reaction mechanisms. This could lead to enhanced activity, an important goal for automotive catalysts, which must reach an operating temperature of around 200°C before active, as the strong binding energy of CO to these metals active sites are blocked. Lowering the temperature at which these catalysts become active is critical as new engine designs seek efficiency by reducing wasted heat which is subsequently used to activate the catalyst.

In the following, theoretical studies were performed to develop a model for the active site and possible mechanism of CO oxidation for a novel catalyst composed of atomically dispersed Pd on γ-alumina developed and characterized by experimental collaborators.

6.2 Methods

To corroborate the experimental results, plane-wave density functional theory (DFT) calculations have been performed using the Vienna ab initio simulation package (VASP) [6–8] with the gradient-corrected PW91 exchange-correction functional [9]. For valence electrons, a plane-wave basis set was employed with an energy cut-off of 400 eV, while the ionic cores were described with the projector augmented-wave (PAW) method [10, 11]. A 21 unit cell (11.178.41 Å) of the γ-Al_2O_3(100) surface [12] with penta-coordinated Al_3^+ sites exposed, was simulated using a slab supercell approach with periodic boundary conditions. A 2x2x1 Monkhorst-Pack k-point grid [13] was adopted to sample the Brillouin zone, which was found to be converged. This model consists of eight atomic layers with the top four atomic layers relaxed in all calculations. A vacuum spacing of 15 Å was employed to avoid interactions between adsorbates and slab images in the z direction. Geometries were optimized until the maximum force on any ion is less than 0.05 eV/Å. Transition states were calculated

using the CINEB methodology [14, 15]. Bader analysis was performed using the grid based algorithm of Henkelman [16]. Our model for Pd-doped γ-alumina involves the (100) surface of Al_2O_3 with Pd replacing a surface four-coordinate Al.

6.3 Results

6.3.1 Experimental Results

A series of catalysts with a low (0.5 wt%) Pd loading were prepared. Operando X-ray absorption spectroscopy (XAS) studies of these catalysts demonstrate the presence of catalytically active atomically dispersed ionic Pd in these systems. Lanthanum doping was generally found to stabilize this active site, however the role of La has been neglected in this theoretical work. The Pd-O first shell coordination number implies a 4-coordinate square planar geometry which drops towards 3-coordinate under CO oxidation and fully recover upon switching to oxidizing conditions.

The light-off curves (Figure 6.1) were obtained by monitoring CO_2 formation as the catalyst was ramped from room temperature to 300 °C at a rate of 2 °C/min and show onset of catalytic activity at 40°C, indicating that the ionic Pd species are not poisoned by CO. For metallic Pd, CO oxidation is known to be positive first-order with respect to O_2, and negative first-order with respect to CO. [17] The reaction order of these catalysts in CO is significantly reduced towards zero, suggesting a reaction mechanism that is different from that on metallic Pd. Furthermore, turn over frequencies are found to be greater and activation energy considerably lower than on metallic Pd. Low positive order with respect to O_2 is consistent with a Mars van Krevelen mechanism, with the oxygen being derived from the surface, rather than the gas phase.

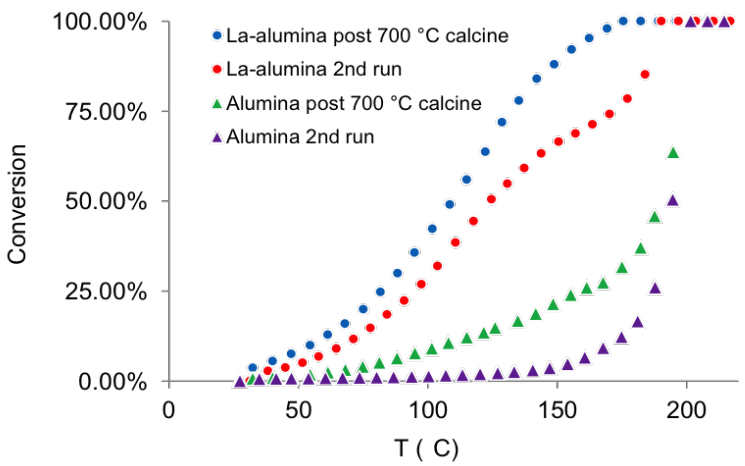

Figure 6.1: CO-oxidation light-off curves for 0.5 wt.% Pd on alumina and La-alumina. The first run was performed after calcining the sample, in situ, at 700 °C for 30 minutes. After the completion of the first run ($T_{max} = 300$ °C), the sample was cooled to room temperature in the reaction mixture and the second run was performed.

6.3.2 DFT Results

Pd doped Al_2O_3

The γ-alumina structure is difficult to study experimentally due to Al vacancies and poor crystallinity, but has been considered to be a defective spinel structure [18]. Recently, however, a series of theoretical studies [19, 20] have proposed a non-spinel structure which is energetically more stable and more reflective of experimental data. Additionally, this structural model captures the essence of the γ-alumina structure in a smaller unit cell than the spinel structure making it more practical for DFT calculations, and hence was used in these studies.

Both the (100) and (110) surfaces of γ-Al_2O_3 were investigated for construction of active sites, as they are expected to be the dominant surfaces comprising roughly 20% and 75% of the surface of alumina particles, respectively [12]. Although these surfaces

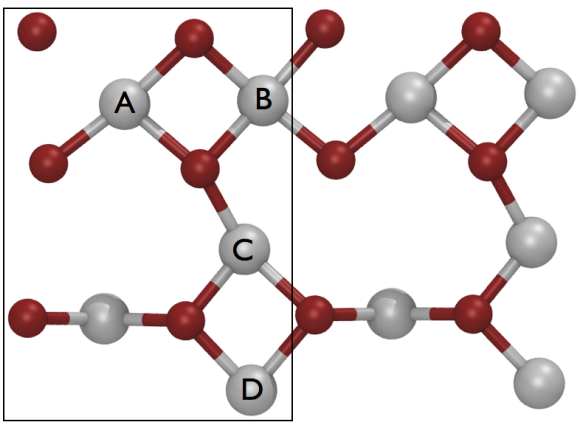

Figure 6.2: The four possible Al atoms which can be replaced with Pd. The unit call is represented by the box on the left.

are expected to have considerable hydroxyl coverage, the 700°C pretreatment of that these catalysts must undergo is expected to remove most if not all hydroxyls, and therefore we consider only hydroxyl free surfaces. Evidence that Pd was coordinated to four oxygen atoms in a square planar structure, as provided from XAS, guided the search for reasonable Al_3^+ vacancy-defect sites that could provide this geometry if Pd were to occupy the defect. Such defects are expected in both the defective spinel and the non-spinel models proposed for the γ-alumina structure. On the (110) surface, no such sites were found. On (100), however there are four such possible sites [21], labeled A-D in Figure 6.2 and all further work focused on the (100) surface.

Although the the formation of these Al vacancy-defects are calculated to be highly unfavorable for all four Al atoms, Site A has the defect formation energy by roughly an electron volt implying that it might be present in higher populations than at other sites. Furthermore, the formation energy of incorporating the Pd atom into the defect is the most exothermic for site A. While Sites A and B both showed square-planar geometry with four equivalent Pd−O bond lengths, Site C had one uniquely

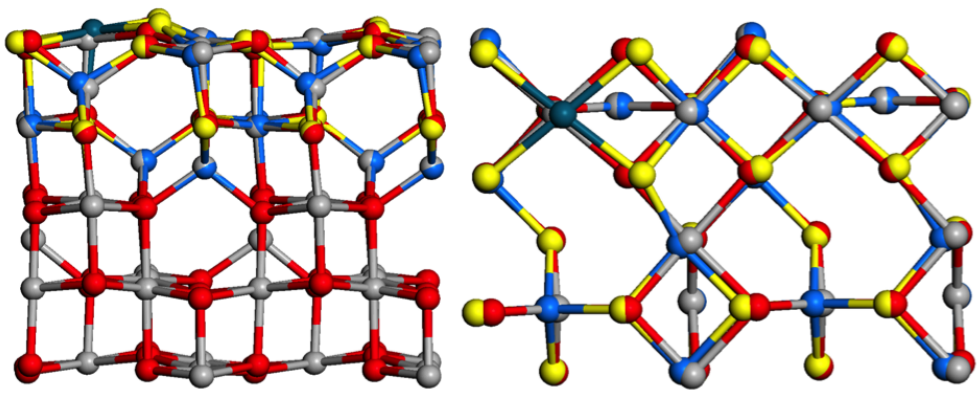

Figure 6.3: Overlay of relaxed and unrelaxed (100) surfaces with a Pd atom in an Al vacancy site. Atom color: O-relaxed (yellow), O-unrelaxed (red), Al-relaxed (light blue), Al-unrelaxed (grey), Pd (dark blue).

long Pd−O bond and in Site D the Pd atom relaxed down below the surface to coordinate with two oxygen atoms in the second layer. On the basis that Site A defects are less unstable and the PdO_4 moiety formed here is the most stable and satisfies experimental geometrical evidence this site was chosen as the model catalyst.

The optimized geometry of the $Pd@Al_2O_3$ system features the Pd atom coordinating with four nearby oxygen atoms, forming a planar geometry. The distances of Pd-O are computed to be 2.11, 2.11, 2.13 and 2.13 Å, which are consistent with the experimental value 2.04 Å. There is a fifth, apical oxygen beneath Pd, with a Pd-O distance of 2.23 Å, which indicates a much weaker interaction. Due to differences in size and electronic structure, the Pd perturbs the surface somewhat, particularly in its vicinity, as can be seen in Figure 6.3. For example, the shifts for the four oxygen atoms coordinated to Pd are found to be +0.23, +0.23, -0.06, -0.06 Å in the z-direction. The Bader charge [22] of the Pd atom is $(+1.04e)$, indicating significant electron transfer from the Pd atom to the surrounding oxygen atoms. The positively charged Pd atom might be responsible for the observed catalytic activity of the $Pd@Al_2O_3$ catalyst.

Adsorption

CO: The carbon monoxide is found to bind atop on the tetra-coordinated Pd atom as illustrated in Figure 6.4 with an adsorption energy of -0.72 eV, which is much smaller than that (-1.97 eV) on Pd(111). The C-O bond length and the Pd−C distance are found to be 1.15 and 1.90 Å, respectively. The angle of O−C−Pd is 174.7°. It should be noted that, after adsorption, the distances between Pd and its surrounding oxygen atoms changed to 2.34, 2.09, 2.37 and 2.11 Å, consistent with experimental results that, during the reaction, the coordination is found to drop to 3 or less. We have also considered the adsorption of CO on Pd in the case of O_2 filling the oxygen vacancy, and the adsorption energy becomes -0.33 eV. The adsorbed CO has a slightly elongated bond length, indicating weakening of the bond. The C−Pd distance is 1.93 Å and the O−C−Pd angle is 170.4°. The distance between C and the upper O (denoted as O_{lat}) atom of the adsorbed O_2 is 2.64 Å, well positioned for reaction. The Pd−O distances are 2.36, 2.25, 2.06 and 2.47 Å when CO is adsorbed.

When CO adsorbs on the top of a Pd atom, the frequency of CO is calculated to be 2105 cm^{-1}, which agrees very well with the experimental observation (2110 cm^{-1}) [23]. This frequency changes to 2078 cm^{-1} after an oxygen molecule fills the vacancy. These frequencies are consistent with the elongation of the CO bond length from π back-bonding from the metal d-orbitals to the π^* CO orbital.

CO_2: The adsorption energy for CO_2 on Pd is very small ($-0.03 \sim -0.05$ eV), indicating it is readily desorbed from the catalyst. The distance between C and Pd is typically larger than 3.00 Å.

O_2: The adsorption energy of the O_2 molecule in the oxygen vacancy, created after CO reacts with surface O, is -2.25 eV and can be seen in Figure 6.4. The distances between Pd and its surrounding three lattice oxygen atoms are 2.15, 2.10 and 2.36 Å. The distances of $O_{gas}-O_{air}$ and $O_{gas}-Pd$ are found to be 1.45 and 1.93

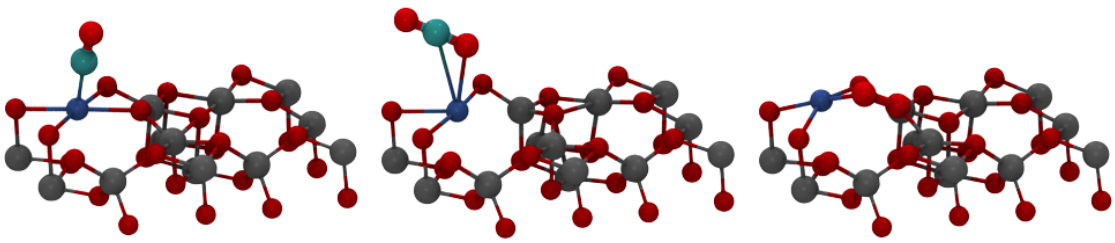

Figure 6.4: Adsorption of CO, CO_2 and O_2 on the Pd active site. The formation of CO_2 produces an oxygen vacancy, which is filled with an O_2 molecule.

Å, respectively, which indicates that molecular oxygen, although not disassociated, is activated upon binding to this site. The angle of Pd−O−O is calculated to be 110.8°.

Reaction Mechanism

A reaction mechanism is proposed based on the DFT calculations as displayed in Figure 6.5, where the energetics are also shown. In this putative mechanism, the catalytic cycle is initiated by the adsorption of CO onto the Pd, which then reacts with a lattice oxygen (O_{lat}) coordinated with Pd. After overcoming an activation barrier of 0.26 eV, an intermediate (iii) was found with ΔE = -0.46 eV. At the transition state, the C−O bond length and the O_{lat} distance are computed to be 1.16 and 1.82 Å, respectively. Several steps are needed to eventually produce CO_2, which promptly desorbs removing O_{lat} in the process (iv). The second half of the catalytic cycle starts with the newly formed oxygen vacancy from the first step, in which now Pd is coordinated by three lattice oxygen atoms with distances of 2.15, 2.27, and 2.49 Å. The adsorption of an O_2 (labeled O_{2gas} or O_{gas} herein) molecule at the vacancy is highly exothermic, with its bond length elongated from 1.23 Å

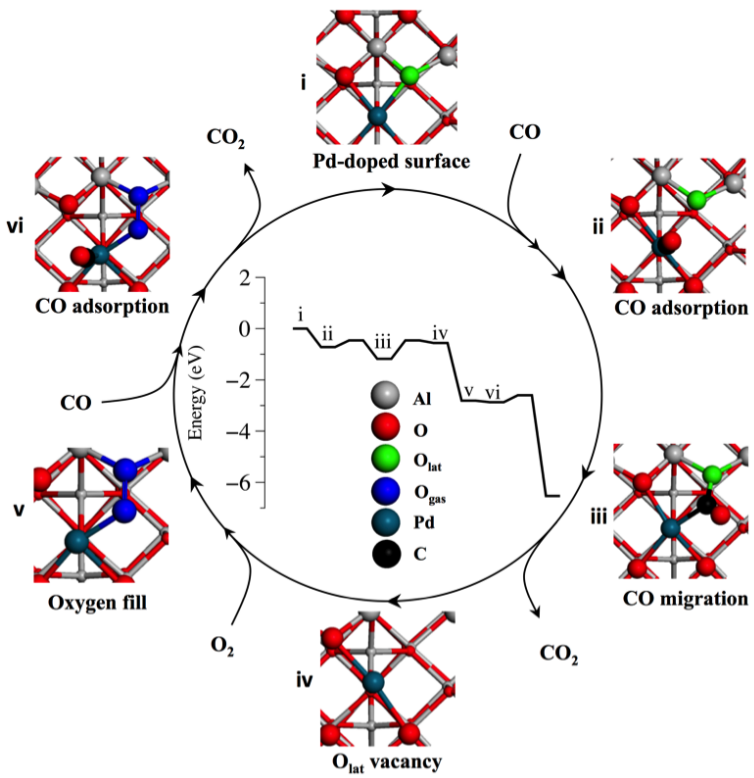

Figure 6.5: Proposed reaction mechanism for CO oxidation on isolated Pd on the γ-alumina(100) surface.

in the isolated molecule to 1.45 Å. This is followed by the adsorption of CO on Pd, which promptly reacts with the pre-adsorbed O_2 gas nearby. This step has an energy barrier of 0.27 eV and the exothermicity is found to be -3.66 eV. At the transition state, the C−O and the C−O_{gas} bond lengths are calculated to be 1.16 and 1.94 Å, respectively. By releasing the CO_2 product, the Pd recovers its tetra-coordinated state on the γ-Al_2O_3(100) surface.

Bader Charge Analysis

Bader charge analysis was performed on the PdO_4 and PdO_3 active site to determine where the charge is distributed upon formation of the O vacancy. In a formal charge picture, the initial 10 electron O^{2-} species is lost as a neutral 8 e^- oxygen atom in CO_2, leaving $2e$ behind to be accounted for. According to the Bader charges, the oxygen atoms in the PdO_4 active site are not formally O^{2-} but closer to $O^{1.5-}$ (-1.5, -1.4, -1.4 and -1.4 specifically), as might be expected in the coordinately-unsaturated surface, a notable departure from an O^{2-} formal charge. Taking the total charge on the Pd and adjacent O atoms before and after the defect formation the Bader values indicate a $0.2e$ difference rather than the $2e$ predicted from formal charges. This is a result of a reorganization of partial charges among the remaining atoms in the active site. Pd is reduced by $0.6e$, and the remaining oxygen atoms bound to Pd are collectively reduced by $0.8e$. The remaining $0.2e$ is then distributed though the 9 nearest Al neighbors coordinated to the oxygen atoms in the active site. Although the Al in Al_2O_3 is typically not considered to be a reducible moiety, we find that one Al bound to two Pd coordinating oxygen atoms in is reduced by $0.17e$. The remaining $0.03e$ is distributed across the remaining adjacent Al atoms. In short, the charge balance for formation of the defect state is achieved as partial charges are distributed throughout the remaining structure. As this analysis shows, it is not appropriate to assign formal charges in this system, as it is for homogeneous analogs. The extended nature of the support allows far more flexibility in distributing partial charges than in the case of relatively small and isolated homogenous catalysts.

6.3.3 Conclusions

In this work a DFT model for isolated single-atom sites of Pd is developed to understand experimental results which demonstrate that γ-alumina supported atomically

dispersed Pd show exceptional activity for CO oxidation at low temperature. This model of Pd atoms stabilized in Al vacancy defects on the (100) surface is consistent with the XAS observations that Pd is coordinated to 4 oxygen atoms in a square-planar geometry. These Pd atoms, being ionic, behave distinctly from that of metallic Pd, which is poisoned by CO at low temperatures. The ionic form of Pd is not poisoned by adsorbed CO since CO is bound less strongly, consistent with our DFT model and the observed positive order in CO oxidation kinetics. Furthermore, the oxygen atoms coordinating the Pd are more labile than in typical alumina surfaces, allowing them to participate in oxidation reactions, consistent with an experimental reaction order with oxygen near zero. At steady-state, the active site could be viewed as two adjacent binding sites: one which immobilizes and slightly activates CO and one that binds and slightly activates molecular oxygen for two sequential oxidation reactions. This proposed catalytic mechanism is consistent with the unexpected low temperature reactivity for the isolated Pd species, whoos calculated barrier (0.27 eV) is similar to the apparent activation energy measured experimentally. Development of atomically dispersed transition metals on high surface area supports is an important step towards more cost-effective catalysts and could provide novel and important mechanistic pathways.

References

[1] S. F. Hackett, R. M. Brydson, M. H. Gass, I. Harvey, A. D. Newman, K. Wilson, and A. F. Lee, "High-Activity, Single-Site Mesoporous Pd/Al2O3 Catalysts for Selective Aerobic Oxidation of Allylic Alcohols," *Angewandte Chemie*, vol. 119, no. 45, pp. 8747–8750, 2007.

[2] B. Qiao, A. Wang, X. Yang, L. F. Allard, Z. Jiang, Y. Cui, J. Liu, J. Li, and T. Zhang, "Single-atom catalysis of CO oxidation using Pt1/FeOx," *Nature Chemistry*, vol. 3, pp. 634–641, July 2011.

[3] S. Abbet, U. Heiz, H. Häkkinen, and U. Landman, "CO Oxidation on a Single

Pd Atom Supported on Magnesia," *Physical Review Letters*, vol. 86, pp. 5950–5953, June 2001.

[4] M. Flytzani-Stephanopoulos, "Gold Atoms Stabilized on Various Supports Catalyze the Water–Gas Shift Reaction," *Accounts of Chemical Research*, 2013.

[5] Y. Guan and E. Hensen, "Cyanide leaching of Au/CeO2: highly active gold clusters for 1, 3-butadiene hydrogenation," *Physical Chemistry Chemical Physics*, vol. 11, no. 41, pp. 9578–9582, 2009.

[6] G. Kresse and J. Hafner, "Abinitio Molecular-Dynamics for Liquid-Metals," *Physical Review B*, vol. 47, no. 1, pp. 558–561, 1993.

[7] G. Kresse and J. Furthmüller, "Efficient iterative schemes for ab initio total-energy calculations using a plane-wave basis set," *Physical Review B*, vol. 54, pp. 11169–11186, Oct. 1996.

[8] G. Kresse and J. Furthmüller, "Efficiency of ab-initio total energy calculations for metals and semiconductors using a plane-wave basis set," *Computational Materials Science*, vol. 6, pp. 15–50, July 1996.

[9] J. P. Perdew, J. A. Chevary, S. H. Vosko, K. A. Jackson, M. R. Pederson, D. J. Singh, and C. Fiolhais, "Atoms, molecules, solids, and surfaces: Applications of the generalized gradient approximation for exchange and correlation.," *Physical review B, Condensed matter*, vol. 46, pp. 6671–6687, Sept. 1992.

[10] P. Blöchl, "Projector augmented-wave method.," *Physical review B, Condensed matter*, vol. 50, pp. 17953–17979, Dec. 1994.

[11] G. Kresse and D. Joubert, "From ultrasoft pseudopotentials to the projector augmented-wave method," *Physical Review B*, vol. 59, no. 3, p. 1758, 1999.

[12] M. Digne, P. Sautet, P. Raybaud, P. Euzen, and H. Toulhoat, "Hydroxyl groups on γ-alumina surfaces: A DFT study," *Journal of Catalysis*, vol. 211, no. 1, pp. 1–5, 2002.

[13] H. J. Monkhorst and J. D. Pack, "Special points for Brillouin-zone integrations," *Physical review B, Condensed matter*, vol. 13, no. 12, pp. 5188–5192, 1976.

[14] H. Jonsson, G. Mills, and K. W. Jacobsen, "Nudged elastic band method for finding minimum energy paths of transitions," in *Classical and Quantum Dynamics in Condensed Phase Simulations* (B. J. Berne, G. Ciccotti, and D. F. Coker, eds.), Singapore: World Scientific, 1998.

[15] G. Henkelman, B. P. Uberuaga, and H. Jonsson, "A climbing image nudged elastic band method for finding saddle points and minimum energy paths," *The Journal of Chemical Physics*, vol. 113, no. 22, pp. 9901–9904, 2000.

[16] W. Tang, E. Sanville, and G. Henkelman, "A grid-based Bader analysis algorithm without lattice bias.," *Journal of Physics: Condensed Matter*, vol. 21, p. 084204, Feb. 2009.

[17] P. J. Berlowitz, C. H. Peden, and D. W. Goodman, "Kinetics of carbon monoxide oxidation on single-crystal palladium, platinum, and iridium," *The Journal of Physical Chemistry*, vol. 92, no. 18, pp. 5213–5221, 1988.

[18] K. Sohlberg, S. J. Pennycook, and S. T. Pantelides, "The bulk and surface structure of γ-alumina," *Chemical Engineering Communications*, vol. 181, pp. 107–135, Sept. 2000.

[19] M. Digne, P. Sautet, P. Raybaud, P. Euzen, and H. Toulhoat, "Use of DFT to achieve a rational understanding of acid–basic properties of γ-alumina surfaces," *Journal of Catalysis*, vol. 226, no. 1, pp. 54–68, 2004.

[20] X. Krokidis, P. Raybaud, A.-E. Gobichon, B. Rebours, P. Euzen, and H. Toulhoat, "Theoretical Study of the Dehydration Process of Boehmite to γ-Alumina," *The Journal of Physical Chemistry B*, vol. 105, pp. 5121–5130, June 2001.

[21] R. Wischert, P. Laurent, C. Copéret, F. Delbecq, and P. Sautet, "γ-Alumina: The Essential and Unexpected Role of Water for the Structure, Stability, and Reactivity of "Defect" Sites," *Journal of the American Chemical Society*, vol. 134, pp. 14430–14449, Sept. 2012.

[22] R. F. Bader, *Atoms in molecules*. Wiley Online Library, 1990.

[23] X. Xu and D. W. Goodman, "An infrared and kinetic study of carbon monoxide oxidation on model silica-supported palladium catalysts from 10-9 to 15 Torr," *The Journal of Physical Chemistry*, vol. 97, no. 29, pp. 7711–7718, 1993.

Chapter 7

$FeO^+ + CH_4$ and H_2

This chapter is based on collaborative work originally found in part in the following publication: S. G. Ard, J. J. Melko, V. G. Ushakov, **R. Johnson**, J. A. Fournier, N. S. Shuman, H. Guo, J. Troe, and A. A. Viggiano, Activation of Methane by FeO +: Determining Reaction Pathways Through Temperature Dependent Kinetics and Statistical Modeling, *The Journal of Physical Chemistry A*, vol. 118, no. 11, pp. 2029-2039, Mar. 2014. Copyright 2014 American Chemical Society. H_2 work is based in part on the work: *Further Insight into the Reaction $FeO^+ + H_2 \longrightarrow Fe^+ + H_2O$: Temperature Dependent Kinetics, Isotope Effects, and Statistical Modeling*, Ard, Shaun; Melko, Joshua; Martinez, Oscar; Ushakov, Vladimir; Li, Anyang; Johnson, Ryan; Shuman, Nicholas; Guo, Hua; Troe, Juergen; Viggiano, Albert, currently under review. Please refer to these for full experimental and kinetic model details.

7.1 Introduction

The iron oxide cation (FeO^+) is capable of reacting with both methane or hydrogen to form methanol or water plus an iron cation, albeit with surprising inefficiency:

$$\begin{aligned} FeO^+(^6\Sigma^+) + CH_4 &\longrightarrow Fe(^6D) + CH_3OH \quad \Delta H_r^\circ = 35.5 \pm 6 \text{kJ/mol} \\ &\longrightarrow FeOH^+ + CH_3 \qquad \Delta H_r^\circ = 1.4 \pm 15 \text{kJ/mol} \end{aligned} \tag{7.1}$$

$$\begin{aligned} FeO^+(^6\Sigma^+) + H_2 &\longrightarrow Fe^+(^6D) + H_2O \quad \Delta H_r^\circ = -154 \pm 6 \text{kJ/mol} \\ &\longrightarrow Fe^+(^4F) + H_2O \quad \Delta H_r^\circ = -139 \pm 6 \text{kJ/mol} \\ &\longrightarrow FeOH^+ + H \qquad \Delta H_r^\circ = 0 \pm 16 \text{kJ/mol} \end{aligned} \tag{7.2}$$

Activation of the CH bond in methane is highly desirable in large part due to methanes abundance and inertness (two deeply interrelated characteristics). According to the EIS's 2013 summary of natural gas reserves [1] the US has over 300,000

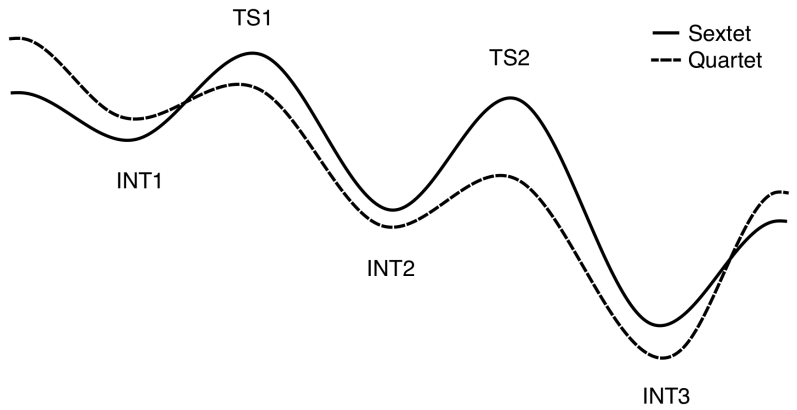

Figure 7.1: Generic potential energy surface for the $FeO^+ + CH_4$ and H_2 reactions.

billion cubic feet of natural gas on reserve, which is primarily composed of methane. Unfortunately, being non-polar, dipole free with negligible electronegativity, and possessing a large homo-lumo gap, is quite resistant to typical acid/base or redox based synthetic approaches. As a result, this plentiful and promising carbon feedstock remains underutilized. A great deal of research has focused on both finding cheap and efficient catalysts for the direct conversion of methane to methanol [2–6].

The reaction between iron oxide cation and molecular hydrogen [7, 8] is one of the simplest examples of bond activation by a transition metal oxide cation [9–11]. As such it provides a nice system for investigating mechanistic details of transition metal catalysis. Despite its deceptive simplicity, it proved to illustrate rich electronic behavior and drove development of Two-State Reactivity (TSR) [12–14].

These two reactions display qualitatively similar and intriguing features as illustrated generically in Figure 7.1. Geometries of the stationary points show that the reactions proceed by first forming pre-reaction complexes in which the reactant molecule associates with the Fe atom. Proton transfer from from either the Fe bound

CH_4 or H_2 to the oxygen atom constitutes the highest TS along both potentials. Both reactions conclude with migration of the remaining reactant to the oxygen atom and then through disassociation to Fe^+ and the appropriate product.

As both reactions are exothermic and spin allowed (both reactant and product have sextet multiplicity derived from the FeO^+ and Fe^+ sextet ground state and closed shell reactants and products), what should be a very efficient reactions proceed at less than 9% for CH_4 and 1% for H_2. Also, both reaction rates are negatively dependent on temperature ($k \sim T^{-1}$), often an indication of a rate determining barrier which is pulled bellow the reactant energy by stable prereaction complexes. This behavior can be explained if the reactions do not proceed along a single spin surface, but rather cross to the quartet surface in order to circumventing large sextet barriers. This is surprising in the context of typical organic reactions, which are usually constrained to the ground state spin surface. When transition metals such as Fe are involved in a reaction, there is sufficient spin-orbit coupling between the nearly degenerate excited spin states that crossing becomes possible. TSR has been found to be applicable to many organometallic systems including enzymatic reactions. [12, 13, 15–26]

A survey of the numerous potential energy surfaces, both in the literature and generated in this work show significant disparity and few identify a negative barrier implied by the negative temperature dependence. Unfortunately, simulations of the reactivity based on the *ab initio* energetics fail to reproduce the observed magnitude and temperature dependence of the rate constants, suggesting significant uncertainties in the characterization of the transition state region. This is particularly annoying because the range of uncertainty for these barriers can changes the sign of the barrier. We surprisingly conclude that chemically accurate energetics for these relatively small systems are still are beyond the capabilities of the state-of-the-art computational chemistry.

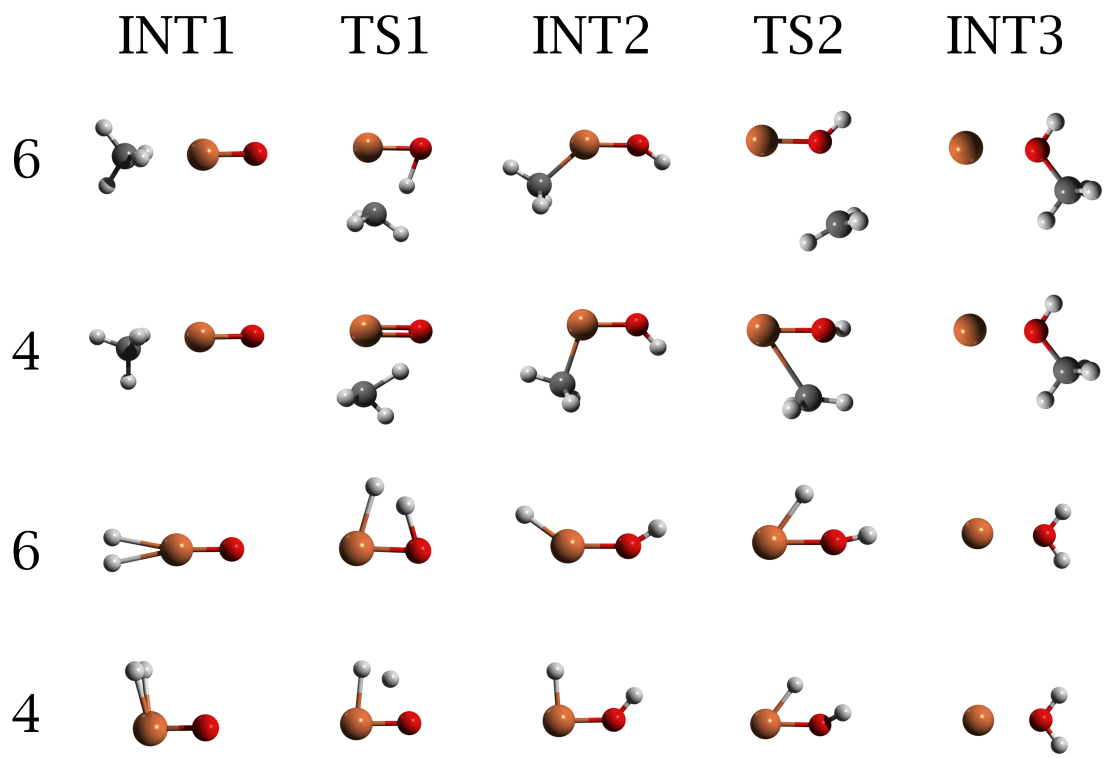

Figure 7.2: The structures for all stationary states in Figure 7.1 for CH_4 (top) and H_2 (bottom).

Despite the previous large body of work on these reactions, several fundamental questions about the system remain unresolved. What are the transition state barriers? And what is the rate determining step responsible for such inefficiency; crossing spin-surfaces or surmounting transition states? This requires knowledge of the lifetimes and populations of the various intermediates. The kinetic models used in the following work provides unique insight into these questions.

With the computational avenue being problematic, we turn instead to a statistical adiabatic channel approach [27–29], using the *ab initio* information of the stationary points along the reaction path as guides but leaving their energies as fitting

parameters. The modeling must fit the magnitude of the total rate constant, the temperature dependence of the total rate constant over a wide range, the product branching ratios at all temperatures and the isotope effect. As such, the modeling is severely overdetermined, and success in reproducing the data not only suggest mechanistic insight but also provide energetics which surpass current quantum chemical calculations in accuracy, of the rate-limiting transition state heights.

7.2 Computational Methods

The stationary points along the reaction pathways for the $FeO^+ + CH_4 \longrightarrow Fe^+ + CH_3OH$ and $FeO^+ + H_2 \longrightarrow Fe^+ + H_2O$ reactions have been evaluated with the CBS-QB3 method, [30] similar to that reported by Altinay et al. [31] for methanol. This composite method performs a geometry optimization and frequency calculations at the B3LYP/CBSB7 (6-311G(2d,d,p)) level, followed by a series of additional single-point calculations with larger basis sets and higher levels of theory to extrapolate to what is typically considered a very accurate value for the energy. There is strong evidence that B3LYP performs adequately in structural determination for systems involving transition metals, [32, 33] but the energetics might contain significant errors. Furthermore, most previous attempts [16, 31, 34–41] to model the potential energy surfaces of this reaction have mostly been based on density functional theory (DFT) methods and, in particular, the B3LYP functional.

To obtain better estimates of energetics, the CBS-QB3 protocol performs single point calculations at CCSD(T)/6-31+G(d) and MP4SDQ/CBSB4 levels on the geometry determined with B3LYP, and then, the final infinite basis set energy is extrapolated with pair natural orbital energies at the MP2/CBSB3 level. Additionally, a correction for spin contamination is included based on the $\langle S2 \rangle$ eigenvalue from MP2/CBSB3. CBS calculations were performed using the GAUSSIAN 09 software

suite. [42] The energy values reported are those at 0 K and include the zero-point energy corrections from the B3LYP-derived frequencies. The vibrational frequencies and rotational constants of the stationary points were obtained at the B3LYP level.

In addition, a number of higher level methods were explored to account for electron correlation effects and multireference character. These methods include CASSCF, [43, 44] CCSD(T), [45] its explicitly correlated CCSD(T)-F12 variant [46], complete active space second-order perturbation theory (CASPT2) [47, 48] and multi-reference configuration interaction (MRCI) [49, 50] approaches. The multi-reference methods (CASSCF, CASPT2 and MRCI) and CCSD-F12 calculations were performed using the MOLPRO suite of electronic structure programs, [51] and the other calculations were implemented in Gaussian 09 package [42].

7.3 Results

7.3.1 $\mathbf{FeO^+ + CH_4 \longrightarrow Fe^+ + CH_3OH}$

Experimental Results

The total rate constants for the reaction of FeO^+ with both CH_4 and CD_4 from 123 to 700 K are summarized in Table 7.1. The rate constant for FeO^+ with CH_4 at 300 K was found to agree with the consensus of those previously reported, [52] occurring at about 9% of the collision rate constant. The reaction with CD_4 is found to be somewhat less efficient, with only about 5% of collisions leading to reaction at room temperature.

Reaction		k (300K) (10^{-10} cm^3/s)	lit. values (300K) (10^{-10} cm^3/s)	reaction efficiency k/k_{coll}
$FeO^+ + CH_4$	$\longrightarrow Fe^+ + CH_3OH$ (52%) $\longrightarrow FeOH^+ + CH_3$ (48%)	0.95	2.0(b), 0.85(c), 0.28(d), 0.74(e)	9.1×10^{-2}
$FeO^+ + CD_4$	$\longrightarrow Fe^+ + CD_3OD$ (79%) $\longrightarrow FeOD^+ + CD_3$	0.51	na	5.4×10^{-2}

Table 7.1: Experimental Rate Constant (k), Reaction Efficiency, And Kinetic Isotope Effect (KIE) at 300 Ka. (a) The error in our rate constant measurement is estimated at ±25%. (b) ICR-derived rate constant from ref [53]. (c) ICR-derived rate constant from ref [52]. (d) GIB-derived rate constant from ref [52]. (e) SIFT-derived rate constant from ref [52].

Computational Results

A number of researchers [16, 24–26, 31, 34] have used the $FeO^+ + CH_4$ reaction to investigate Two State Reactivity and the reaction pathways have been primarily been explored by DFT studies, although some are augmented with higher-level energy corrections. The qualitative PESs and geometries for the quartet and sextet states are depicted in Figure 7.1 and 7.2. The calculations all indicate a crossing between the quartet and sextet PESs somewhere before the TS1 allowing the system to access a much lower barrier along the quartet surface.

Our CBS-QB3 energy for ^{4}TS1 relative to that for the sextet FeO^+ reactants is slightly negative (7.72 kJ mol^{-1}), which is quite similar to those reported earlier by other theoretical calculations. [31] This submerged barrier is consistent with the negative temperature dependence of the rate constants at low temperatures. However, as discussed below, the *ab initio* value for this reaction bottleneck is probably not quantitatively accurate, evidenced by the much more negative value determined by the statistical fit of the experimental rate constants presented below. With the less negative (or positive) values for the bottleneck from the *ab initio* calculations (see below), statistical modeling would obtain a rate constant significantly smaller than that observed experimentally.

Stationary point	HF	B3LYP	CBS-QB3 Current work (ref [6])	CCSD(T)-F12 AVTZ	CCSD(T) AVTZ Current work (ref [6])	exp.derived values	kinetic model determined values
$^4FeO^+ + CH_4$	-76.8	52.5	24.1 (25)	50.5	49.5 (45)	∼34.6 [55]	
$^6Fe^+ + CH_3OH$	-304.9	-29.8	-35.9 (-36)	-36.6	-52.0 (-49)	-35.5±6 [7, 8]	-34.6
$^4Fe^+ + CH_3OH$	-114.0	-21.7	-39.8 (-6)	-24.4	-30.0 (-31)	-10.6±6 [7, 8, 56])	-9.7
$^5FeOH^+ + CH_3$	-209.7	-21.7	-22.8 (-23)	-6.4	-5.4	-1.4±15 [7, 8]	-0.6
^{6}TS1	113.9	44.0	40.1 (40)	56.9	(60)		
^{4}TS1		-4.22	-7.9 (-1)	11.8	(12)		-22.5

Table 7.2: Comparison of the energetics of key species along the reaction path between theoretical and experimental values. All energies are relative to reactants (kJ mol^{-1}) The literature values for CBS-QB3 and CCSD(T) are given in parentheses.

In order to gain a better understanding of the energetics, we performed single-point calculations using the CCSD(T) method. Similar calculations have been reported before but with a relatively small basis set. [31] Here, the explicitly correlated version of CCSD(T)-F12 was used with the AVTZ basis set, which is expected to provide results with CBS quality. [54] The results shown in Table 7.2 suggests that the previous CCSD(T) results are well-converged with the basis set. More importantly, it shows that the ^{4}TS1 is 11.8 kJ mol^{-1} above the reactant, in worse agreement with the kinetic data.

The data in Table 7.2 underscore many of the challenges in describing this system theoretically. Hartree-Fock theory, as is expected, fails badly due apparently to the paramount importance of electron correlation. B3LYP, which incorporates electron correlation, tends to do a far better job, as noted in previous studies. [32, 33] The higher-level composite CBS-QB3 method only marginally improves upon the B3LYP values. In addition, it fails to describe the relative ordering of the two spinorbit levels of the Fe^+ atom, incorrectly predicting the quartet to be more stable than the sextet by 8.1 kJ mol^{-1}. The CCSD(T)-F12 method does describe asymptotic regions well but fails to predict a submerged ^{4}TS1, finding it to be 11.8 kJ mol^{-1} above the reactant asymptote. Due to the failures of what are often considered reliable methods, we have concluded that an alternative approach is necessary to shed light on the energetics of this reaction.

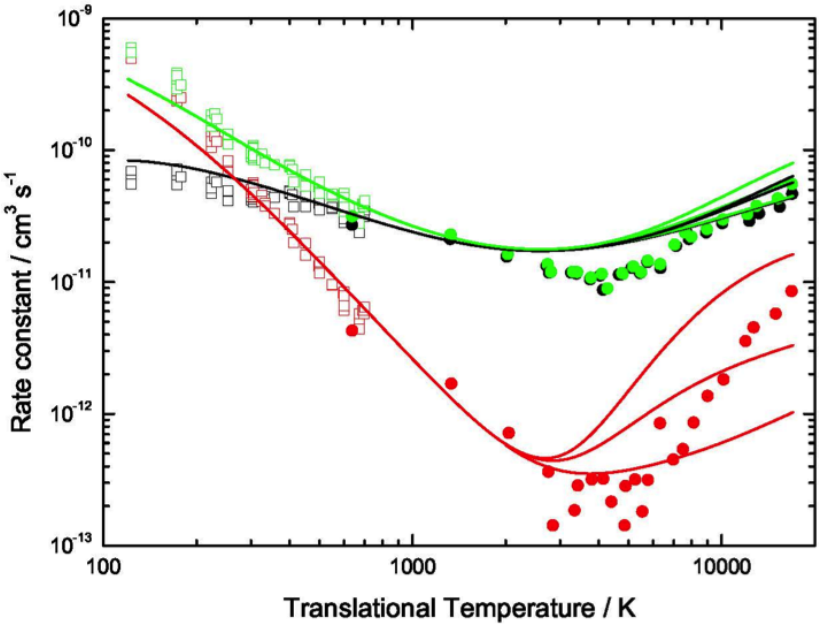

Figure 7.3: Statistical modeling of rate constants for $FeO^+ + CH_4$ from present work (squares) and from GIB experiments of ref. [35] (filled circles). Green: total rate constants, red: rate constants for formation of $Fe^+ + CH_3OH$, black: rate constants for formation of $FeOH^+ + CH_3$. Lines: model.

The inconsistency may have several possible origins. First, the CBS-QB3 and CCSD(T)-F12 calculations used the B3LYP geometry for the stationary points, which might be different at the higher levels of theory. Second, the system may have significant multireference character due to the numerous low-lying excited states. The T1 diagnostic value at the ^{4}TS1 is 0.07, significantly higher than the recommended cutoff value of 0.02 for single-reference systems. [57] However, multireference *ab initio* calculations involving transition metals, particularly with geometry optimization, are computationally formidable.

Reaction	k(300K) (10^{-12} cm^3s^{-1})	lit.values (10^{-12} $cm^3s{-}1$)	efficiency (k/k_{coll})	T dep.
$FeO^+ + H_2 \longrightarrow Fe^+ + H_2O$	10	10a, 8.8b	.0066	T-1±0.1
$FeO^+ + D_2 \longrightarrow Fe^+ + D_2O$	5.1	6.9a, 4.2b, 2.5c	.007	T-1±0.1
$FeO^+ + HD \longrightarrow Fe^+ + HDO$	8.7	8.1a, 7.7b	.0047	T-1±0.1

Table 7.3: Room temperature rate constant (k), reaction efficiency (k/k_{coll}), and temperature dependence for the reactions of FeO^+ with H_2, D_2, and HD (Errors in the rate constants are estimated at 10% relative and 25% absolute). Refs: a. IRC derived rate, b. SIFT derived rate, c. GIB derived rate all from Ref. [52]

Kinetic Modeling

In our statistical modeling, we rely on the vibrational frequencies and rotational constants such as those derived by DFT calculations. As discussed above, energies are not known with sufficient accuracy for use in the modeling, though these calculations provide reasonable measures of the frequencies [31]. Therefore, it appeared reasonable to leave the energies of the reactants and the products as fit parameters in the modeling. Furthermore, the energy of the ^{4}TS1 between the ^{4}INT1 and ^{4}INT2 complexes was kept as a third fit parameter. The results of the statistical modeling sensitively depend on these three fit parameters such that the present approach likely provides a better representation of these quantities than the *ab initio* values. We calculate $k_B(T)$ and $k_C(T)$ while varying the three energy parameters mentioned above. We then perform mean-least-squares fits of the modeling to the experimental results presented here and in ref [35]. The results are shown in Figure 7.3, and the resulting fitted energies are collected in Table 7.2.

7.3.2 $FeO^+ + H_2 \longrightarrow Fe^+ + H_2O$

Experimental Results

The room temperature rate constants measured for the reactions of FeO^+ with H_2, D_2, and HD are shown in Table 7.3. The rate constants are found to proceed very inefficiently, agreeing well with previously published room temperature rate constants and vary strongly with temperature for each of the three reactions, scaling as $\sim T^{-1}$.

Computational Results

Again, refer to Figures 7.1 and 7.2 for schematic PESs and geometries for the $FeO^+ + H_2 \longrightarrow Fe^+ + H_2O$ reaction. To assess the large number of PESs found in the literature and produced in this work, a few benchmark values are chosen: the spin-orbit splitting between the ground state sextet and the first quartet of Fe^+ and FeO^+, the barrier height of ^{4}TS1 relative to the sextet reactant asymptote, and the barrier height of ^{4}TS1 relative to ^{4}INT, which provides information about the performance of various electronic structure methods in predicting the barrier height in a single electronic state and the overall exothermicity of the reaction (ΔE_{rxn}) from sextet reactants to sextet products. These values are summarized in Table 7.4 for B3LYP, CBS-QB3, CCSD(T), CASSCF, CASPT2 and MRCI as well as previously reported studies using B3LYP, diffusion Monte Carlo (DMC) and CCSD(T) single point results at B3LYP geometries. CASSCF was performed with 13 active electrons in 11 orbitals, CASPT2 and MRCI were carried out using the CAS-configurations as the reference configuration state functions. This active space is similar to previous CASSCF/MRCI studies on FeO^+ [58, 59].

Experimental spin-orbit splittings are available for Fe^+ and FeO^+, being 24.1 and 47.3 kJ/mol respectively [55, 56]. B3LYP does a fair job of capturing these

Method	Basis	Fe^+ (6-4)	FeO^+ (6-4)	^{6}TS1−^{6}INT1	^{4}TS1	ΔE_{rxn}
Modeled Values (this work)	–				-0.33	
Expt.	–	24.1	47.3	——	——	——
B3LYP	TZVP	28	61.8	102.3	14.5	-159.2
CBS-QB3	na	-2.9	24.1	103.2	5.8	-144.7
CCSD(T)	cc-PVDZ / SDD	88.8	-41.5	110	34.7	-194.9
	cc-PVTZ / SDD at above geometry	88.8	52.1	104.2	22.2	-217.1
	cc-PVTZ	49.2	47.3	——	——	——
CASSCF	aug-cc-pVTZ / cc-pVTZ for H	105.2	——	——	44.4	-258.6
CASPT2	aug-cc-pVTZ/ cc-pVTZ for H	95.5	——	——	56	-158.2
MRCI	AVTZ	99.4	41.5	——	12.5	-167.9
(REF [60])	B3LYP	-10.6	33.8	99.4	0	-161.1
	(BP86)	(-18.3)	-53.1	-117.7	0	
(REF [41])	DMC	30.9	52.1	107.1	5.8	-208.4
(REF [40])	B3LYP / CCSD(T)	28	53.1	96.5	-5.8	-159.2

Table 7.4: Various calculated and previously reported values of key features of the $FeO^+ + H_2$ PES in kJ/mol

values, and are comparable to CCSD(T)/cc-PVTZ and DMC. CBS-QB3 fails badly with the Fe^+ atom, reversing the order of the sextet and quartet states. As far as overall exothermicity of the reaction is concerned, B3LYP, CBS-QB3 and CASPT2 all perform well, falling within 9.6 kJ/mol of the experimental value of 154±6 kJ/mol [7, 8]. CASSCF and CCSD(T) fare the worst, overestimating the energy by at least 48 and as much as 96 kJ/mol. The success of the CASPT2 is not surprising because it maintains the size constancy necessary to evaluate the ΔE_{rxn} without basis superposition error. CCSD(T) likely fails due to the use of the SDD effective core potential on Fe and an unconverged basis set. However, full electron calculations were not attempted other than for Fe^+ and FeO^+, due to formidable computational costs. The key quantity investigated in this work is the relative barrier height of ^{4}TS1, which shows considerable variation among methods. Importantly, due to the fact that the barrier is so close to the energy of the reactants, slight variation will cause the sign of the barrier energy to change, giving qualitatively different behavior at this

rate determining step. Of the methods surveyed here only one predicted a slightly negative barrier, as might be expected from the negative temperature dependence of the reaction rate. The CCSD(T) single point calculation on B3LYP geometries of ref. 19 find this barrier to be -5.8 kJ/mol. DMC and CBS-QB3 gave the second lowest barriers at +5.8 kJ/mol, followed closely by MRCI and B3LYP values at +12.5 and +14.5 kJ/mol, respectively. The highest barriers are found in CCDS(T), CASSCF, CASPT2 and MRCI calculations. The failure of CCSD(T) is again likely due to the use of the SDD potential for Fe, and there is evidence that the failure of CASPT2 and MRCI are due to a choice of an active space too small to accurately capture the correlation and the multi-reference character of the wavefunctions. Unfortunately, a larger active space is prohibitively costly, but we believe that this is the most appropriate methodology for an accurate description of the reaction path.

Since a possible source of error is the splitting of the two spin states of FeO^+, the absolute barrier height along the sextet potential energy surface can provide insight into the accuracy of the method independent of the splitting. In general, most methods find the height of ^{6}TS1 to be around 96.5 kJ/mol above ^{6}INT1, and the largest values correspond to methods which over estimate the ^{4}TS1 barrier. The lowest value, of 96.5 kJ/mol at CCSD(T)/B3LYP, also corresponds to the method that produced the lowest barrier found for ^{4}TS1. This methodology was also very accurate for the spin-orbit splitting of Fe^+ and FeO^+ species.

In Table 7.5 we have compared the geometry of ^{4}TS1 obtained using CBS-QB3, CCSD(T) and CASSCF. In general, the transition-state structure becomes progressively looser in that all bond lengths increase in this order. The CBS-QB3 and CCSD(T) results are more similar to each other than CASSCF, in which bond lengths can be as much as 0.2 Å longer. The CBS-QB3 values are closest to previously published geometries [17, 40, 60], albeit this is not to be unexpected considering these previous studies are also DFT based.

TS4	R_{FeO}	R_{H1H2}	R_{FeH1}	R_{FeH2}	A_{OFeH1}	A_{OFeH2}
CBS-QB3	1.603	0.916	1.703	1.665	52.2	83.7
CCSD(T)	1.656	0.922	1.760	1.704	48.6	79.4
CASSCF	1.759	0.944	1.925	1.825	40.9	69.9
DFT (Ref. [37])	1.630	1.010	1.650			
B3LYP (Ref. [60])	1.620	0.930		1.689		
B3LYP (Ref. [17])	1.612	0.916		1.687		

Table 7.5: Geometrical parameters of ^{4}TS1 for $FeO^+ + H_2$ calculated at various methods in Å and degrees.

Despite a known problem in calculating the splitting of nearly degenerate spin states in Fe(II) compounds with sulfur ligands [61], B3LYP is known to perform quite well in determining bond dissociation energies of MO^+ complexes with respect to other DFT functionals [32]. It has also been found to provide reasonable geometries [62] and is commonly used to provide starting geometries for more accurate single point evaluations as is the case in ref. [40]. In this spirit we have chosen to utilize the geometries and vibrational frequencies as found in the CBS-QB3 method, which is B3LYP with the reasonably large 6-311G basis with Fe, O and H receiving 2d, d and p polarization functions respectively. The molecular parameters obtained and used in the statistical modeling are given in the supplemental materials.

Kinetic Modelling

The results of our modeling of the present thermal rate constants $k_{tot}(T)$ over the range 173-673 K, as well as the experimental points from the present work, are illustrated in Fig. 7.4. The curve for H_2 is fitted with ^{4}TS1 energies of -0.33 kJ mol^{-1}. For HD, the two different ^{4}TS1 values were found to be -0.48 kJ mol^{-1} and -2.03 kJ mol^{-1}, and -1.81 kJ mol^{-1} was obtained for D_2. Within the estimated uncertainty of present quantum chemical calculations, they agree with the quantum

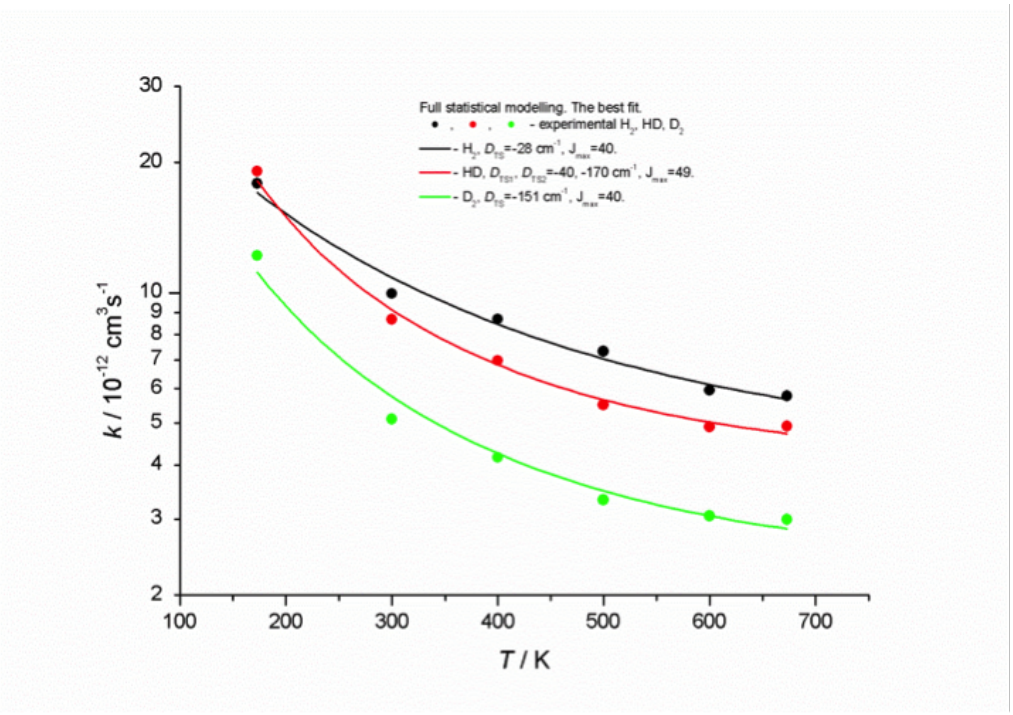

Figure 7.4: Rate constants and statistical modeling for the reactions of FeO^+ with H_2, HD, and D_2

chemical values given in Table 7.4 and particularly well with the the result from ref. [40]. We note in addition that the isotope dependence of the fitted experimental energy values reproduces the results from the present quantum chemical calculations.

7.4 Conclusions

Thorough understanding of fundamental reaction mechanisms in numerous aspects of organometallic chemistry is currently inhibited by an inability to precisely map out the energetic landscape of the reaction. For example, modeling of the crossing efficiency in cases of two-state reactivity such as this would greatly benefit from an approximation of the complex lifetime in the vicinity of the crossing, as well as its

energy dependence. These quantities are highly dependent, however, on the relative energetics of the complex as well as the neighboring transition states, which state-of-the-art calculation methods have had little success in describing energetically.

To this end, experimentally determined temperature dependent rate constants for the reactions of FeO^+ with H_2, CH_4 and their isotopologues were used in conjunction with kinetic and computational models to shed new light on the mechanistic details of these important reactions. The combination of multiple near degenerate electronic states, the multi-reference nature of the system (particularly at the transition states where bond breaking and formation are occurring) and electron correlation all present in these cases of two-state reactivity prove challenging for current quantum chemical models. Contrary to previous interpretations of these reactions, we find spin-inversion to be efficient and crossing of the first quartet transition state to be rate limiting in both cases. The refined energies of ^{4}TS1 are found to be -22 kJ mol^1 and -0.33 kJ mol^{-1} for CH_4 and H_2 respectively.

References

[1] US Energy Information Administration, "Natural Gas Dry, Proved Reserves as of Dec. 31." http://www.eia.gov/dnav/ng/ng_enr_sum_a_EPG0_R11_BCF_a.htm, Apr. 2014.

[2] H. D. Gesser, N. R. Hunter, and C. B. Prakash, "The direct conversion of methane to methanol by controlled oxidation," *Chemical Reviews*, vol. 85, pp. 235–244, Aug. 1985.

[3] N. R. Foster, "Direct catalytic oxidation of methane to methanol — a review," *Applied Catalysis*, vol. 19, pp. 1–11, Jan. 1985.

[4] H. Schwarz, "Chemistry with Methane: Concepts Rather than Recipes," *Angewandte Chemie International Edition*, vol. 50, pp. 10096–10115, June 2011.

[5] Z.-C. Wang, N. Dietl, R. Kretschmer, J.-B. Ma, T. Weiske, M. Schlangen, and H. Schwarz, "Direct Conversion of Methane into Formaldehyde Mediated by [Al2O3].+ at Room Temperature," *Angewandte Chemie International Edition*, vol. 51, pp. 3703–3707, Mar. 2012.

[6] Z.-C. Wang, X.-N. Wu, Y.-X. Zhao, J.-B. Ma, X.-L. Ding, and S.-G. He, "Room-temperature methane activation by a bimetallic oxide cluster," *Chemical Physics Letters*, vol. 489, no. 1, pp. 25–29, 2010.

[7] E. Goos, A. Burcat, and B. Ruscic, *Extended third millennium ideal gas and condensed phase thermochemical database for combustion with updates from active thermochemical tables*. 2010.

[8] D. Schröder, "Gaseous Rust: Thermochemistry of Neutral and Ionic Iron Oxides and Hydroxides in the Gas Phase ," *The Journal of Physical Chemistry A*, vol. 112, pp. 13215–13224, Dec. 2008.

[9] D. K. Bohme and H. Schwarz, "Gas-phase catalysis by atomic and cluster metal ions: the ultimate single-site catalysts.," *Angewandte Chemie (International ed. in English)*, vol. 44, pp. 2336–2354, Apr. 2005.

[10] P. Armentrout, "Reactions and thermochemistry of small transition metal cluster ions.," *Annual Review of Physical Chemistry*, vol. 52, pp. 423–461, 2001.

[11] D. Schröder and H. Schwarz, "C-H and C-C Bond Activation by Bare TransitionMetal Oxide Cations in the Gas Phase," *Angewandte Chemie (International ed. in English)*, vol. 34, no. 18, pp. 1973–1995, 1995.

[12] S. Shaik, D. Danovich, A. Fiedler, D. Schr der, and H. Schwarz, "Two-State Reactivity in Organometallic Gas-Phase Ion Chemistry," *Helvetica Chimica Acta*, vol. 78, pp. 1393–1407, Sept. 1995.

[13] D. Schröder, S. Shaik, and H. Schwarz, "Two-State Reactivity as a New Concept in Organometallic Chemistry §," *Accounts of Chemical Research*, vol. 33, pp. 139–145, Mar. 2000.

[14] S. Shaik, "An Anatomy of the Two-State Reactivity Concept: Personal Reminiscences in Memoriam of Detlef Schröder," *International Journal of Mass Spectrometry*, 2013.

[15] L. Zhao, Y. Wang, W. Guo, H. Shan, X. Lu, and T. Yang, "Theoretical Investigation of the Fe +-Catalyzed Oxidation of Acetylene by N 2O," *The Journal of Physical Chemistry A*, vol. 112, pp. 5676–5683, June 2008.

[16] Y. Shiota and K. Yoshizawa, "A spin–orbit coupling study on the spin inversion processes in the direct methane-to-methanol conversion by FeO+," *The Journal of Chemical Physics*, vol. 118, no. 13, p. 5872, 2003.

[17] S. Chiodo, O. Kondakova, M. d. C. Michelini, N. Russo, E. Sicilia, A. Irigoras, and J. M. Ugalde, "Theoretical Study of Two-State Reactivity of Transition Metal Cations: The "Difficult" Case of Iron Ion Interacting with Water, Ammonia, and Methane," *The Journal of Physical Chemistry A*, vol. 108, pp. 1069–1081, Feb. 2004.

[18] P. B. Armentrout, "Chemistry of excited electronic States.," *Science*, vol. 251, pp. 175–179, Jan. 1991.

[19] X.-L. Sun, X.-R. Huang, J.-L. Li, R.-P. Huo, and C.-C. Sun, "Mechanism Insights of Ethane C–H Bond Activations by Bare [Fe IIIO] +: Explicit Electronic Structure Analysis," *The Journal of Physical Chemistry A*, vol. 116, pp. 1475–1485, Feb. 2012.

[20] N. Harris, S. Shaik, D. Schröder, and H. Schwarz, "Single- and Two-State Reactivity in the Gas-Phase CH Bond Activation ofNorbornane by 'Bare' FeO+," *Helvetica Chimica Acta*, vol. 82, pp. 1784–1797, Oct. 1999.

[21] H. Schwarz, "On the spin-forbiddeness of gas-phase ion–molecule reactions: a fruitful intersection of experimental and computational studies," *International Journal of Mass Spectrometry*, vol. 237, no. 1, pp. 75–105, 2004.

[22] N. Dietl, M. Schlangen, and H. Schwarz, "Thermal Hydrogen-Atom Transfer from Methane: The Role of Radicals and Spin States in Oxo-Cluster Chemistry," *Angewandte Chemie International Edition*, vol. 51, pp. 5544–5555, Mar. 2012.

[23] R. E. White and M. J. Coon, "Oxygen Activation by Cytochrome P-4501," *Annual Review of Biochemistry*, vol. 49, pp. 315–356, June 1980.

[24] D. Schroeder, A. Fiedler, J. Hrusak, and H. Schwarz, "Experimental and theoretical studies toward a characterization of conceivable intermediates involved in the gas-phase oxidation of methane by bare FeO+. Generation of four distinguishable [Fe,C,H4,O]+ isomers," *Journal of the American Chemical Society*, vol. 114, pp. 1215–1222, Feb. 1992.

[25] K. Yoshizawa, Y. Shiota, and T. Yamabe, "MethaneMethanol Conversion by MnO +, FeO +, and CoO +: A Theoretical Study of Catalytic Selectivity," *Journal of the American Chemical Society*, vol. 120, pp. 564–572, Jan. 1998.

[26] K. Yoshizawa, Y. Shiota, and T. Yamabe, "Reaction Paths for the Conversion of Methane to Methanol Catalyzed by FeO+," *Chemistry - A European Journal*, vol. 3, pp. 1160–1169, July 2005.

[27] J. Troe, "Statistical adiabatic channel model for ion–molecule capture processes," *The Journal of Chemical Physics*, vol. 87, no. 5, p. 2773, 1987.

[28] J. Troe, "Rotational effects in complex-forming bimolecular reactions: Application to the reaction CH_4+ $O_2{}^+$," *International journal of mass spectrometry and ion processes*, vol. 80, pp. 17–30, 1987.

[29] J. Troe and V. G. Ushakov, "A Simple Method Relating Specific Rate Constants k (E, J) and Thermally Averaged Rate Constants k(T) of Unimolecular Bond Fission and the Reverse Barrierless Association Reactions," *The Journal of Physical Chemistry A*, vol. 110, no. 21, pp. 6732–6741, 2006.

[30] J. A. Montgomery, M. J. Frisch, J. W. Ochterski, and G. A. Petersson, "A complete basis set model chemistry. VI. Use of density functional geometries and frequencies," *The Journal of Chemical Physics*, vol. 110, no. 6, pp. 2822–2827, 1999.

[31] G. Altinay, M. Citir, and R. B. Metz, "Vibrational Spectroscopy of Intermediates in Methane-to-Methanol Conversion by FeO +," *The Journal of Physical Chemistry A*, vol. 114, pp. 5104–5112, Apr. 2010.

[32] X. Zhang and H. Schwarz, "Bonding in cationic MOH n + (M = K La, Hf Rn; n = 0–2): DFT performances and periodic trends," *Theoretical Chemistry Accounts*, vol. 129, pp. 389–399, Dec. 2010.

[33] M. N. Glukhovtsev, R. D. Bach, and C. J. Nagel, "Performance of the B3LYP/ECP DFT Calculations of Iron-Containing Compounds," *The Journal of Physical Chemistry A*, vol. 101, pp. 316–323, Jan. 1997.

[34] H. J. Kulik and N. Marzari, "A self-consistent Hubbard U density-functional theory approach to the addition-elimination reactions of hydrocarbons on bare FeO+," *The Journal of Chemical Physics*, vol. 129, no. 13, p. 134314, 2008.

[35] Y. Shiota and K. Yoshizawa, "Methane-to-Methanol Conversion by First-Row Transition-Metal Oxide Ions: ScO +, TiO +, VO +, CrO +, MnO +, FeO +, CoO +, NiO +, and CuO +," *Journal of the American Chemical Society*, vol. 122, pp. 12317–12326, Dec. 2000.

[36] K. Yoshizawa, Y. Shiota, and T. Yamabe, "Intrinsic reaction coordinate analysis of the conversion of methane to methanol by an iron–oxo species: A study of

crossing seams of potential energy surfaces," *The Journal of Chemical Physics*, vol. 111, no. 2, pp. 538–545, 1999.

[37] A. Fiedler, D. Schroeder, S. Shaik, and H. Schwarz, "Electronic Structures and Gas-Phase Reactivities of Cationic Late-Transition-Metal Oxides," *Journal of the American Chemical Society*, vol. 116, pp. 10734–10741, Nov. 1994.

[38] D. E. Clemmer, Y.-M. Chen, F. A. Khan, and P. B. Armentrout, "State-Specific Reactions of Fe+(a6D,a4F) with D2O and Reactions of FeO+ with D2," *The Journal of Physical Chemistry*, vol. 98, pp. 6522–6529, June 1994.

[39] D. Danovich and S. Shaik, "SpinOrbit Coupling in the Oxidative Activation of HH by FeO +. Selection Rules and Reactivity Effects," *Journal of the American Chemical Society*, vol. 119, pp. 1773–1786, Feb. 1997.

[40] J. N. Harvey and D. P. Tew, "Understanding the reactivity bottleneck in the spin-forbidden reaction FeO++H2Fe++H2O," *International Journal of Mass Spectrometry*, vol. 354-355, pp. 263–270, Nov. 2013.

[41] J. M. Matxain, J. M. Mercero, A. Irigoras, and J. M. Ugalde, "Discordant results on the FeO++ H2 reaction reconciled by quantum Monte Carlo theory," *Molecular Physics*, vol. 102, no. 23-24, pp. 2635–2637, 2004.

[42] M. J. Frisch, G. W. Trucks, H. B. Schlegel, G. E. Scuseria, M. A. Robb, J. R. Cheeseman, G. Scalmani, V. Barone, B. Mennucci, G. A. Petersson, H. Nakatsuji, M. Caricato, X. LI, H. P. Hratchian, A. F. Izmaylov, J. Bloino, G. Zheng, J. L. Sonnenberg, M. Hada, M. Ehara, K. Toyota, R. Fukuda, J. Hasegawa, M. Ishida, T. Nakajima, Y. Honda, O. Kitao, H. Nakai, T. Vreven, J. J. A. Montgomery, J. E. Peralta, F. Ogliaro, M. Bearpark, J. J. Heyd, E. Brothers, K. N. Kudin, V. N. Staroverov, R. Kobayashi, J. Normand, K. Raghavachari, A. Rendell, J. C. Burant, S. S. Iyengar, J. Tomasi, M. Cossi, N. Rega, J. M. Millam, M. Klene, J. E. Knox, J. B. Cross, V. Bakken, C. Adamo, J. Jaramillo, R. Gomperts, R. E. Stratmann, O. Yazyev, A. J. Austin, R. Cammi, C. Pomelli, J. W. Ochterski, R. L. Martin, K. Morokuma, V. G. Zakrzewski, G. A. Voth, P. Salvador, J. J. Dannenberg, S. Dapprich, A. D. Daniels, Ö. Farkas, J. B. Foresman, J. V. Ortiz, J. Cioslowski, and D. J. Fox, "Gaussian09 Revision C.01,"

[43] H. J. Werner and P. J. Knowles, "A Second Order MCSCF Method with Optimum Convergence," *J. Chem. Phys.*, vol. 82, p. 5053, 1985.

[44] P. J. Knowles and H. J. Werner, "An Efficient Second Order MCSCF Method for Long Configuration Expansions," *Chem. Phys. Letters*, vol. 115, pp. 259–267, 1985.

[45] J. A. Pople, M. Head-Gordon, and K. Raghavachari, "Quadratic configuration interaction. A general technique for determining electron correlation energies," *The Journal of Chemical Physics*, vol. 87, no. 10, p. 5968, 1987.

[46] G. Knizia, T. B. Adler, and H.-J. Werner, "Simplified CCSD(T)-F12 methods: Theory and benchmarks," *The Journal Of Chemical Physics*, vol. 130, p. 054104, Feb. 2009.

[47] P. Celani and H.-J. Werner, "Multireference perturbation theory for large restricted and selected active space reference wave functions," *The Journal of Chemical Physics*, vol. 112, no. 13, p. 5546, 2000.

[48] H.-J. Werner, "Third-order multireference perturbation theory The CASPT3 method," *Molecular Physics*, vol. 89, no. 2, pp. 645–661, 1996.

[49] H. J. Werner and P. J. Knowles, "An Efficient Internally Contracted Multiconfiguration Reference CI Method," *J. Chem. Phys.*, vol. 89, pp. 5803–5814, 1988.

[50] P. J. Knowles and H. J. Werner, "An Efficient Method for the Evaluation of Coupling Coefficients in Configuration Interaction Calculations," *Chem. Phys. Letters*, vol. 145, pp. 514–522, 1988.

[51] H. J. Werner, P. J. Knowles, G. Knizia, F. R. Manby, M. Schütz, *et al.*, "MOLPRO, a package of ab initio programs," tech. rep., Cardiff, UK, 2012.

[52] D. Schröder, H. Schwarz, D. E. Clemmer, Y. Chen, P. B. Armentrout, V. I. Baranov, and D. K. Böhme, "Activation of hydrogen and methane by thermalized FeO+ in the gas phase as studied by multiple mass spectrometric techniques," *International journal of mass spectrometry and ion processes*, vol. 161, no. 1, pp. 175–191, 1997.

[53] D. Schröder and H. Schwarz, "FeO Activates Methane," *Angewandte Chemie (International ed. in English)*, vol. 29, pp. 1433–1434, Dec. 1990.

[54] D. H. Bross, J. G. Hill, H. J. Werner, and K. A. Peterson, "Explicitly correlated composite thermochemistry of transition metal species," *The Journal of Chemical Physics*, vol. 139, p. 094302, Sept. 2013.

[55] R. B. Metz, C. Nicolas, M. Ahmed, and S. R. Leone, "Direct determination of the ionization energies of FeO and CuO with VUV radiation," *The Journal of Chemical Physics*, vol. 123, no. 11, p. 114313, 2005.

[56] A. Kramida, Y. Ralchenko, J. Reader, and NIST ASD Team, "NIST Atomic Spectra Database (version 5.1), [online].." http://physics.nist.gov/asd, 2014. Saturday, 24-May-2014 16:13:18 EDT.

[57] T. J. Lee and P. R. Taylor, "A diagnostic for determining the quality of single-reference electron correlation methods," *International Journal of Quantum Chemistry*, vol. 36, no. S23, pp. 199–207, 1989.

[58] C. N. Sakellaris, E. Miliordos, and A. Mavridis, "First principles study of the ground and excited states of FeO, FeO+, and FeO," *The Journal of Chemical Physics*, vol. 134, no. 23, pp. 234308–234308–16, 2011.

[59] A. Fiedler, J. Hrusak, W. Koch, and H. Schwarz, "The energetical and structural properties of FeO+. An application of multireference perturbation theory," *Chemical Physics Letters*, vol. 211, no. 2, pp. 242–248, 1993.

[60] M. Filatov and S. Shaik, "Theoretical Investigation of Two-State-Reactivity Pathways of HH Activation by FeO +: AdditionElimination, "Rebound", and Oxene-Insertion Mechanisms," *The Journal of Physical Chemistry A*, vol. 102, pp. 3835–3846, May 1998.

[61] M. Reiher, O. Salomon, and B. Artur Hess, "Reparameterization of hybrid functionals based on energy differences of states of different multiplicity," *Theoretical Chemistry Accounts*, vol. 107, pp. 48–55, Dec. 2001.

[62] S. Niu and M. B. Hall, "Theoretical studies on reactions of transition-metal complexes.," *Chemical Reviews*, vol. 100, pp. 353–406, Feb. 2000.